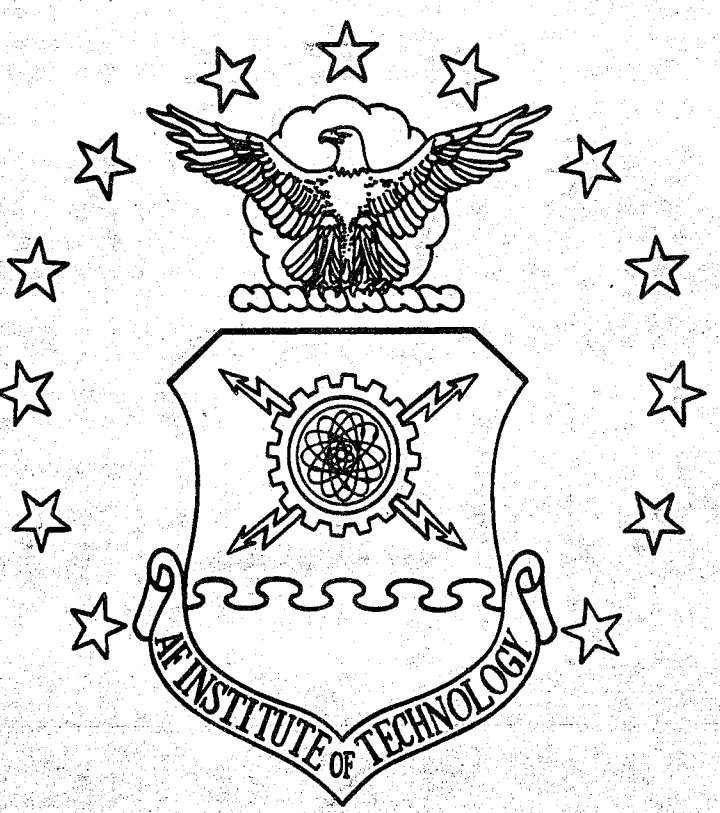

DEPARTMENT OF THE AIR FORCE

AIR UNIVERSITY

AIR FORCE INSTITUTE OF TECHNOLOGY

Wright-Patterson Air Force Base, Ohio

AFIT/GE/ENG/95D-25

Characterization of Atmospheric Turbulence Over Long Horizontal Paths Using Optical Slope Measurements

THESIS

Eric Eugene Silbaugh
Captain, USAF

AFIT/GE/ENG/95D-25

The views expressed in this thesis are those of the author and do not reflect the official policy or position of the Department of Defense or the U. S. Government.

AFIT/GE/ENG/95D-25

Characterization of Atmospheric Turbulence Over Long Horizontal Paths Using Optical Slope Measurements

THESIS

Presented to the Faculty of the School of Engineering

of the Air Force Institute of Technology

Air University

In Partial Fulfillment of the

Requirements for the Degree of

Master of Science in Electrical Engineering

Eric Eugene Silbaugh, BEE

Captain, USAF

December 1995

Acknowledgements

Many people besides the author have contributed to the success of this thesis. Special thanks are due to my advisor, Dr. Byron Welsh, for his guidance and encouragement throughout my time at AFIT. Dr. Welsh's copious knowledge of optical systems operating in turbulence was crucial to my success. It was a pleasure working with you. Maj Mike Roggemann freely shared his knowledge of the `otfsim3` code and kept me straight on the physics of atmospheric turbulence. Thanks to Maj Bob Mills for providing encouragement and many interesting discussions on new and bizarre communications methods. My classmates in the comm/radar program provided many enlightening discussions, much needed sanity checks, and the occasional comic relief. Last, but not least, thanks to my Creator for this opportunity to learn a little more about one small aspect of His universe.

Eric Eugene Silbaugh

Table of Contents

List of Figures

List of Tables

Abstract

Atmospheric turbulence has long been recognized as one of the fundamental factors affecting optical systems operating through the atmosphere. Turbulence over vertical paths has been well characterized, both theoretically and experimentally. Much less is known about turbulence over long, horizontal paths. Perturbations of the wave front phase can be measured using a Hartmann wave front sensor (H-WFS). Theoretical expressions for the tilt-removed structure function of the H-WFS slope measurements were derived and evaluated using quadrature. These slope structure functions are functions of the phase structure function. The Kolmogorov turbulence model was assumed. Simulated H-WFS slope measurements were generated using an adaptive optics simulation code. The effects of deterministic aberrations on the structure function estimator were illustrated using the simulated slope measurements. Average slope removal was shown to be effective in removing the effects of aberrations. Five H-WFS measurement data sets from the ABLE ACE database were analyzed for homogeneity, isotropy, and fit to theory. The ABLE ACE experiment recorded H-WFS measurements over horizontal paths 20-200 km in length. Results indicate that the turbulence encountered appears to be homogeneous and isotropic and seems to fit the Kolmogorov turbulence model.

Characterization of Atmospheric Turbulence Over Long Horizontal Paths Using Optical Slope Measurements

I. Introduction

Atmospheric turbulence has long been recognized as one of the most significant factors limiting the performance of optical systems. Even the best astronomical observatories, with telescopes meters in diameter, obtain resolutions equivalent to telescopes only ten to twenty centimeters in diameter because of atmospheric turbulence [17]. Thus, characterization of atmospheric turbulence is of paramount importance in understanding its effects on optical systems.

1.1 Background

Understanding atmospheric turbulence is critical for several technologies which support USAF missions. Ground-based telescopes are used to image satellites and orbital debris. The resolution of these telescopes can be improved using adaptive optics which compensate for the effects of turbulence. However, many adaptive techniques require stochastic models of turbulence. Using incorrect models can artificially degrade the performance of an adaptive optical system [21].

High energy airborne lasers involve laser beams propagated over long, horizontal paths in the troposphere and stratosphere. Scintillation of the optical beam causes the spot on the target to break up reducing the available power. Adaptive optics may help compensate for some of the scintillation. Understanding the statistics of atmospheric turbulence will help determine the feasibility and operational limits of this concept, and the role adaptive optics can play in overcoming some of these limits [25].

Finally, air-to-air optical communication has the potential benefits of long range, low probability of intercept (LPI), and high data rates. Predicting system performance, detector design, and estimating the benefits of forward error correction schemes are highly dependent on an accurate knowledge of turbulence statistics [4, 18, 1].

Vertical paths through the atmosphere have been studied intensively and sophisticated turbulence models have been developed because ground-based telescopes have been the primary interest [1, 10, 13, 17]. Balloon-born thermosondes, radar sounders, and sonar profilometers are all well established

methods for measuring atmospheric turbulence [13]. Unfortunately, these methods are most useful over vertical paths.

Long, horizontal paths are important for new applications such as airborne laser weapons and air-to-air optical communications [18, 25]. However, whether atmospheric turbulence over long, horizontal paths conforms to the same theoretical models as turbulence over vertical paths is not well understood. A few experiments have been conducted to measure atmospheric turbulence over horizontal paths.

1.2 Previous experiments

Wright Laboratory performed a series of experiments, called HAVE LACE, during 1985. The goal of these experiments was to determine the feasibility of air-to-air optical communications by measuring the scintillation statistics of a laser beam propagated between two aircraft [5]. Unfortunately, these scintillation statistics tell us little about the phase perturbations of the wave front. It is the phase perturbations which ultimately produce scintillations. Thus, the HAVE LACE measurements are not useful for directly characterizing the effects of atmospheric turbulence on the phase of an optical wave front.

Phillips Laboratory performed a series of experiments in 1993, called ABLEX, to characterize turbulence in the upper atmosphere. ABLEX used a temperature probe mounted on the nose of an aircraft to provide an indirect measurement of turbulence along the aircraft's path [3]. Calibration of this temperature sensor is difficult and the subject of ongoing research [19]. To characterize horizontal paths, these temperature measurements must be integrated along the aircraft's path while accounting for variations in the the aircraft's velocity.

1.3 The ABLE ACE experiment

ABLE ACE is a series of experiments performed by the Phillips Laboratory during January and March of 1995. The goal of ABLE ACE is to measure laser beam propagation characteristics over long, near-horizontal paths above and around the tropopause. The effects of atmospheric turbulence on the amplitude and phase characteristics of a laser beam are of primary interest. Predicting the performance of optical systems depends on knowledge of these characteristics [3, 25].

During the experiment, measurements were made on laser beams propagating between two aircraft flying in the stratosphere separated by up to hundreds of kilometers. The laser beam propagates over a long horizontal path from the transmitter aircraft to the receiver aircraft which carries a telescope that collects a portion of the laser beam. As the laser beam propagates between the two aircraft through the atmosphere the wave front is perturbed. These wave front perturbations are a direct effect of the turbulence encountered by the laser beam along the propagation path. Measuring and analyzing these perturbations should enable us to characterize upper atmosphere turbulence and validate theoretical models.

Measurements of wave front phase perturbations made using a Shack-Hartmann wave front sensor (H-WFS) are the focus of this thesis. Collecting H-WFS slope measurements aboard a moving aircraft requires a tracking system that keeps the receiving telescope pointed at the transmitting laser. This tracking system attempts to remove the overall tilt from the wave front as it tracks the transmitter. Tracking errors produce overall tilts not induced by atmospheric turbulence. Tracking errors can also be produced by random jolts and vibrations within the aircraft. Any observed overall tilt must be removed in the data analysis because of this removal and corruption of the overall tilt.

A H-WFS cannot sense the wave front phase directly. Instead, it produces a set of wave front slope measurements and the wave front phase must be inferred from the slope measurements. The standard approach is to use a phase reconstruction algorithm to recover the phase from the phase slope measurements. Phase reconstruction is widely used in adaptive optics systems and has been shown to work well in laboratory measurements of turbulence [12]. Unfortunately, phase reconstruction algorithms are sensitive to errors in the slope measurements. Any aberrations or tilt not due to turbulence will be reconstructed. Measurement noise will produce errors the reconstructed phase.

The primary statistical measure of atmospheric turbulence is the phase structure function, which can be calculated from the recovered phase. The phase structure function describes the perturbations induced on the wave front phase by atmospheric turbulence. A large body of theory using the phase structure function to describe turbulence is available.

Researchers at the USAF Phillips Laboratory have attempted to use phase reconstruction techniques to analyze atmospheric turbulence using the ABLE ACE H-WFS data [2]. The researchers used tilt-removed H-WFS slope measurements and a well-known least-squares phase reconstruction

algorithm [16] to recover a set of coefficients for the Zernike polynomials [14] which describe the wave front phase. These results did not fit any known model for atmospheric turbulence.

The researcher's next approach was to use a minimum-variance phase reconstruction algorithm [24] known to produce better results than the least-squares reconstructor under noisy conditions [16]. The minimum-variance reconstructor uses knowledge about the statistics of the measurement noise and atmospheric turbulence to improve its performance. The Zernike coefficients obtained using this method fit the Kolmogorov turbulence model. However, it was unclear if the fit to the Kolmogorov model was because the turbulence was indeed Kolmogorov or was an artifact of the assumptions used in the minimum-variance reconstructor.

Other problems encountered were with obscured and unreliable subapertures in the H-WFS. Special efforts had to be made in the phase reconstruction algorithms to account for these obscured and unreliable subapertures.

These difficulties provided the impetus to consider using the slope measurements themselves to characterize atmospheric turbulence. Using the slope measurements directly allows us to avoid phase reconstruction with its heavy computational load and sensitivity to measurement noise and aberrations.

1.4 Problem description and scope

Characterizing atmospheric turbulence over long horizontal paths using H-WFS slope measurements directly is the goal of this thesis. The ABEL ACE H-WFS measurements will be used. Since turbulence is random this characterization must be through the turbulence's statistical properties. Structure functions are one of the most powerful and widely used statistical quantities for characterizing atmospheric turbulence. In this thesis the structure function of the H-WFS slope measurements was used to avoid phase reconstruction. The analysis steps used in this thesis were:

- Derive and evaluate a theoretical expression for the structure function of the H-WFS slopes.
- Estimate slope structure functions from the H-WFS slope measurements.
- Analyze the slope structure functions to determine the homogeneity and isotropy of the measured turbulence.
- Compare the estimated and theoretical slope structure functions to see how well they fit.

1.5 Summary

Chapter II provides the derivation and evaluation of the theoretical slope structure function using widely accepted models of atmospheric turbulence. The H-WFS measurement processing and estimation of the slope structure function are described in Chapter III. Chapter IV identifies the ABLE ACE data sets analyzed and presents an analysis of the homogeneity and isotropy of upper atmosphere turbulence. The fit between estimated and theoretical slope structure functions is also detailed. Chapter V presents conclusions and provides suggestions for further research.

II. Theory

The difficulties experienced by researchers at the USAF Phillips Laboratory in using standard wave front reconstruction techniques motivates us to examine the slope measurements directly, bypassing the computationally intense phase reconstruction step. This chapter begins with a brief description of atmospheric turbulence and how a Hartmann wave front sensor (H-WFS) is modeled mathematically. The slope structure function is then defined and manipulated into a form which depends on the phase structure function. Last, the theoretical expressions obtained are evaluated using numerical quadrature.

2.1 Atmospheric Turbulence

Atmospheric turbulence is fundamentally generated by differential heating of the Earth's atmosphere. Large eddies of warm air mix with colder air, transferring energy from larger eddies to smaller eddies in the process. These smaller eddies transfer energy to still smaller eddies until viscous effects dominate. At this point, the flow becomes laminar and energy is dissipated as heat. Eddies with different temperatures have different densities and therefore different indices of refraction. It is these random index of refraction variations which corrupt an optical wave front as it propagates through the atmosphere.

Analyses by Kolmogorov [11] and Tatarski [22] are the seminal theoretical works on the statistics of atmospheric turbulence. Kolmogorov derived a three dimensional power spectral density (PSD) for the index of refraction variations in the atmosphere. Tatarski, in turn, derived the structure function for index of refraction variations. Key assumptions in Kolmogorov's and Tatarski's derivations are the homogeneity and isotropy of the atmospheric turbulence. Homogeneity means the turbulence's PSD does not depend upon location in the atmosphere; the turbulence is wide-sense stationary (WSS). Isotropy means the turbulence's PSD is independent of the direction of propagation through the atmosphere.

The Kolmogorov PSD is proportional to a simple 11/3 power law within a region called the inertial subrange defined by the inner scale and the outer scale. The inner scale is the smallest eddy size below which the turbulence becomes laminar and kinetic energy is dissipated as heat. The outer scale denotes the size of the largest eddies which form in the atmosphere. Clearly, eddy size is limited by the finite size of the atmosphere and the assumptions of homogeneity and isotropy will eventually be

violated. Fortunately, the range between the inner and outer scales covers several orders of magnitude in many situations. Also, many optical propagation calculations are insensitive to the exact nature of the PSD beyond the inner and outer scales.

Mathematically, Kolmogorov PSD implies infinite energy, which is not physically possible. While the Kolmogorov PSD may not be strictly physically valid it is the most widely used power spectrum. The Kolmogorov PSD is also known to accurately model the turbulence seen on vertical paths. Von Karman [23] proposed a PSD which has finite energy and falls off rapidly outside the inner and outer scales. Recently, Stribling [21] has investigated turbulence power spectrums based on general power laws with exponents between 3 and 4.

2.2 *Phase structure functions*

The wave front phase of an optical beam is perturbed by random refractive index variations as it travels through atmospheric turbulence. These perturbations are assumed to have zero mean. The effect of random refractive index variations on an optical beam are most commonly described using the phase structure function, defined as,

$$D_\phi(\vec{r}_1, \vec{r}_2) = \left\langle [\phi(\vec{r}_1) - \phi(\vec{r}_2)]^2 \right\rangle, \tag{2.1}$$

where $\phi(\vec{r})$ is a single realization of the wave front phase, $\vec{r}_1$ and $\vec{r}_2$ are two coordinate positions, and $\langle \cdot \rangle$ denotes the ensemble average. This is actually the general form for any structure function [8].

If the random refractive index variations are homogeneous the phase structure function will be a function only of the difference between the two coordinates, $\vec{r}_1 - \vec{r}_2$. If the the refractive index variations are also isotropic the phase structure function will depend only on the magnitude of the separation, $r = |\vec{r}_1 - \vec{r}_2|$.

Fried [7] was able to derive a functional form for the phase structure function by applying the index of refraction structure function, derived from Kolmogorov turbulence theory, to an optical wave propagating through the atmosphere. His expression for plane wave propagation,

$$D_\phi(r) = 6.88 \left(\frac{r}{r_o} \right)^{5/3}, \tag{2.2}$$

accounts for variations of the turbulence strength along the propagation path length since r_o, the 'coherence diameter' or 'seeing parameter', is defined as

$$r_o = \left[\frac{6.88\lambda^2}{2.91 \int_0^L \mathrm{d}z \, C_n^2(z)} \right]^{3/5}, \tag{2.3}$$

where $C_n^2(z)$ is the Kolmogorov structure constant along the path of propagation, L is the path length, and λ is the wavelength.

2.3 Hartmann wavefront sensor

One method of measuring the wave front phase is to use a Hartmann wave front sensor (H-WFS). An H-WFS cannot sense the phase directly; it produces slope measurements which are the average wave front phase gradient over the subapertures of the sensor [16, 24],

$$\begin{aligned} s_n^i &= \int \mathrm{d}\vec{r} \, W_n(\vec{r}) \left(\nabla \phi(\vec{r}) \cdot \hat{d}_i \right) \\ &= -\int \mathrm{d}\vec{r} \left(\nabla W_n(\vec{r}) \cdot \hat{d}_i \right) \phi(\vec{r}), \end{aligned} \tag{2.4}$$

where s_n^i is the slope in the ith direction at the nth subaperture, $\phi(\vec{r})$ is the wave front phase, $W_n(\vec{r})$ is the subaperture weighting function, $\vec{r}$ is a two-dimensional vector in the plane transverse to the wave front propagation, $\hat{d}_i$ is the unit vector in the ith direction, ∇ is the gradient operator, and $\cdot$ represents the vector dot product. The indices i and j can take on the values x or y since the H-WFS produces slope measurements in both the x and x directions.

The H-WFS used in the ABEL ACE experiments had square subapertures so we can write the subaperture weighting function as,

$$W_n(\vec{r}) = W_n(x,y) = \frac{1}{d^2} \mathrm{rect}\left(\frac{x - x_n}{d} \right) \mathrm{rect}\left(\frac{y - y_n}{d} \right), \tag{2.5}$$

where d is the distance across the subaperture edge and the point (x_n, y_n) is the center of the nth subaperture, and

$$\mathrm{rect}\left(\frac{x - x_n}{d} \right) = \begin{cases} 1 & , |x - x_n| \leq \frac{d}{2} \\ 0 & , \text{else} \end{cases}. \tag{2.6}$$

Note that $W_n(\vec{r})$ is normalized to have unit volume. The gradient of the subaperture weighting function then becomes,

$$\begin{aligned}\nabla W_n(\vec{r}) = \nabla W_n(x,y) &= \hat{d}_x \frac{\partial}{\partial x} W_n(x,y) + \hat{d}_y \frac{\partial}{\partial y} W_n(x,y) \\ &= \frac{\hat{d}_x}{d^2}\left[\delta\left(x - x_n + \frac{d}{2}\right) - \delta\left(x - x_n - \frac{d}{2}\right)\right] \text{rect}\left(\frac{y - y_n}{d}\right) \\ &\quad + \frac{\hat{d}_y}{d^2}\left[\delta\left(y - y_n + \frac{d}{2}\right) - \delta\left(y - y_n - \frac{d}{2}\right)\right] \text{rect}\left(\frac{x - x_n}{d}\right),\end{aligned} \tag{2.7}$$

where $\delta(\cdot)$ is the unit impulse function.

2.4 Slope structure functions

The phase structure function statistically describes the random perturbations of the wave front perturbations. Since the H-WFS slope measurements are a linear operation on the phase we expect the slope structure function to be a function of the phase structure function. Combining the definition of a structure function and the wave front sensor slopes produces a slope structure function,

$$\begin{aligned}D_s^{ij}(n,k) &= \left\langle \left[s_n^i - s_k^j\right]^2 \right\rangle \\ &= \left\langle \left[\int \mathrm{d}\vec{r}_1 \left(\nabla W_n(\vec{r}_1)\cdot \hat{d}_i\right)\phi(\vec{r}_1) - \int \mathrm{d}\vec{r}_2 \left(\nabla W_k(\vec{r}_2)\cdot \hat{d}_j\right)\phi(\vec{r}_2)\right]^2 \right\rangle.\end{aligned} \tag{2.8}$$

Here the notation $D_s^{ij}(n,k)$ represents the slope structure function in the ith and jth directions for the nth and kth subapertures at the points $\vec{r}_1$ and $\vec{r}_2$. The H-WFS produces slope measurements in the x and y directions; these directions are the values i and j may take.

Collecting WFS slope measurements aboard a moving aircraft requires a tracking system that keeps the receiving telescope pointed at the transmitting laser. This tracking system attempts to remove the overall tilt from the wave front as it tracks the transmitter. The tracking system is also noisy. Tracking errors, and random jolts and vibrations within the aircraft, produce overall tilts not induced by atmospheric turbulence. Because of this removal and corruption of the overall tilt, any observed overall tilt will be removed in the data analysis. Thus, we must determine the effect of removing the overall tilt from the slope structure function.

The tilt removed phase can be represented as, $\phi(\vec{r}) - \vec{a} \cdot \vec{r}$, where $\vec{a}$ is a vector representing the overall wavefront tilt. Substituting the tilt removed phase into Eq. (2.8) produces,

$$D_s^{ij}(n,k) = \left\langle \left[\int \mathrm{d}\vec{r}_1 \left(\nabla W_n(\vec{r}_1) \cdot \hat{d}_i \right) \phi(\vec{r}_1) - \int \mathrm{d}\vec{r}_2 \left(\nabla W_k(\vec{r}_2) \cdot \hat{d}_j \right) \phi(\vec{r}_2) - \left(\vec{a} \cdot \hat{d}_i - \vec{a} \cdot \hat{d}_j \right) \right]^2 \right\rangle . \tag{2.9}$$

The first two terms are the wave front sensor slopes and the last term is the difference of the overall tilts in the ith and jth directions. When the direction vectors are identical the overall tilts exactly cancel, and the slope structure function is insensitive to overall tilt. This insensitivity to overall tilt is analogous to the insensitivity of the phase structure function to overall piston.

However, when the direction vectors are different the overall tilts will not, in general, cancel and the slope structure function will be sensitive to tilt removal. Thus, we must consider two cases in this derivation. The case where the direction vectors are identical (D_s^{xx} and D_s^{yy}) is referred to as the self slope structure function; the case where the direction vectors differ (D_s^{xy} and D_s^{yx}) is referred to as the cross slope structure function.

2.4.1 Self slope structure function. Consider the self slope structure function for the x-slopes first. Expanding Eq. (2.9), canceling the tilt, and moving the expectation operator inside the integrations produces:

$$\begin{aligned} D_s^{xx}(n,k) = & \iint \mathrm{d}\vec{r}_1 \mathrm{d}\vec{r}_1' \left(\nabla W_n(\vec{r}_1) \cdot \hat{d}_x \right) \left(\nabla W_n(\vec{r}_1') \cdot \hat{d}_x \right) \langle \phi(\vec{r}_1) \phi(\vec{r}_1') \rangle \\ & + \iint \mathrm{d}\vec{r}_2 \mathrm{d}\vec{r}_2' \left(\nabla W_n(\vec{r}_2) \cdot \hat{d}_x \right) \left(\nabla W_n(\vec{r}_2') \cdot \hat{d}_x \right) \langle \phi(\vec{r}_2) \phi(\vec{r}_2') \rangle \\ & - 2 \iint \mathrm{d}\vec{r}_1 \mathrm{d}\vec{r}_2 \left(\nabla W_n(\vec{r}_1) \cdot \hat{d}_x \right) \left(\nabla W_n(\vec{r}_2) \cdot \hat{d}_x \right) \langle \phi(\vec{r}_1) \phi(\vec{r}_2) \rangle . \end{aligned} \tag{2.10}$$

Expanding the phase correlations using the identity

$$\langle \phi(\vec{r}_1) \phi(\vec{r}_2) \rangle = \frac{1}{2} \langle \phi^2(\vec{r}_1)) \rangle + \frac{1}{2} \langle \phi^2(\vec{r}_2)) \rangle - \frac{1}{2} D_\phi(\vec{r}_1, \vec{r}_2),$$

where $D_\phi(\vec{r}_1, \vec{r}_2)$ is the phase structure function defined in Eq. (2.1), allows us to write the slope structure function in terms of the phase structure function. The correlations $\langle \phi^2(\vec{r}_1) \rangle$ and $\langle \phi^2(\vec{r}_2) \rangle$ are constants because the phase, $\phi(\vec{r})$, is assumed to be homogeneous (WSS). Since $\nabla W_n(\vec{r})$ is an

odd function and the integrals have symmetric limits these terms will vanish. Thus, the slope structure function becomes,

$$\begin{aligned} D_s^{xx}(n,k) &= -\frac{1}{2}\iint \mathrm{d}\vec{r}_1 \mathrm{d}\vec{r}_1' \left(\nabla W_n(\vec{r}_1)\cdot\hat{d}_x\right)\left(\nabla W_n(\vec{r}_1')\cdot\hat{d}_x\right) D_\phi(\vec{r}_1,\vec{r}_1') \\ &\quad -\frac{1}{2}\iint \mathrm{d}\vec{r}_2 \mathrm{d}\vec{r}_2' \left(\nabla W_k(\vec{r}_2)\cdot\hat{d}_x\right)\left(\nabla W_k(\vec{r}_2')\cdot\hat{d}_x\right) D_\phi(\vec{r}_2,\vec{r}_2') \\ &\quad +\iint \mathrm{d}\vec{r}_1 \mathrm{d}\vec{r}_2 \left(\nabla W_n(\vec{r}_1)\cdot\hat{d}_x\right)\left(\nabla W_k(\vec{r}_2)\cdot\hat{d}_x\right) D_\phi(\vec{r}_1,\vec{r}_2). \end{aligned}$$

Using Eq. (2.8), the sifting property of the impulse function, and the homogeneity and isotropy of the phase structure function we can write,

$$\begin{aligned} D_s^{xx}(n,k) &= -\frac{1}{2d^4}\iint \mathrm{d}y_1 \mathrm{d}y_1' \left[2D_\phi(|y_1-y_1'|) - D_\phi(|-d, y_1-y_1'|) - D_\phi(|d, y_1-y_1'|)\right] \\ &\qquad \times \mathrm{rect}\left(\frac{y_1-y_n}{d}\right)\mathrm{rect}\left(\frac{y_1'-y_n}{d}\right) \\ &\quad -\frac{1}{2d^4}\iint \mathrm{d}y_2 \mathrm{d}y_2' \left[2D_\phi(|y_2-y_2'|) - D_\phi(|-d, y_2-y_2'|) - D_\phi(|d, y_1-y_1'|)\right] \\ &\qquad \times \mathrm{rect}\left(\frac{y_2-y_k}{d}\right)\mathrm{rect}\left(\frac{y_2'-y_k}{d}\right) \\ &\quad +\frac{1}{d^4}\iint \mathrm{d}y_1 \mathrm{d}y_2 \left[2D_\phi(|x_n-xk, y_1-y_2|) - D_\phi(|x_n-xk-d, y_1-y_2|)\right. \\ &\qquad \left. -D_\phi(|x_n-xkd, y_1-y_2|)\right]\mathrm{rect}\left(\frac{y_1-y_n}{d}\right)\mathrm{rect}\left(\frac{y_2'-y_k}{d}\right). \end{aligned}$$

Here the shorthand notation $|x,y| = \sqrt{x^2+y^2}$ is used to simplify the arguments of the phase structure functions. Using the variable substitutions

$$\begin{aligned} u &= y_1 - y_1' \quad u' = \tfrac{1}{2}(y_1+y_1') \\ u &= y_2 - y_2' \quad u' = \tfrac{1}{2}(y_2+y_2') \\ u &= y_1 - y_2 \quad u' = \tfrac{1}{2}(y_1+y_2) \end{aligned}$$

in these three integrals, respectively, produces

$$
\begin{aligned}
D_s^{xx}(n,k) \;=\; & -\frac{1}{2d^4}\int \mathrm{d}u\,\left[2D_\phi(|u|) - D_\phi(|-d,u|) - D_\phi(|d,u|)\right] \\
& \qquad \times \int \mathrm{d}u'\,\mathrm{rect}\left(\frac{u'+u/2-y_n}{d}\right)\mathrm{rect}\left(\frac{u'-u/2-y_n}{d}\right) \\
& -\frac{1}{2d^4}\int \mathrm{d}u\,\left[2D_\phi(|u|) - D_\phi(|-d,u|) - D_\phi(|d,u|)\right] \\
& \qquad \times \int \mathrm{d}u'\,\mathrm{rect}\left(\frac{u'+u/2-y_k}{d}\right)\mathrm{rect}\left(\frac{u'-u/2-y_k}{d}\right) \\
& +\frac{1}{d^4}\int \mathrm{d}u\,\left[2D_\phi(|x_n-x_k,u|) - D_\phi(|x_n-x_k-d,u|) - D_\phi(|x_n-x_k+d,u|)\right] \\
& \qquad \times \int \mathrm{d}u'\,\mathrm{rect}\left(\frac{u'+u/2-y_n}{d}\right)\mathrm{rect}\left(\frac{u'-u/2-y_k}{d}\right).
\end{aligned}
$$

Recognizing the $\int \mathrm{d}u'$ terms as a correlation, which can be written as

$$
\begin{aligned}
\int \mathrm{d}u'\,\mathrm{rect}\left(\frac{u'+u/2-y_n}{d}\right)\mathrm{rect}\left(\frac{u'-u/2-y_k}{d}\right) &= \begin{cases} d-|u-y_n+y_k| & ,|u-y_n+y_k|\le d \\ 0 & ,\text{else} \end{cases} \\
&= \mathrm{tri}\left[\frac{u-(y_n-y_k)}{d}\right],
\end{aligned}
$$

the self slope structure function reduces to:

$$
\begin{aligned}
D_s^{xx}(n,k) \;=\; & -\frac{1}{d^4}\int \mathrm{d}u\,\left[2D_\phi(|u|) - D_\phi(|-d,u|) - D_\phi(|d,u|)\right]\mathrm{tri}\left[\frac{u}{d}\right] \\
& +\frac{1}{d^4}\int \mathrm{d}u\,\left[2D_\phi(|x_n-x_k,u|) - D_\phi(|x_n-x_k-d,u|)\right. \\
& \qquad \left. -D_\phi(|x_n-x_k+d,u|)\right]\mathrm{tri}\left[\frac{u-(y_n-y_k)}{d}\right]. \qquad (2.11)
\end{aligned}
$$

Using this same procedure on the y-slope self structure function produces:

$$
\begin{aligned}
D_s^{yy}(n,k) \;=\; & -\frac{1}{d^4}\int \mathrm{d}u\,\left[2D_\phi(|u|) - D_\phi(|u,-d|) - D_\phi(|u,d|)\right]\mathrm{tri}\left[\frac{u}{d}\right] \\
& +\frac{1}{d^4}\int \mathrm{d}u\,\left[2D_\phi(|u,y_n-y_k|) - D_\phi(|u,y_n-y_k-d|)\right. \\
& \qquad \left. -D_\phi(|u,y_n-y_k+d|)\right]\mathrm{tri}\left[\frac{u-(x_n-x_k)}{d}\right]. \qquad (2.12)
\end{aligned}
$$

Up to this point in the derivation the only assumptions made were the homogeneity and isotropy of the phase structure function, and the zero mean characteristics of the wave front phase. In particular, nothing has been assumed about the form of the phase structure function. Any appropriate phase structure function (Kolmogorov, Von Karman, general power law) may be used. The simplest and most widely used form is the Kolmogorov structure function which Fried writes as [7],

$$D_\phi(r) = 6.88\left(\frac{r}{r_o}\right)^{5/3}.$$

Substituting this phase structure function into the x-slope self structure function produces,

$$\begin{aligned} D_s^{xx}(n,k) &= -\frac{6.88}{d^4} r_o^{-5/3} \int \mathrm{d}u \left[2|u|^{5/3} - |-d,u|^{5/3} - |d,u|^{5/3}\right] \mathrm{tri}\left[\frac{u}{d}\right] \\ &\quad + \frac{6.88}{d^4} r_o^{-5/3} \int \mathrm{d}u \left[2|x_n - x_k, u|^{5/3} - |x_n - x_k - d, u|^{5/3}\right. \\ &\quad \left. -|x_n - x_k + d, u|^{5/3}\right] \mathrm{tri}\left[\frac{u - (y_n - y_k)}{d}\right]. \end{aligned} \tag{2.13}$$

Normalizing the integrals by using $\mathrm{d}u = d\,\mathrm{d}\xi$ produces the x-slope self structure function

$$\begin{aligned} D_s^{xx}(n,k) &= -6.88 d^{-1/3} r_o^{-5/3} \left\{2\int \mathrm{d}\xi \left[|1,\xi|^{5/3} - |\xi|^{5/3}\right] \mathrm{tri}\left[\xi\right]\right. \\ &\quad - \int \mathrm{d}\xi \left[\left|\frac{x_n - x_k}{d} - 1, \xi\right|^{5/3} + \left|\frac{x_n - x_k}{d} + 1, \xi\right|^{5/3} - 2\left|\frac{x_n - x_k}{d}, \xi\right|^{5/3}\right] \\ &\quad \left. \times \mathrm{tri}\left[\xi - \frac{(y_n - y_k)}{d}\right]\right\}. \end{aligned} \tag{2.14}$$

where the explicit dependence on the turbulence parameter, r_o, and the WFS subaperture dimension. d, have been moved outside the integrals. The same procedure produces the y-slope self structure function

$$\begin{aligned} D_s^{yy}(n,k) &= -6.88 r_o^{-5/3} d^{-1/3} \left\{2\int \mathrm{d}\xi \left[|1,\xi|^{5/3} - |\xi|^{5/3}\right] \mathrm{tri}\left(\xi\right)\right. \\ &\quad - \int \mathrm{d}\xi \left[\left|\frac{y_n - y_k}{d} - 1, \xi\right|^{5/3} + \left|\frac{y_n - y_k}{d} + 1, \xi\right|^{5/3} - 2\left|\frac{y_n - y_k}{d}, \xi\right|^{5/3}\right] \\ &\quad \left. \times \mathrm{tri}\left[\xi - \frac{(x_n - x_k)}{d}\right]\right\}. \end{aligned} \tag{2.15}$$

Notice that $D_s^{xx}(n,k)$ and $D_s^{yy}(n,k)$ have exactly the same functional forms except for the shift direction dependence in the tri$(\cdot)$ function. This result is not surprising and is a direct result of the isotropy of the phase structure function and the symmetry of the subaperture weighting function. The self slope structure functions, $D_s^{xx}(n,k)$ and $D_s^{yy}(n,k)$, will be evaluated numerically in Section 2.5 to determine their behavior. The next challenge is to determine the cross slope structure function.

2.4.2 Cross slope structure function. Recall that the cross slope structure function is sensitive to tilt removal. Expanding Eq. (2.9) for the xy slopes and moving the expectation operator inside the integrations produces,

$$\begin{aligned} D_s^{xy}(n,k) \;=\; & \iint \mathrm{d}\vec{r}_1 \mathrm{d}\vec{r}_1' \left(\nabla W_n(\vec{r}_1)\cdot\hat{d}_x\right)\left(\nabla W_n(\vec{r}_1')\cdot\hat{d}_x\right)\langle\phi(\vec{r}_1)\phi(\vec{r}_1')\rangle \\ & + \iint \mathrm{d}\vec{r}_2 \mathrm{d}\vec{r}_2' \left(\nabla W_k(\vec{r}_2)\cdot\hat{d}_y\right)\left(\nabla W_k(\vec{r}_2')\cdot\hat{d}_y\right)\langle\phi(\vec{r}_2)\phi(\vec{r}_2')\rangle \\ & - 2\iint \mathrm{d}\vec{r}_1 \mathrm{d}\vec{r}_2 \left(\nabla W_n(\vec{r}_1)\cdot\hat{d}_x\right)\left(\nabla W_k(\vec{r}_2)\cdot\hat{d}_y\right)\langle\phi(\vec{r}_1)\phi(\vec{r}_2)\rangle \\ & + 2\int \mathrm{d}\vec{r}_1 \left(\nabla W_n(\vec{r}_1)\cdot\hat{d}_x\right)\left\langle\left(\vec{a}\cdot\hat{d}_y - \vec{a}\cdot\hat{d}_x\right)\phi(\vec{r}_1)\right\rangle \\ & - 2\int \mathrm{d}\vec{r}_1 \left(\nabla W_k(\vec{r}_2)\cdot\hat{d}_y\right)\left\langle\left(\vec{a}\cdot\hat{d}_y - \vec{a}\cdot\hat{d}_x\right)\phi(\vec{r}_2)\right\rangle \\ & + \left\langle\left[\vec{a}\cdot\hat{d}_y - \vec{a}\cdot\hat{d}_x\right]^2\right\rangle. \end{aligned} \tag{2.16}$$

The first three terms are due only to the wavefront phase and thus compose the non-tilt-removed cross slope structure function. The last three terms arise from the tilt removal. With the procedure used for the self slope structure functions the first three terms can be immediately written in terms of the phase

structure function. The cross slope structure function becomes,

$$
\begin{aligned}
&D_s^{xy}(n,k) \\
&= -\frac{1}{2d^4}\int \mathrm{d}u\ [2D_\phi(|u|) - D_\phi(|-d,u|) - D_\phi(|d,u|)]\ \mathrm{tri}\left(\frac{u}{d}\right) \\
&\quad -\frac{1}{2d^4}\int \mathrm{d}u\ [2D_\phi(|u|) - D_\phi(|-d,u|) - D_\phi(|d,u|)]\ \mathrm{tri}\left(\frac{u}{d}\right) \\
&\quad -\frac{1}{d^4}\iint \mathrm{d}u\mathrm{d}v\ [D_\phi(|u-x_n+d/2, v-y_k+d/2|) + D_\phi(|u-x_n-d/2, v-y_k-d/2|) \\
&\qquad\qquad - D_\phi(|u-x_n+d/2, v-y_k-d/2|) - D_\phi(|u-x_n-d/2, v-y_k+d/2|)] \\
&\qquad\qquad \times \mathrm{rect}\left(\frac{u-x_k}{d}\right)\mathrm{rect}\left(\frac{v-y_n}{d}\right) \\
&\quad + 2\int \mathrm{d}\vec{r}_1\ \left(\nabla W_n(\vec{r}_1)\cdot\hat{d}_x\right)\left\langle\left(\vec{a}\cdot\hat{d}_y - \vec{a}\cdot\hat{d}_x\right)\phi(\vec{r}_1)\right\rangle \\
&\quad - 2\int \mathrm{d}\vec{r}_1\ \left(\nabla W_k(\vec{r}_2)\cdot\hat{d}_y\right)\left\langle\left(\vec{a}\cdot\hat{d}_y - \vec{a}\cdot\hat{d}_x\right)\phi(\vec{r}_2)\right\rangle \\
&\quad + \left\langle\left[\vec{a}\cdot\hat{d}_y - \vec{a}\cdot\hat{d}_x\right]^2\right\rangle .
\end{aligned}
\tag{2.17}
$$

The fourth and fifth terms of the cross slope structure function require calculation of the correlation between the wavefront's tilt and phase. Heidbreder [9] shows that these correlations can be written as,

$$
\left\langle\left(\vec{a}\cdot\hat{d}_x\right)\phi(x,y)\right\rangle = \frac{-\iint u\mathrm{d}u\mathrm{d}v\ P(u,v)D_\phi(|u-x,v-y|)}{2\iint u^2\mathrm{d}u\mathrm{d}v\ P(u,v)} \tag{2.18}
$$

$$
\left\langle\left(\vec{a}\cdot\hat{d}_y\right)\phi(x,y)\right\rangle = \frac{-\iint v\mathrm{d}u\mathrm{d}v\ P(u,v)D_\phi(|u-x,v-y|)}{2\iint v^2\mathrm{d}u\mathrm{d}v\ P(u,v)}, \tag{2.19}
$$

where $P(x,y)$ is the pupil function. Restricting $P(x,y)$ to be symmetric, inserting Eqs. (2.18) and (2.19) into the fourth and fifth terms of Eq. (2.17), expanding, grouping terms, and recognizing a common denominator produces,

$$
\begin{aligned}
&2\int \mathrm{d}\vec{r}_1\ \left(\nabla W_n(\vec{r}_1)\cdot\hat{d}_x\right)\left\langle\left(\vec{a}\cdot\hat{d}_y - \vec{a}\cdot\hat{d}_x\right)\phi(\vec{r}_1)\right\rangle \\
&= \frac{\iint (u-v)\mathrm{d}u\mathrm{d}v\ P(u,v)\int \mathrm{d}y_1\{D_\phi(|u-x_n+d/2, v-y_1|) - D_\phi(|u-x_n-d/2, v-y_1|)\}\mathrm{rect}\left(\frac{y_1-y_n}{d}\right)}{d^2\iint u^2\mathrm{d}u\mathrm{d}v\ P(u,v)}
\end{aligned}
\tag{2.20}
$$

and

$$2\int d\vec{r}_1 \left(\nabla W_k(\vec{r}_2)\cdot\hat{d}_y\right)\left\langle\left(\vec{a}\cdot\hat{d}_y-\vec{a}\cdot\hat{d}_x\right)\phi(\vec{r}_2)\right\rangle$$
$$=\frac{\iint(u-v)\,du\,dv\,P(u,v)\int dx_2\left\{D_\phi(|u-x_2,v-y_k+d/2|)-D_\phi(|u-x_2,v-y_k-d/2|)\right\}\mathrm{rect}\left(\frac{x_2-x_k}{d}\right)}{d^2\iint u^2\,du\,dv\,P(u,v)} \tag{2.21}$$

which depend only on the pupil function, $P(x,y)$, and the phase structure function, $D_\phi(r)$.

Assuming the tilts in the x and y directions are independent and zero mean, the last term of Eq. 2.17 can be expanded as,

$$\begin{aligned}\left\langle\left[\left(\vec{a}\cdot\hat{d}_y\right)-\left(\vec{a}\cdot\hat{d}_x\right)\right]^2\right\rangle &= \left\langle\left(\vec{a}\cdot\hat{d}_x\right)^2\right\rangle-2\left\langle\left(\vec{a}\cdot\hat{d}_x\right)\right\rangle\left\langle\left(\vec{a}\cdot\hat{d}_y\right)\right\rangle+\left\langle\left(\vec{a}\cdot\hat{d}_y\right)^2\right\rangle \\ &= \left\langle\left(\vec{a}\cdot\hat{d}_x\right)^2\right\rangle+\left\langle\left(\vec{a}\cdot\hat{d}_y\right)^2\right\rangle,\end{aligned}$$

which is the sum of the mean-square tilts in the x and y directions. Heidbreder shows that the mean-square tilt can be written as

$$\left\langle\left(\vec{a}\cdot\hat{d}_x\right)^2\right\rangle=\left\langle\left(\vec{a}\cdot\hat{d}_y\right)^2\right\rangle=\frac{-\iint uv\,du\,dv\,P(u)P(v)D_\phi(u-v)}{2\iint uv\,du\,dv P(u)P(v)}. \tag{2.22}$$

Because the pupil function is restricted to be symmetric, and the phase structure function is assumed to be homogeneous and isotropic, the mean-square tilt in the x and y directions are identical.

Pupil	Mean-square tilt
Square	$6.88(0.8598)D^{-1/3}r_o^{-5/3}$
Circular	$6.88(0.8281)D^{-1/3}r_o^{-5/3}$

Table 2.1 Mean-square tilt for square and circular pupils using Kolmogorov structure function. D is the side length or diameter of the pupil, respectively, and r_o is Fried's strength parameter.

Combining Eqs. (2.17), (2.20), (2.21), and (2.22) produces

$$
\begin{aligned}
&D_s^{xy}(n,k) \\
&= -\frac{1}{2d^4}\int \mathrm{d}u\,[2D_\phi(|u|) - D_\phi(|-d,u|) - D_\phi(|d,u|)]\,\mathrm{tri}\left(\frac{u}{d}\right) \\
&\quad -\frac{1}{2d^4}\int \mathrm{d}u\,[2D_\phi(|u|) - D_\phi(|-d,u|) - D_\phi(|d,u|)]\,\mathrm{tri}\left(\frac{u}{d}\right) \\
&\quad -\frac{1}{d^4}\iint \mathrm{d}u\mathrm{d}v\,[D_\phi(|u-x_n+d/2, v-y_k+d/2|) + D_\phi(|u-x_n-d/2, v-y_k-d/2|) \\
&\qquad\qquad - D_\phi(|u-x_n+d/2, v-y_k-d/2|) - D_\phi(|u-x_n-d/2, v-y_k+d/2|)] \\
&\qquad\qquad \times \mathrm{rect}\left(\frac{u-x_k}{d}\right)\mathrm{rect}\left(\frac{v-y_n}{d}\right) \\
&\quad + \frac{\iint (u-v)\mathrm{d}u\mathrm{d}v P(u,v)\int \mathrm{d}y_1\{D_\phi(|u-x_n+d/2, v-y_1|) - D_\phi(|u-x_n-d/2, v-y_1|)\}\mathrm{rect}\left(\frac{y_1-y_n}{d}\right)}{d^2\iint u^2\mathrm{d}u\mathrm{d}v\,P(u,v)} \\
&\quad - \frac{\iint (u-v)\mathrm{d}u\mathrm{d}v P(u,v)\int \mathrm{d}x_2\{D_\phi(|u-x_2, v-y_k+d/2|) - D_\phi(|u-x_2, v-y_k-d/2|)\}\mathrm{rect}\left(\frac{x_2-x_k}{d}\right)}{d^2\iint u^2\mathrm{d}u\mathrm{d}v\,P(u,v)} \\
&\quad - \frac{\iint uv\,\mathrm{d}u\mathrm{d}v\,P(u)P(v)D_\phi(u-v)}{\iint uv\,\mathrm{d}u\mathrm{d}v P(u)P(v)}.
\end{aligned}
\tag{2.23}
$$

Note that an explicit functional form of the phase structure function has not been assumed; only homogeneity and isotropy. Any appropriate structure function may be used at this point.

Heidbreder has computed the mean-square tilt (Eq. 2.22) for both square and circular pupils assuming the Kolmogorov phase structure function. Heidbreder's results are summarized in Table 2.1.

2.5 *Slope structure function properties*

Now that we have the self slope structure function we can examine its properties. The self slope structure function is only a function of the subaperture separation. However, there are an enormous number of possible separations in many directions. Concentrating on shifts in the x, y, and $\pm 45°$ directions will provide a representative sample of all possible shifts.

The self slope structure function consists of two scaling parameters which depend on the subaperture dimensions and the turbulence strength and a dimensionless integral which depends on differences

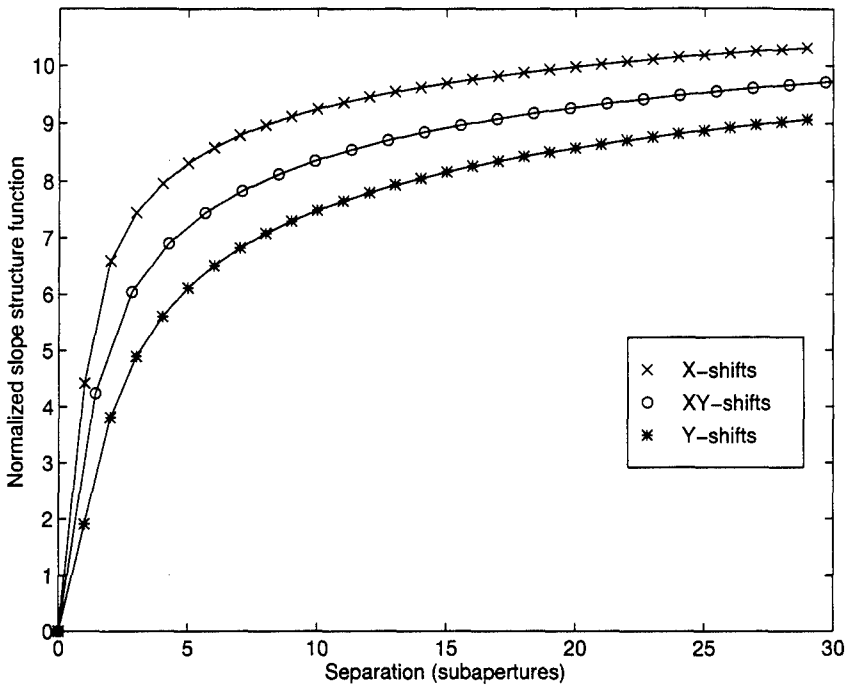

Figure 2.1 Normalized x-slope structure function for x, y, and xy shifts as a function of subaperture separation

of phase structure functions for various subaperture separations. Because the integral is dimensionless we need only evaluate it once for the separations of interest.

The dimensionless integral portion of Eq. (2.14) was evaluated using numerical quadrature for shifts in the x, y, and $\pm 45°$ shifts. The results are shown in Fig. 2.1 (the xy shifts correspond to the $\pm 45°$ directions. We can see that the slope structure function vanishes for zero shifts, as it should, and that all shift directions asymptotically tend toward the the same slope. The actual value of the slope structure function depends on the shift direction. These curves are also valid for the y-slope self structure function, D_s^{yy}, except the curve for the x and y shifts must be interchanged.

III. Statistical methods and simulation results

As we have seen in Chapter II, the WFS slope structure function is a function of the phase structure function, for which there exists a highly developed theory. Our goal is to use H-WFS slope measurements to estimate the slope structure functions and test for homogeneity, isotropy, and fit to the theory developed in Chapter II. In this chapter, the statistical methods used to analyze the H-WFS slope measurements are presented. The performance of these methods using simulated WFS slope measurements is also presented.

The steps used in analyzing the ABLE ACE WFS measurements were:

- choose a data set and segment the WFS images into contiguous sets of frames,
- process the WFS images to extract the slope measurements,
- estimate the slope structure functions,
- examine the slope structure functions for homogeneity and isotropy,
- and compare the estimated and theoretical slope structure functions.

In the next two sections we will briefly describe how a Hartmann WFS operates and define the slope structure function estimator. The following sections will examine each of the above steps in detail and the chapter will close with some comments on tradeoffs and limitations.

3.1 Hartmann WFS slope measurements

A Hartmann WFS consists of an array of lenslets and a detector array in the focal plane of the lenslet array. The incoming wave front is spatially segmented by the lenslet array; each segment is called a subaperture. A slice through this configuration is depicted in Fig. 3.1(a). The lenslet array in the H-WFS used in the ABEL ACE experiment was a square 21×21 subaperture grid and the detector was a CCD camera having a 512×512 pixel array.

Figure 3.1(b) depicts a single subaperture. Each lenslet produces a spot on the detector array whose location is proportional to the average tilt, θ, of the wave front incident on the subaperture. Spot location, x, is defined as the centroid of the pixel intensities within the spot's main lobe. Given a

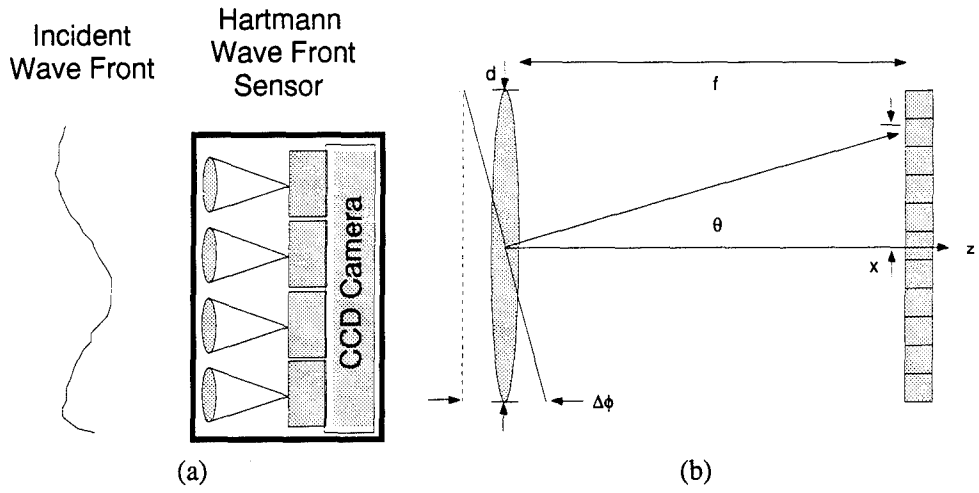

Figure 3.1 Diagram of (a) Hartmann wave front sensor and (b) a single subaperture.

subaperture size d the wave front tilt can be written as,

$$\theta = \tan^{-1}\left(\frac{x}{f}\right), \tag{3.1}$$

where x is the spot location in pixels and f is the focal length of an individual lenslet.

Each subaperture subtends 21 pixels per side in the pixel array and the telescope pupil was imaged onto the lenslet array such that each subaperture corresponds to a distance of three centimeters in the pupil. The main lobe of the diffraction pattern is four pixels wide from peak to first null. Thus, a shift of four pixels corresponds to a $\Delta\phi$ of one wavelength [2]. Using Fraunhoffer diffraction theory [8] the angle, θ, can be written as,

$$\theta \simeq \frac{\lambda}{4d}x, \tag{3.2}$$

where the subaperture width, d, is 3 cm, the laser wavelength, λ, is 0.532 μm, and small angle approximations are used. The slope, s (in rad/m), is calculated using

$$s = \frac{(\theta d)\frac{2\pi}{\lambda}}{d} = \frac{\pi}{2d}x. \tag{3.3}$$

This conversion factor is used to convert from spot centroid locations, x (in pixels), to wave front slopes, s (in radians/m).

The timing used to capture the H-WFS images is also important. The atmosphere is effectively 'frozen' during each measurement since the aircraft flew at approximately 200 m/s. Each WFS image is captured using a single laser pulse 25 ns in duration. The CCD camera frame rate was $1/3$ Hz so the aircraft covered approximately 67 m meters between frames. Each frame is thus affected by independent realizations of atmospheric turbulence. These qualities simplify the corresponding statistical calculations.

3.2 Structure function estimation

The slope structure function is the main statistic we will use to characterize the turbulence encountered by the laser beam. An estimate of the slope structure function can be found by computing the mean square difference of the H-WFS slope measurements between any two subapertures within the pupil of the telescope. This operation corresponds to,

$$\hat{D}_s^{ij}(n,k) = \frac{1}{M}\sum_{m=1}^{M}\left[s_n^i - s_k^j\right]^2 \tag{3.4}$$

where $\hat{D}_s^{ij}(n,k)$ is the estimated slope structure function, M is the number of frames (realizations) in a data set, and s_n^i and s_k^j are the slope measurements at the nth and kth subapertures in the ith and jth directions, respectively. The i and j directions are unit vectors in the x and y directions in a plane perpendicular to the direction of the wave front propagation. The indices i and j may take values of x or y depending on the direction of the slope measurement. The mean is calculated over the ensemble of frames in a particular data set.

When estimating the slope structure function, only slope measurements from the chosen subaperture pairs and slope directions are averaged across the ensemble of frames. Thus, no assumptions are made about the homogeneity or isotropy of the turbulence. However, without these assumptions the slope structure function must be estimated separately for each possible pair of subapertures and four possible slope direction combinations; an enormous number of possibilities. To keep the computations manageable, yet still have a representative sample, the analysis was confined to subaperture separations in the x, y, and $\pm 45°$ directions. Section 3.4 describes how these calculations were implemented.

Not assuming homogeneity or isotropy allows us to test the resulting estimated slope structure functions for these very qualities by examining the behavior of the slope structure function. In

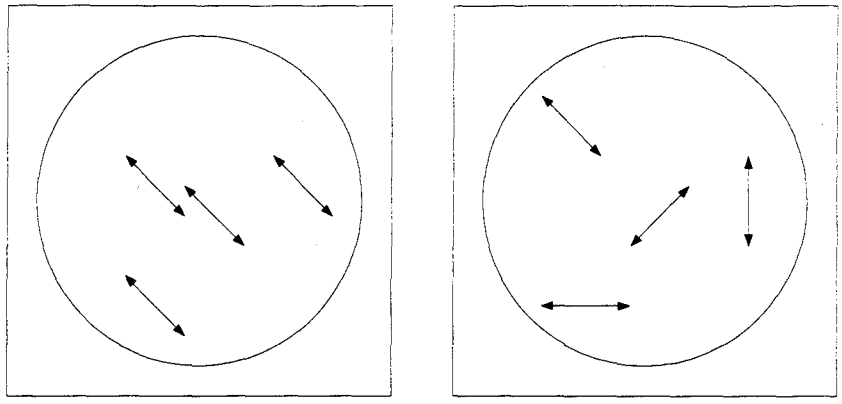

(a) (b)

Figure 3.2 The phase structure function will have the same value for each vector separation shown if the turbulence is (a) homogeneous and (b) isotropic.

Chapter II we found that the slope structure function is a function of the phase structure function. Thus, the behavior of the slope structure function depends on the behavior of the phase structure function.

We can represent any subaperture pair as a vector whose length corresponds to the separation between the subapertures and whose orientation corresponds to the direction in which the subapertures are separated. If the measured turbulence is homogeneous, the phase structure function will depend only on the vector separation between two subapertures and not on the location within the pupil. Thus, the value of the phase structure function corresponding to each of the vectors in Fig. 3.2(a) will be the same. If the measured turbulence is isotropic the values of the phase structure function corresponding of each the vectors in Fig. 3.2(b) will be equal. Isotropic turbulence depends on the magnitude of the separation and not on the orientation.

Now that we know what the WFS sensor measures, and how to estimate the slope structure function, we can process the WFS images to retrieve the slope measurements.

3.3 WFS image processing

The first step is to select a set of WFS images from among the thousands available in several data sets. We would like as many contiguous frames of data as possible to provide a large ensemble to average across. However, there is a tradeoff between ensemble length and the stationarity of the turbulence. We must also account for interruptions in data collection.

The stationarity of the data was primarily gauged by visually assessing the average strength and characteristics of the WFS sensor spot scintillation. Data sets were made as long as possible while keeping the scintillation characteristics similar throughout the data set.

Extracting the WFS slopes requires centering the subaperture grid over the WFS spots as shown in Figure 3.3(a). Unfortunately, the initial grid placement could not be automated because the WFS spots did not appear in the same locations across the data sets. Also, the WFS spots sometimes wandered slightly within a data set. Next, the subapertures not containing a well-formed spot were rejected. This rejection was accomplished by comparing the mean-square error between the magnitude of the subaperture spot's fast Fourier transform (FFT) and magnitude of the FFT an ideal spot to a fixed threshold. Both FFT magnitudes were normalized to have unity peak magnitude. A typical result of this threshold rejection scheme is shown in Figure 3.3(b).

This threshold scheme worked well because the spot position is encoded in the FFT phase, which we ignore. The FFT magnitude is only sensitive to the spot's shape. Subapertures containing only noise and those with highly aberrated spots have large mean-square errors and were rejected.

Once the subaperture grid was defined, the average of the spot centroids was used to place the subaperture grid. This fine centering step ensured that nearly all the overall tilt was removed. Finally, the x and y spot centroid locations within each subaperture was extracted, scaled using Eq.(3.3), and saved in two separate matrices. A mask matrix defining the valid subapertures was also extracted and saved.

The centering operations remove the overall tilt from the H-WFS slopes. As noted earlier, any overall tilt cannot be trusted because it is corrupted by the telescope tracking mechanism and aircraft vibrations. Now we can compute the statistical quantities of interest.

3.4 Statistical analysis

The first statistical quantities computed are the average and variance of the slopes at each subaperture, averaging across the ensemble. Perturbations caused by turbulence are zero mean, so we expect the slope averages to be zero across the aperture. Any non-zero average slope corresponds to a deterministic or slowly varying aberration. In fact, possible aberrations were noticed during the WFS image processing, which made it imperative to closely examine the average slopes.

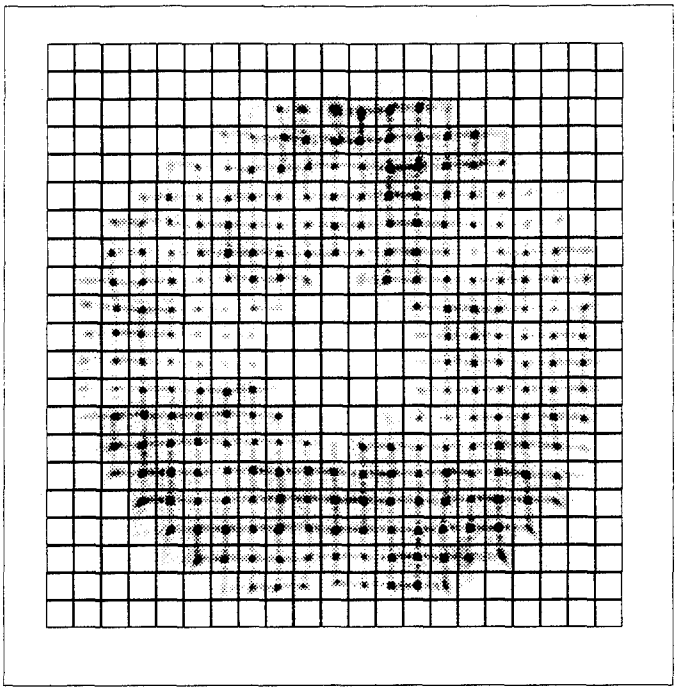

(a)

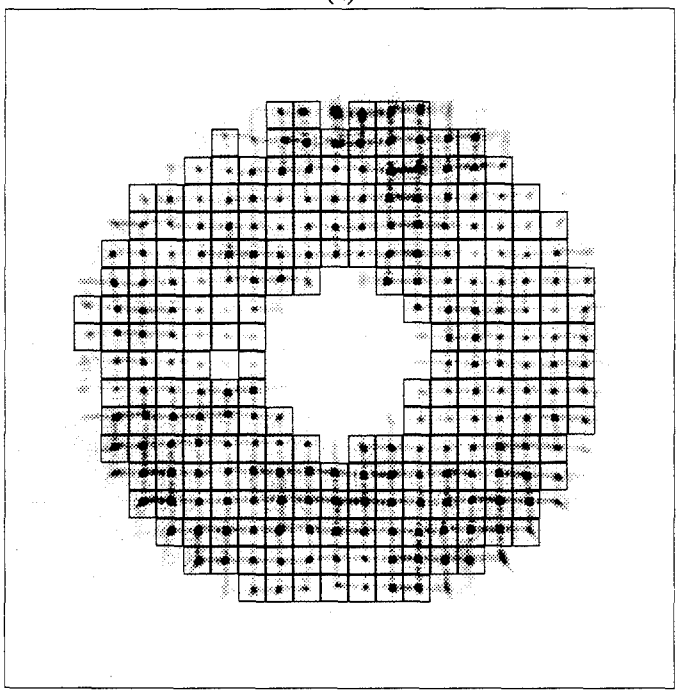

(b)

Figure 3.3 WFS subaperture grid (a) initial placement and (b) after shape thresholding.

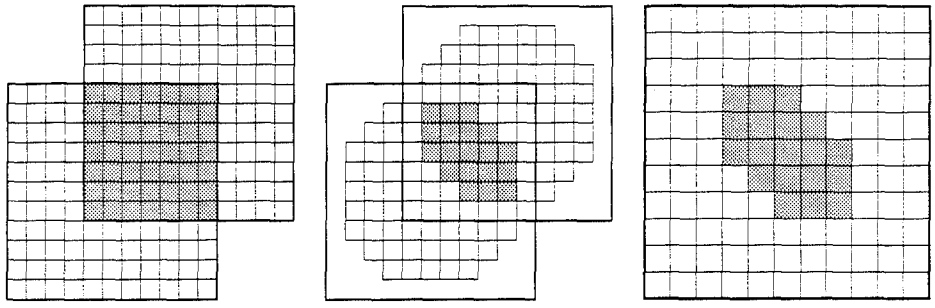

Figure 3.4 Slope differences showing (a) matrix overlap, (b) mask overlap, and (c) difference matrix

Perturbations due to turbulence will not cancel out in the second moment calculation. Removing the average slope should remove most of the effects of any deterministic aberrations. Thus, the slope variance will be primarily a function of the turbulence strength. How uniform the variance is across the aperture gives a rough indication of the homogeneity of the turbulence. Homogeneous turbulence should produce equal variances at each point in the aperture. The value of the variance also serves as a crude measure of the turbulence strength.

Once these global statistics have been calculated, the slope structure function is estimated using Eq. (3.4). As noted at the beginning of this chapter, this estimator makes no assumptions about homogeneity or isotropy. Thus, there are an enormous number of possible separations and directions to consider. Confining the computations to the x, y, and $\pm 45°$ directions and even subaperture separations provides a representative sample while keeping the computations manageable.

The differencing operation in the slope structure function estimator (see Eq.(3.4)) can be computed for each valid subaperture simultaneously by differencing shifted versions of the matrices containing the slopes. Figure 3.4(a) shows a representation of two slope matrices shifted by four subapertures in the $+45°$ direction. The overlap shown by the shaded region contains the only valid separations for this shift value.

Both points in the overlap region may not be within the region defined by the subaperture mask, which changes for each frame. We must also compute the subaperture mask corresponding to the overlap region. The overlap mask is calculated by simply multiplying the shifted mask matrices since the mask matrices consist of ones for valid subapertures and zeros for invalid subapertures. The resulting valid region in the mask matrix is shown by the shaded region in Fig. 3.4(b). This mask

is multiplied with the differenced slope matrix and centered in a matrix the same size as the H-WFS subaperture grid. The resulting matrix is shown in Fig. 3.4(c). The shaded region contains all the valid slope differences for that particular shift direction and separation. Each subaperture position within the matrix corresponds to the center point between the differenced slope locations and contains the differenced slopes.

The shifted mask, the squared slope differences, and the second moment of the squared slope differences are accumulated in running sums. The mask matrix tracks how many measurements are accumulated at each subaperture location. Dividing the accumulated slope differences by the corresponding mask sum produces the structure function estimate at a particular subaperture location.

The accumulated second moment of the squared slope differences allows us to calculate the variance of the squared slope difference's. Using the Tchebycheff inequality allows us to compute a confidence interval for our slope structure function estimate [15]. A 95% confidence interval is calculated using

$$CI_{95} = \pm 4.47\sqrt{\frac{\sigma^2}{n}}, \tag{3.5}$$

where σ^2 is the variance and n is the number of frames in the ensemble. Using the Tchebycheff inequality produces a conservative estimate of the actual confidence interval since no assumptions about the probability distribution function of the structure function are necessary.

The slope structure function estimates are calculated using both the raw slopes and the slopes obtained by subtracting the average slope from each frame. Comparing the raw and average removed structure functions allows us to gauge the effects of removing deterministic aberrations. Now that the estimated slope structure functions are in hand, we can test our results.

3.5 Homogeneity, isotropy, and fit to theory

Before comparing the estimated slope structure functions with the theoretical model developed in Chapter II we must determine if the measured turbulence is actually homogeneous and isotropic. We can examine the variance of the slopes to get a global sense for the homogeneity. The slope variances should be approximately equal across the pupil if the turbulence is homogeneous. How similar the slope structure functions are at various points in the aperture, for a particular shift direction, indicate the homogeneity of the turbulence.

Determining the isotropy of the turbulence is more complicated. From the theoretical results in Chapter II (Fig. 2.1) the structure functions for different shift directions will not be identical and cannot be directly compared. The estimated slope structure functions from Eq.(3.4) can be least-mean-square fit to the normalized theoretical slope structure functions using Eq.(3.6). Since the strength of the turbulence and subaperture size are multiplicative factors we need only estimate a scale parameter. The mean-square fit is computed using

$$d^{-1/3} r_o^{-5/3} = (\mathbf{N}\mathbf{N}^T)^{-1}\mathbf{N}^T\mathbf{D}, \tag{3.6}$$

where $\mathbf{N}$ is the vector containing the theoretically computed normalized slope structure function and $\mathbf{D}$ is the vector containing the estimated slope structure function [20].

The coherence diameter, r_o, can be calculated since the subaperture width, d, is known. Coherence diameters can be compared for various subaperture locations and shift directions to give an indication of homogeneity and isotropy. The root-mean-square error between the estimated and scaled theoretical slope structure functions gives an indication of how well the turbulence is modeled by the Kolmogorov model.

3.6 Simulation results

Before applying the statistical methods described above to real data, we should determine how well these methods perform. Do determine performance we need an ensemble of simulated WFS slope measurements with known statistical properties. An adaptive optics simulation code available at AFIT, `otfsim3`, was used to create such an ensemble [16]. The `otfsim3` code contains a phase screen generator which has been thoroughly tested and is known to produce phase screens with Kolmogorov statistics [16]. The code also simulates a Hartmann WFS.

The phase screen generator and H-WFS simulation modules were used to produce an ensemble of 200 frames of H-WFS measurements for a grid 22 subapertures on a side. Each subaperture side was 4.5 centimeters long when projected into the pupil. A wavelength of $0.523\mu m$ was used for the H-WFS. This wavelength is the laser wavelength used in the ABLE ACE experiments. High light levels were used so the simulated measurements will have very little noise. The r_o value used to in generating the ensemble was 10 centimeters.

Phase screens were generated, the overall tilt was removed, and the resulting phase screen was sent to the H-WFS module. The resulting x and y slope measurements, as well as a subaperture mask, were extracted in the same format as the slope measurements from the real data. Since the simulation code provides slope measurements, the statistical methods were directly applied as described above.

Figures 3.5 and 3.6 show the x and y slope average and variance, respectively. As expected, the average slopes are nearly zero mean. The slope variance is fairly uniform across the pupil.

3.6.1 Homogeneity. The next step is to compute the structure functions. Figures 3.7 and 3.8 show the x and y slope structure functions value versus subaperture separation for various locations within the pupil. Each curve plotted with a dotted line corresponds to a structure function computed at a particular location within the pupil of the telescope. The confidence intervals shown correspond to one of the selected structure functions. The fairly large confidence intervals arise from the finite ensemble used. As expected, for homogeneous turbulence the structure functions cluster together.

3.6.2 Isotropy. Since the simulated turbulence is homogeneous, we can average the structure functions from various locations within the pupil together. The resulting spatially averaged structure function will have many more samples than the non-spatially averaged structure functions and should have much tighter confidence intervals.

Figures 3.9 and 3.10 show the spatially averaged x and y slope structure functions, respectively, for the various separation directions. The dotted line and circles show the estimated structure function. The corresponding theoretical slope structure function, least-squares fit to the estimated structure function, is shown with the solid line.

As expected, the confidence intervals for the spatially averaged structure function are much tighter. The root-mean-square (RMS) error between the estimated and scaled theoretical structure functions is also very small. The value of r_o was recovered to within two significant figures from the scale factor in all cases. The methods work for perfect slope measurements; but what if there are deterministic aberrations?

3.6.3 Effect of aberrations. Deterministic aberrations in the slope measurements can arise from uncompensated aberrations in the optical train used to direct the light from the telescope pupil to the wave front sensor. Such an aberration may influence our structure function estimates.

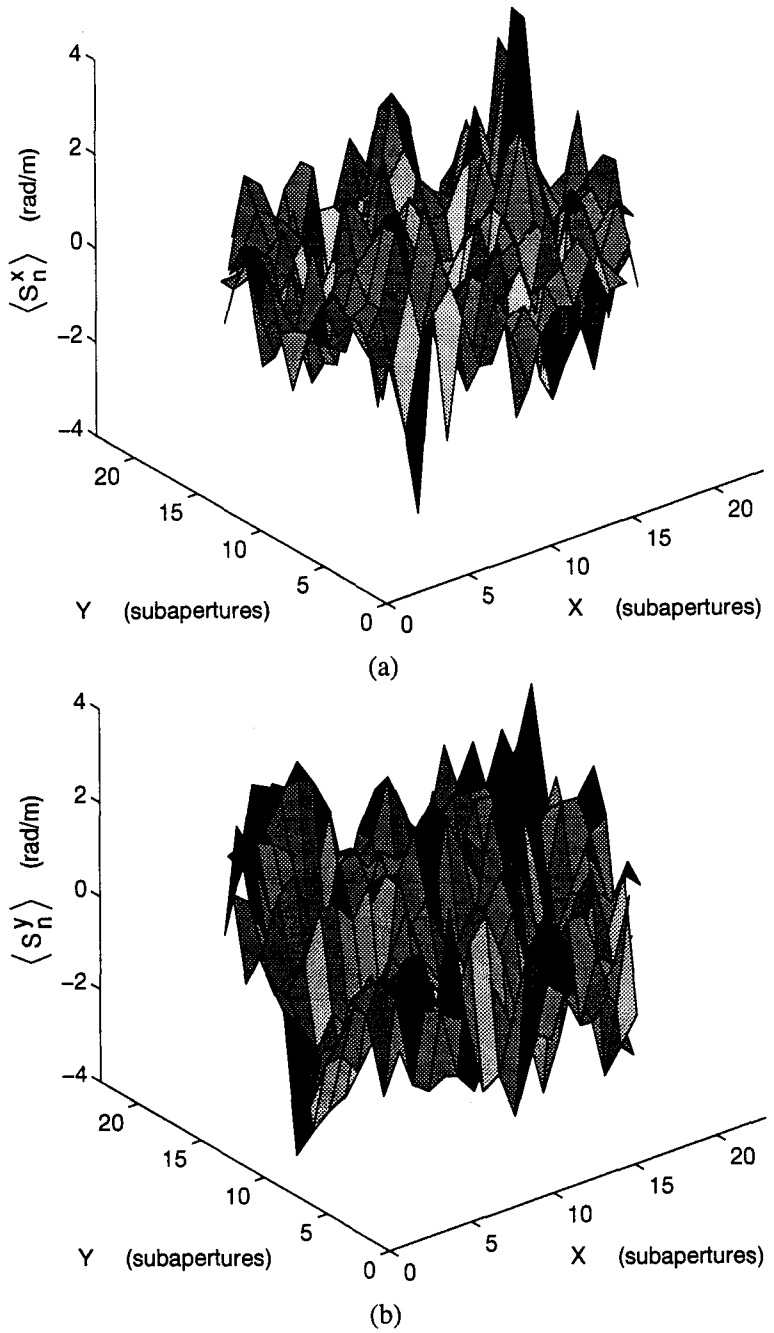

Figure 3.5 Simulation: (a) x-slope average, $\langle s_n^x \rangle$, and (b) y-slope average, $\langle s_n^y \rangle$.

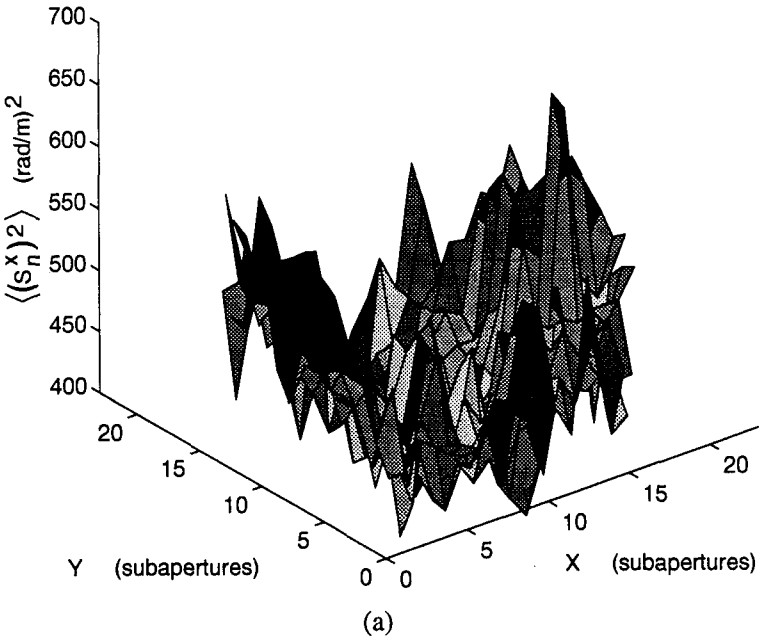

(a)

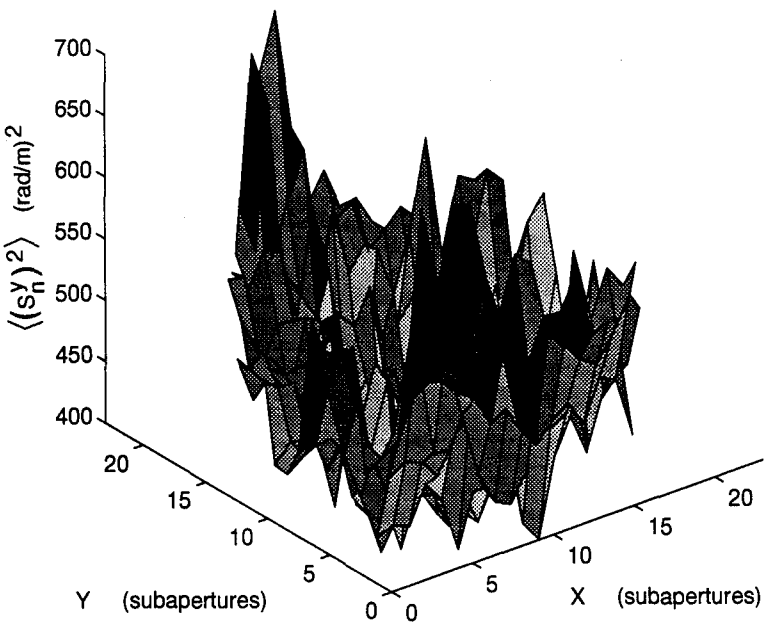

(b)

Figure 3.6 Simulation: (a) x-slope variance, $\langle (s_n^x)^2 \rangle$, and (b) y-slope variance, $\langle (s_n^y)^2 \rangle$.

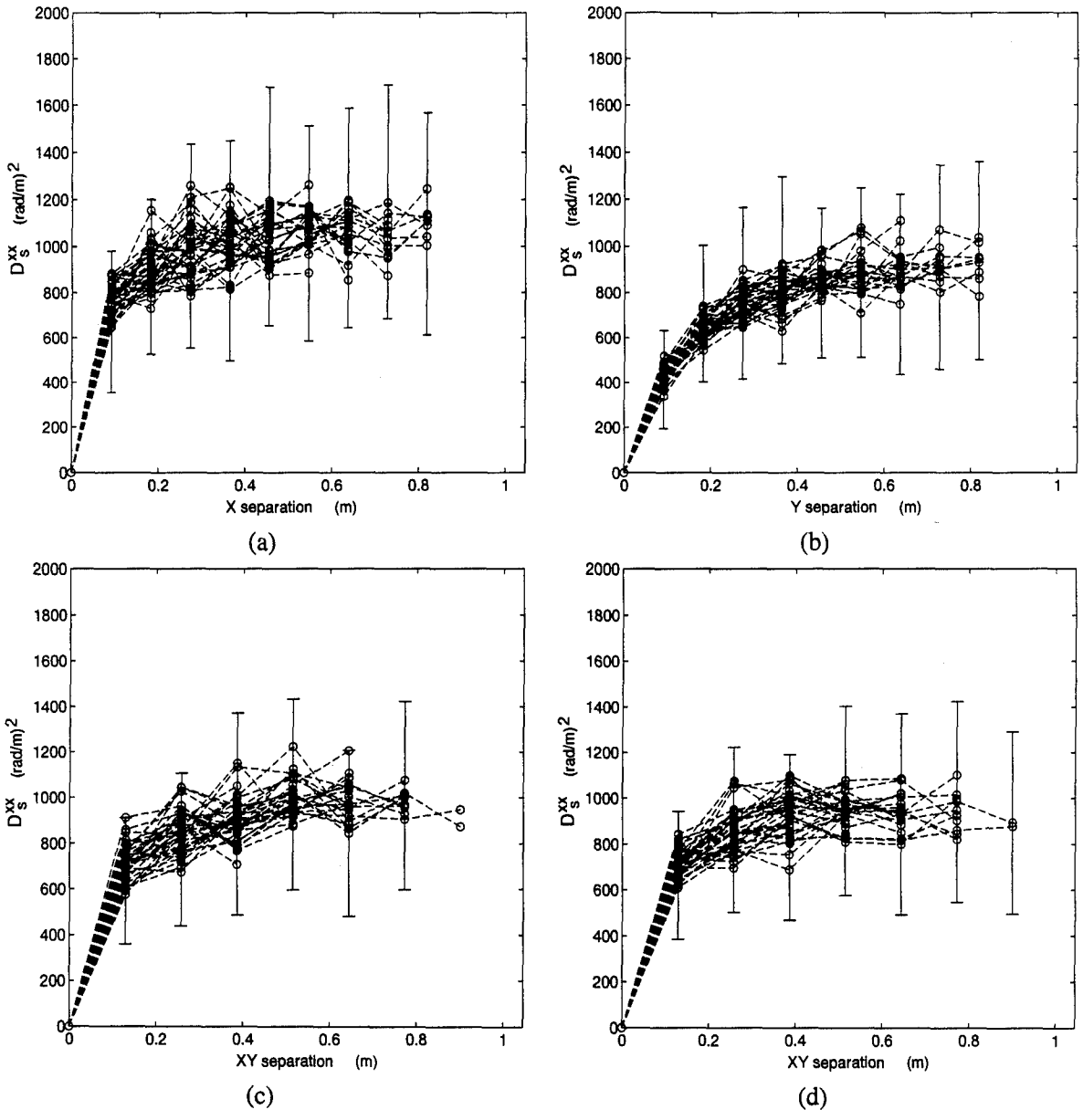

Figure 3.7 Structure function homogeneity, simulation: D_s^{xx} for (a) x, (b) y, (c) $+45°$, and (d) $-45°$ separations.

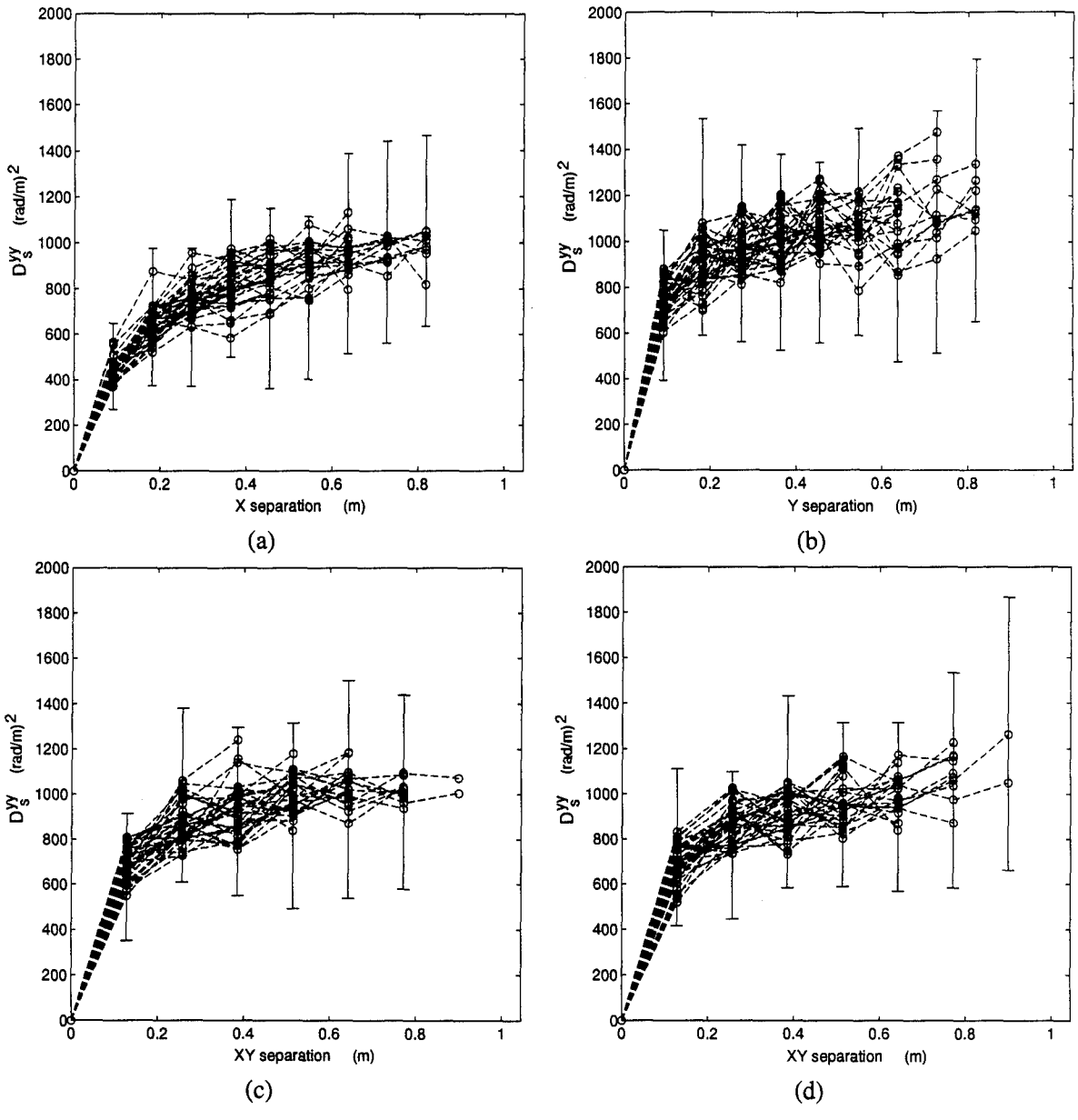

Figure 3.8 Structure function homogeneity, simulation: D_s^{yy} for (a) x, (b) y, (c) $+45°$, and (d) $-45°$ separations.

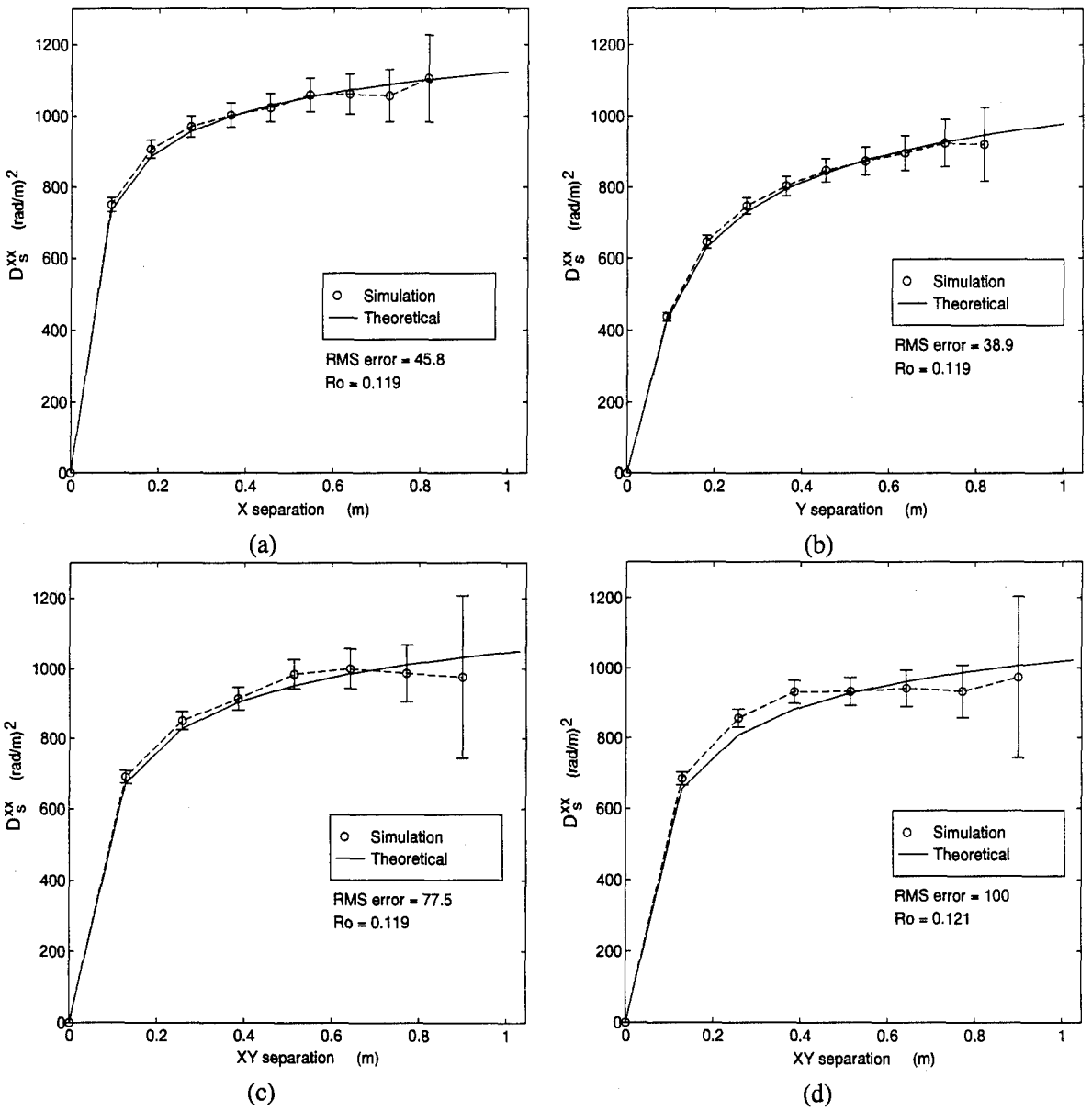

Figure 3.9 Structure function isotropy, simulation: spatially averaged D_s^{xx} for (a) x, (b) y, (c) $+45°$, and (d) $-45°$ separations.

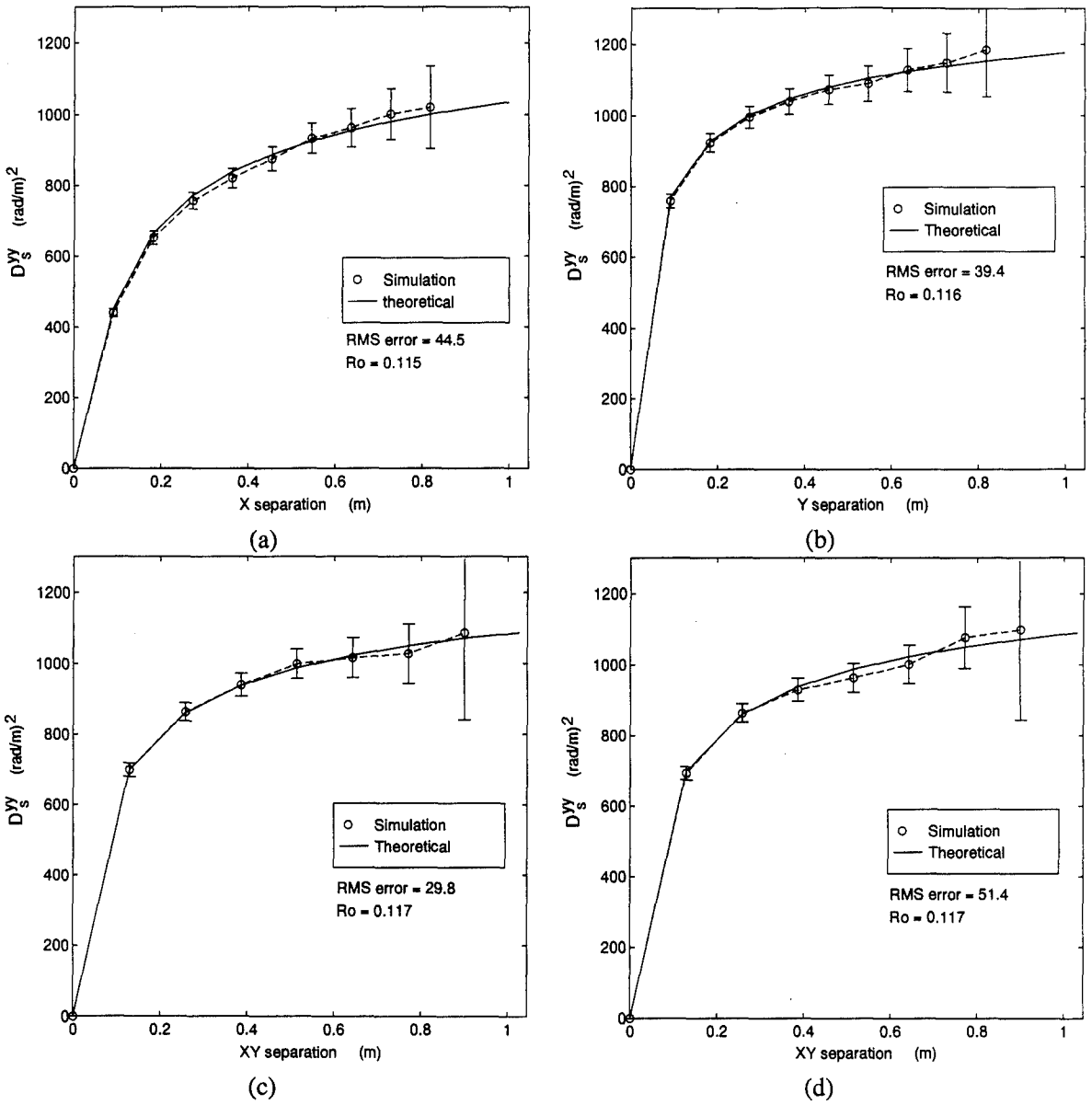

Figure 3.10 Structure function isotropy, simulation: spatially averaged D_s^{yy} for (a) x, (b) y, (c) $+45°$, and (d) $-45°$ separations.

To gauge the effect of deterministic aberrations, a simulated aberration was added to the simulated slopes. The aberration used was a plane tilted in the x or y directions added to the x and y slopes, respectively. The form of this simulated aberration was suggested by the shape of average slope measurements seen in several ABEL ACE data sets.

Again, the average and variance of the slopes were calculated. Figures 3.11 and 3.12 show the x and y slope average and variance, respectively. The deterministic aberration is recovered very well by the slope average calculation. The slope variance is nearly identical to the unaberrated variance. These results suggest that we can recover a deterministic aberration using the slope average. But what effect does this aberration have on our structure functions?

Figure 3.13 shows the x slope structure functions for the various shift directions from selected locations within the pupil. Others follow by symmetry. Homogeneity is not destroyed by this particular aberration. The shape of the structure functions is distorted, especially at the larger separations.

Figure 3.14 shows the spatially averaged x-slope structure functions for the various shift directions. Large RMS errors occur between the estimated and scaled theoretical structure functions. The recovered r_o values are approximately two centimeters low. The fit between estimate and theory in Fig. 3.14(b) is an artifact of the particular aberration used and will not in general happen. Can we improve the performance of our methods by removing the average slope before estimating the structure functions?

3.6.4 Effect of average removal. The average slope calculation closely estimated the aberration added to the simulated slope measurements. Thus, we should be able to correct for a deterministic aberration by subtracting the average slope from each frame of WFS slope measurements before estimating the slope structure functions.

Figure 3.15 shows the average removed x slope structure functions for the various separation directions from selected locations within the pupil. The structure functions are now nearly identical to the results from the unaberrated slope measurements.

Figure 3.16 shows the average removed, spatially averaged x slope structure functions for the various shift directions. The shape of the structure functions again matches the theoretical slope structure functions and the RMS error has been reduced. The recovered r_o values are nearly identical to those recovered from the unaberrated slope measurements.

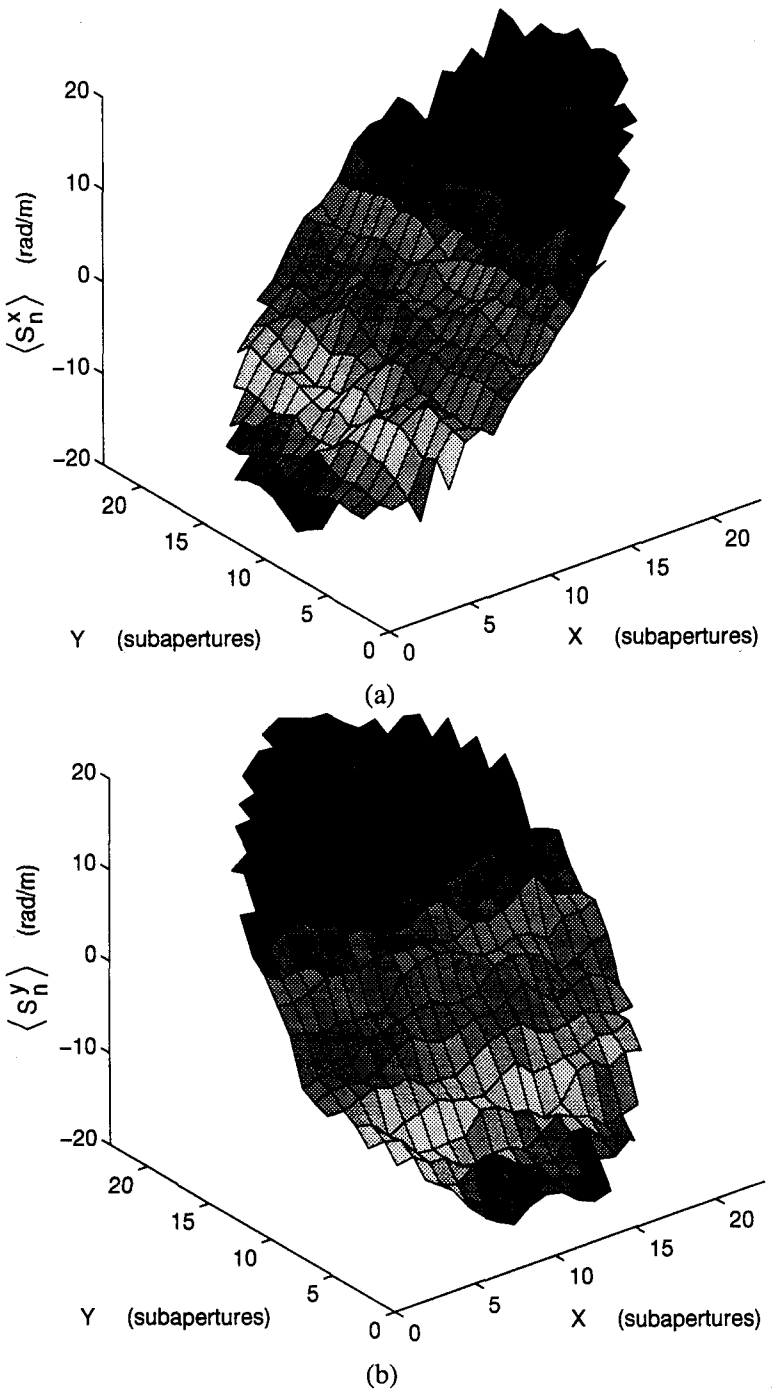

Figure 3.11 Simulation with aberration: (a) x-slope average, $\langle s_n^x \rangle$, and (b) y-slope average, $\langle s_n^x \rangle$.

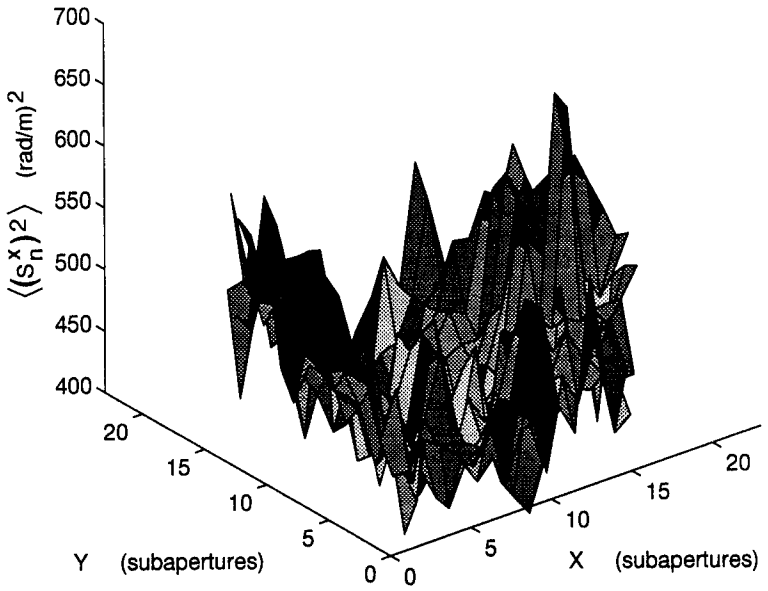

(a)

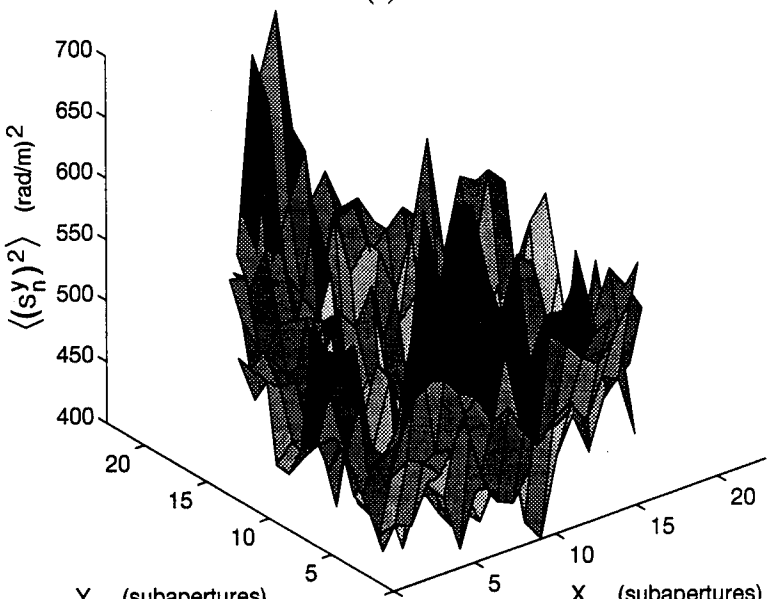

(b)

Figure 3.12 Simulation with aberration: (a) x-slope variance, $\langle (s_n^x) \rangle$, and (b) y-slope variance, $\langle (s_n^y) \rangle$.

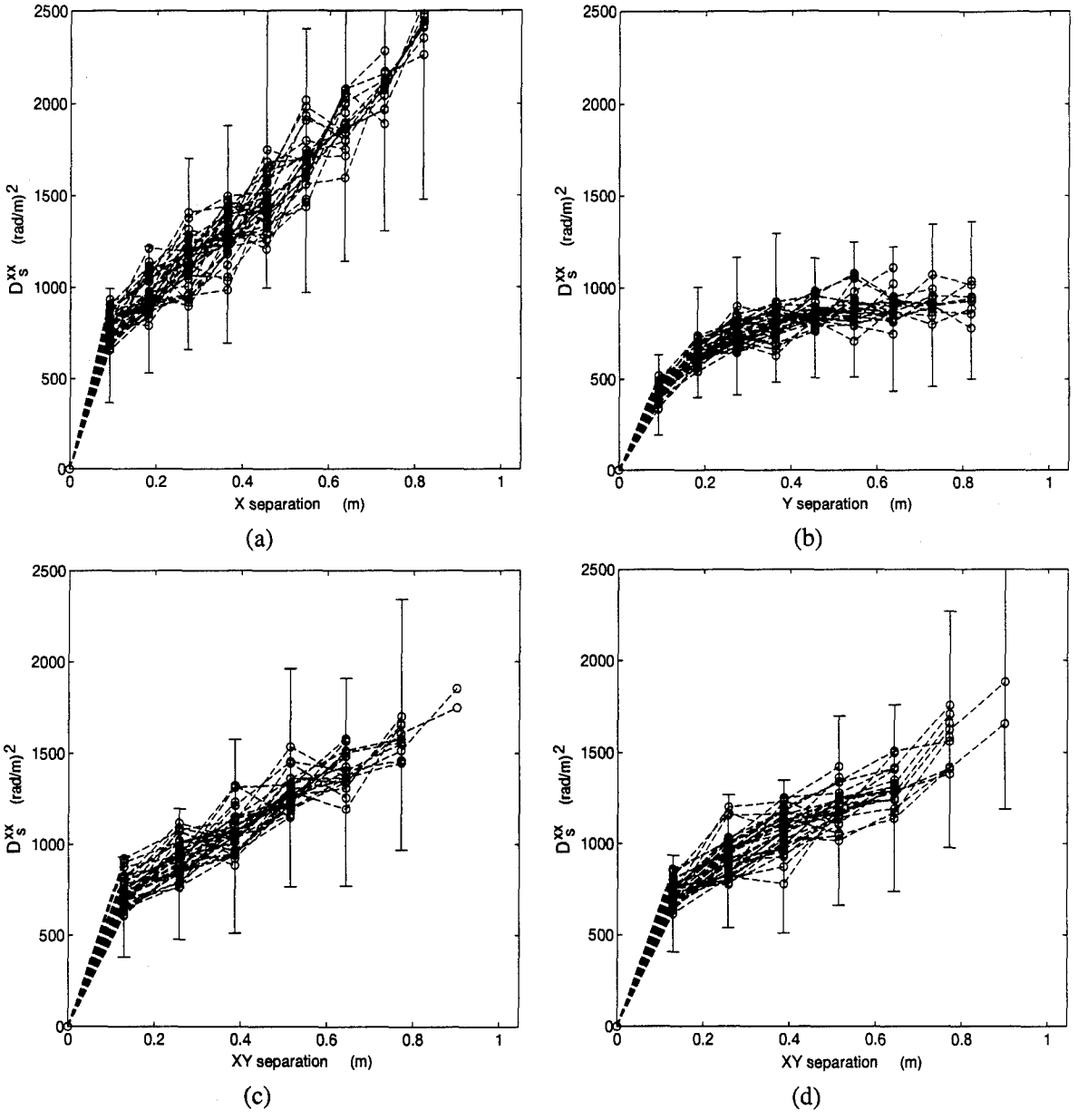

Figure 3.13 Structure function homogeneity, simulation: D_s^{xx} for (a) x, (b) y, (c) $+45°$, and (d) $-45°$ separations. Aberrated slope measurements.

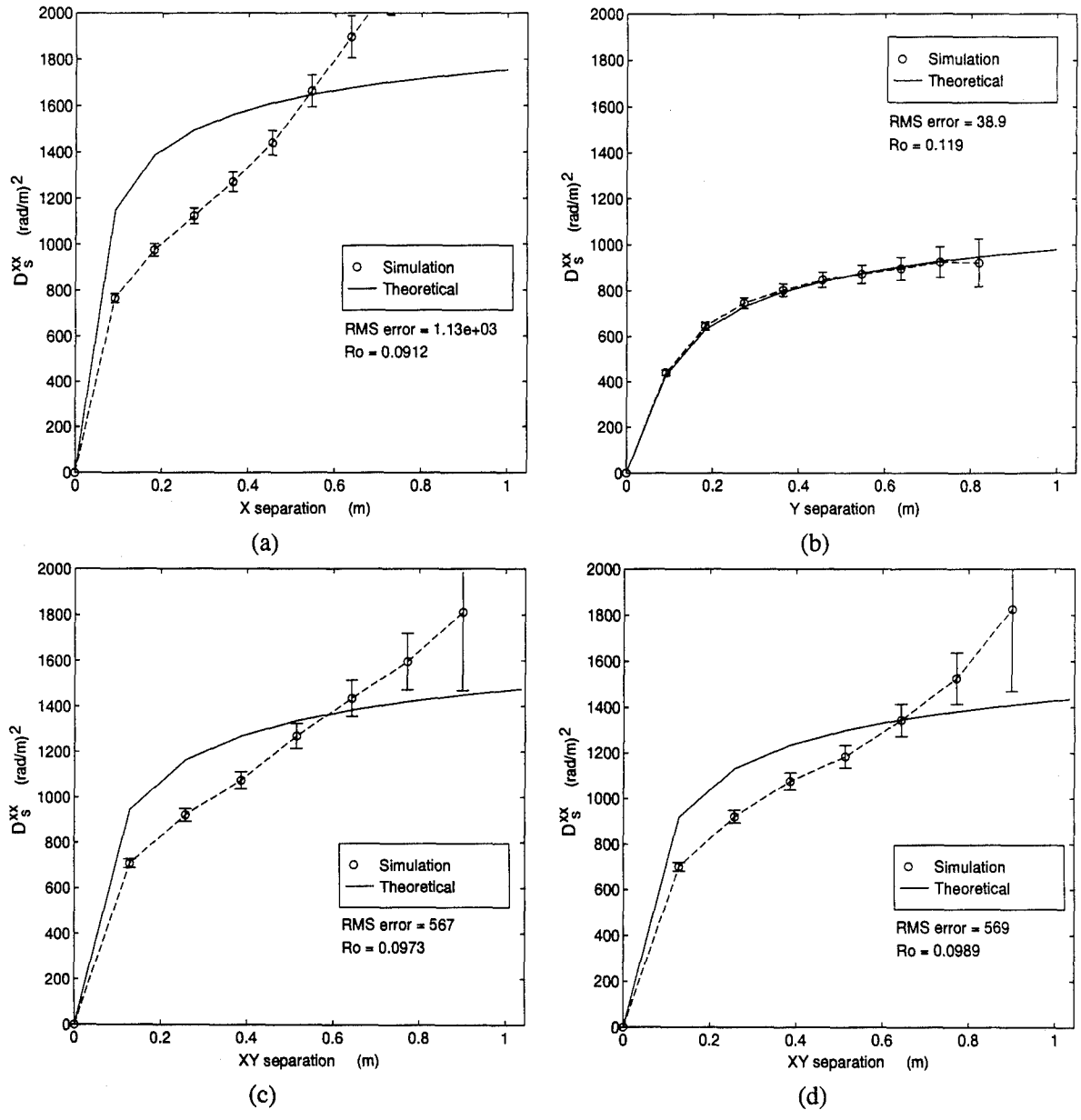

Figure 3.14 Structure function isotropy, simulation: D_s^{xx} for (a) x, (b) y, (c) $+45°$, and (d) $-45°$ separations. Aberrated slope measurements.

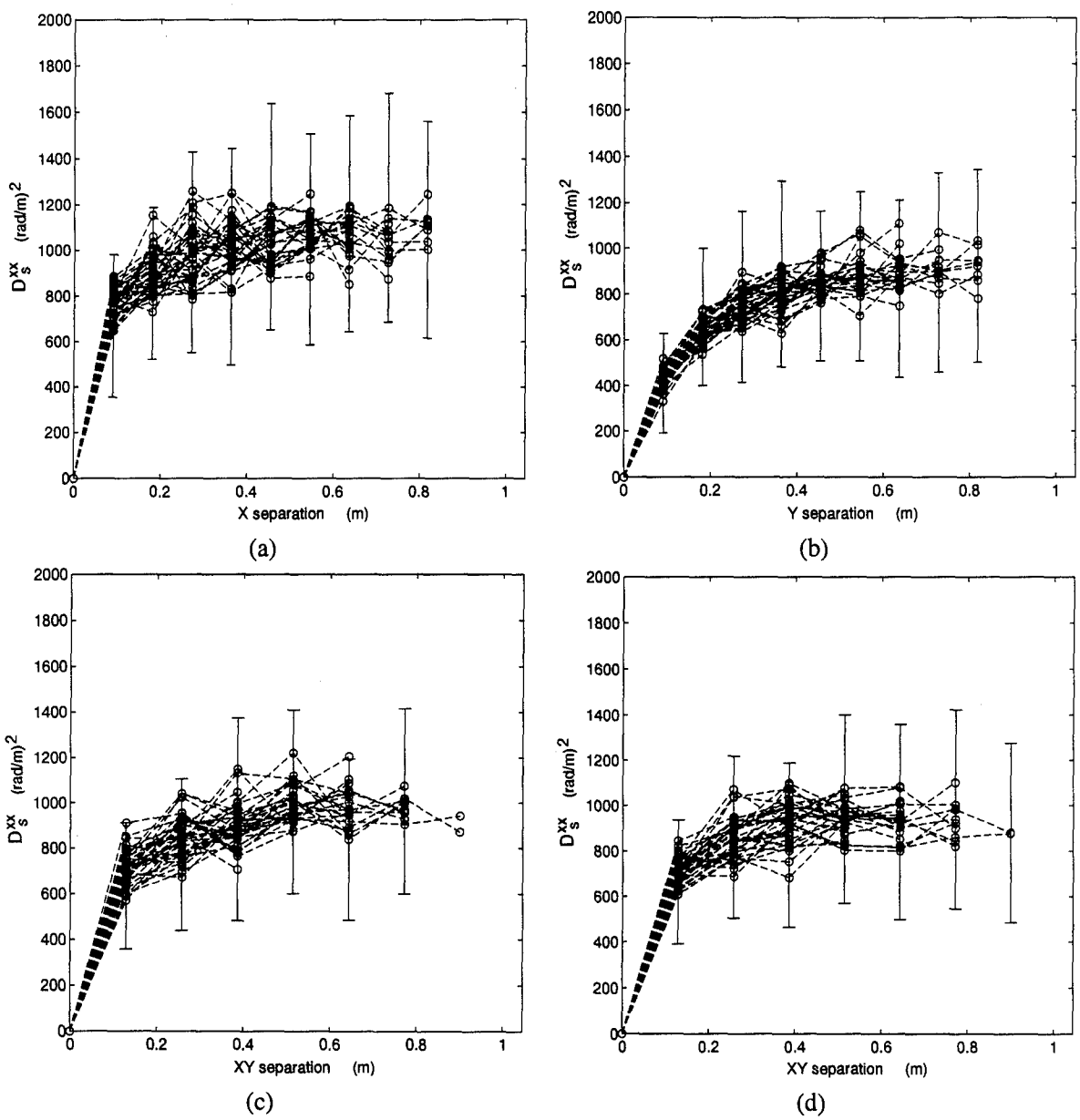

Figure 3.15 Structure function homogeneity, simulation: D_s^{xx} for (a) x, (b) y, (c) $+45°$, and (d) $-45°$ separations. Average slope removed.

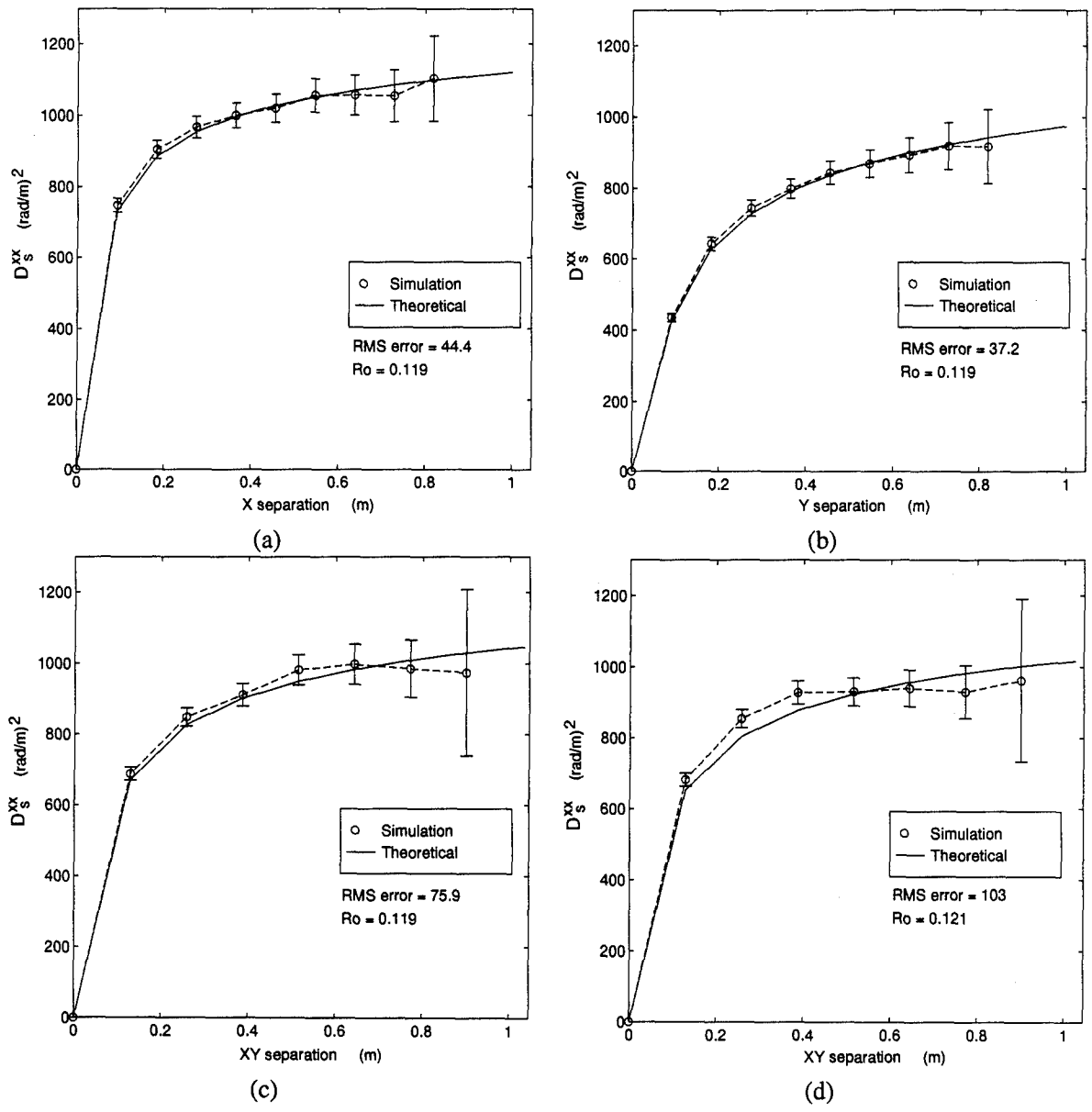

Figure 3.16 Structure function isotropy, simulation: D_s^{xx} for (a) x, (b) y, (c) $+45°$, and (d) $-45°$ separations. Average slope removed.

3.7 Observations

Using the H-WFS slope measurements directly to sense atmospheric turbulence appears to be feasible. The slope structure function confines us to a discrete set of separations, defined by the subaperture grid. Phase reconstruction would be more flexible since we would not be confined to the subaperture locations. However, the computational burden would be much higher.

Removing the overall tilt is a tradeoff. The overall tilt contains approximately 87% of the total power in the turbulence, so the remaining higher order modes are correspondingly weak [6]. The counterpoint is that removing the overall tilt removes exactly those modes which are corrupted by the telescope tracking and aircraft motion. Also, the self slope structure function is insensitive to overall tilt so we cannot learn anything about overall tilt anyway.

Based on performance with simulated slope measurements we can use the structure function estimator to recover the slope structure function. Removing the average slope from the slope measurements was shown to be an important step. The average slopes must be removed before computing the slope structure functions. Average removal allows us to remove the effects of deterministic aberrations in our slope measurements. Now we can analyze the actual ABLE ACE data.

IV. ABLE ACE Data Analysis

This chapter presents the results of the calculations outlined in Chapter III. The results are analyzed to determine the homogeneity and isotropy of the turbulence, and to compare the results with the theory developed in Chapter II. The first section describes the parameters of each of the ABLE ACE data sets analyzed. The following sections present the results and analysis of the statistical and slope structure function calculations.

4.1 ABLE ACE data sets

The ABLE ACE experiment gathered data over a three month period at various locations within the continental United States and overseas. The primary purpose was to gather data on turbulence in the stratosphere; thus, the aircraft altitudes ranged between 35,00-45,000 feet. Many different separations between the aircraft were used, ranging from twenty kilometers to over one hundred kilometers.

The data sets analyzed were chosen to span the range of aircraft separations, provide a sampling of the various geographic locations, and to produce fairly long ensembles of frames for the statistical calculations. Even so, these results barely scratch the surface of the gigabytes of data available.

Table 4.1 provides the aircraft separation, altitude, and number of frames in each data set. Several thousand WFS frames, representing several hours of data collection, were examined to select the hundreds of frames used. The data sets in Table 4.1 were analyzed using the procedures outlined in Chapter III. The results for the *Science3* data set are presented in the remainder of this chapter.

4.2 The Science3 *data set*

The *Science3* data set was chosen for a detailed presentation because the characteristics and trends of this data set are representative. The analysis for the remaining data sets is found in Appendix A.

Data Set	Separation	Altitude	Frames
Yokota3-1	22-27 km	44,500 ft	112
Science3	58-59 km	40,000 ft	114
Yokota3-2	59-63 km	43,000 ft	150
Osan2	103-105 km	41,500 ft	71
Science2	107-110 km	41,500 ft	206

Table 4.1 Parameters of the ABLE ACE data sets analyzed.

A few results from other data sets are presented when those results are exceptions to the general trends illustrated by the Science3 data set.

One of the major difficulties encountered in analyzing the results are gaps in the structure function calculations produced by the central obscuration of the telescope. These gaps arise since both slope measurements differenced in the structure function calculations are not always within the pupil of the telescope. Another difficulty is the finite ensemble length. The short ensembles available, coupled with the fact that all subaperture locations are not always valid, can produce statistically unreliable points. Structure function values calculated using fewer than 75% of the possible ensemble samples are removed during the analysis. Once the unreliable structure function estimates are removed we can examine the global slope statistics.

4.2.1 Global statistics. The mean and variance of the slope measurements were computed in an effort to discover any deterministic aberrations and the strength of the turbulence across the telescopes pupil. The x and y slope averages for the *Science3* data set are shown in Fig. 4.1.

Atmospheric turbulence should be zero mean. The *Science3* slope averages are not zero mean; which suggests some deterministic aberration is present. The aberrations for the *Science3* data set are not particularly large. A data set with a much larger and more consistent aberration was the *Osan2* data set. The slope averages for the *Osan2* data set are shown in Fig. 4.2. The aberration in this data set was noticed during the WFS image processing and provided the impetus to analyze all the WFS slope measurements for any deterministic aberrations.

The slope variances for the *Science3* data set are shown in Fig. 4.3. The slope variances are fairly uniform across the telescope's pupil. Homogeneous turbulence would produce slope variances which are uniform across the telescope's pupil. Thus, a fairly uniform slope variance across the pupil suggests that the turbulence encountered was indeed homogeneous. This characteristic held for all the data sets analyzed. Homogeneity of the turbulence can also be tested by examining the estimated structure functions.

4.2.2 Testing for homogeneity. Once the global statistics were known the self slope structure functions were computed. Gaps in the structure functions caused by the central obscuration require us to plot structure functions from several locations to observe the overall behavior. Confidence intervals

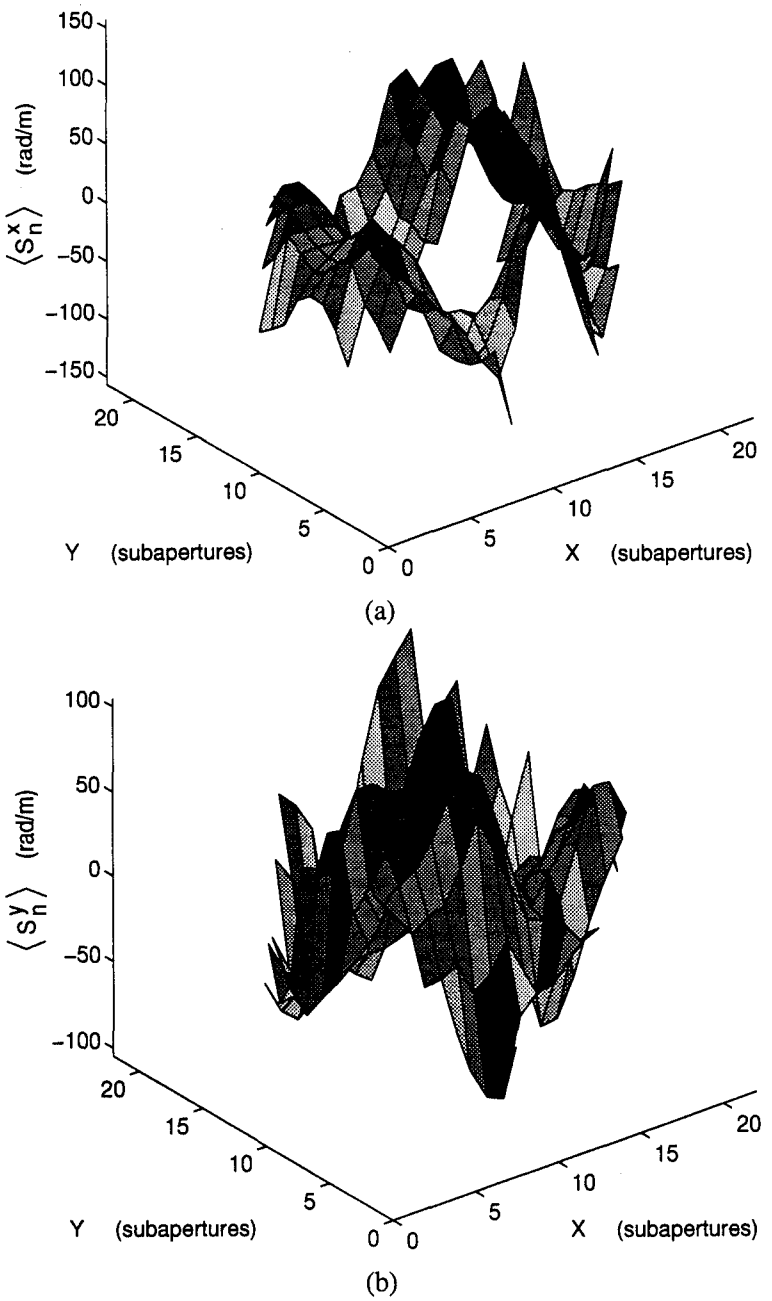

Figure 4.1 Science3: (a) x-slope average, $\langle s_n^x \rangle$, and (b) y-slope average, $\langle s_n^y \rangle$.

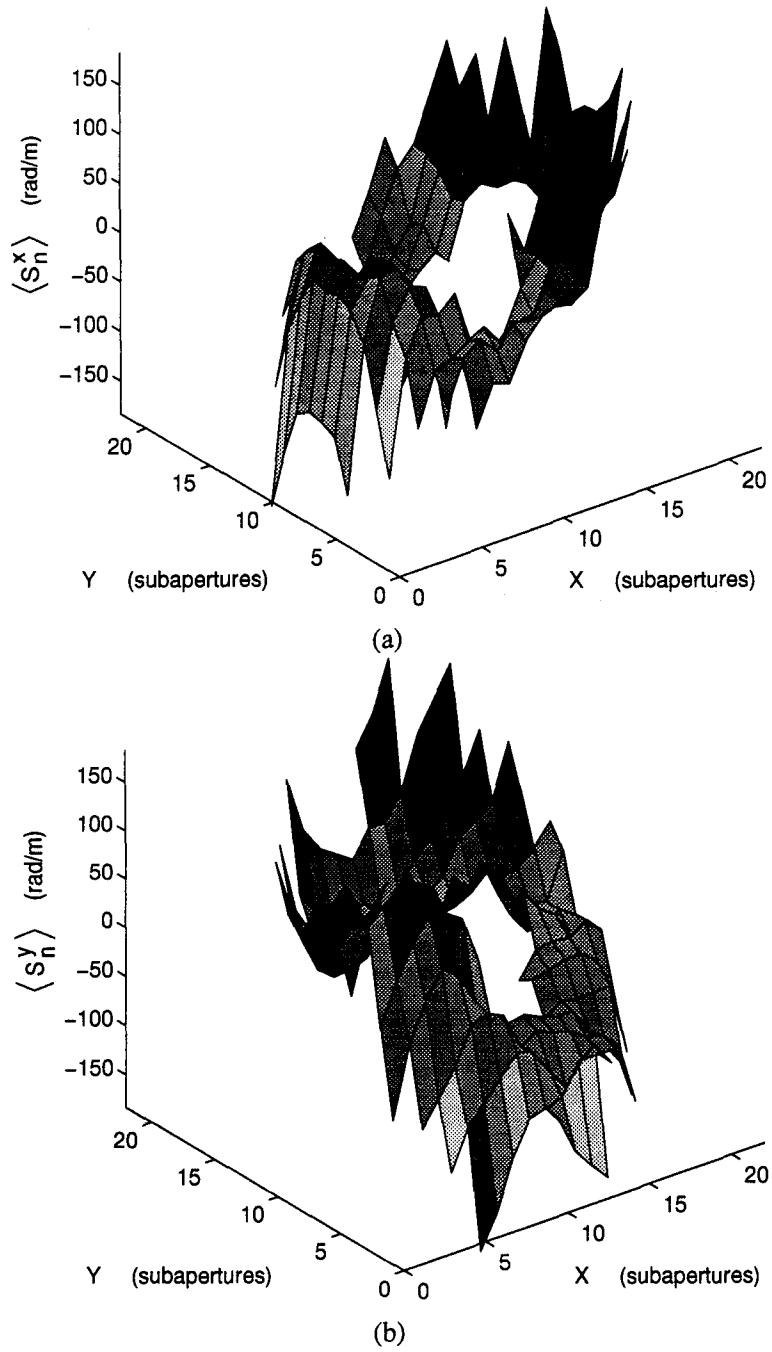

Figure 4.2 Osan2: (a) x-slope average, $\langle s_n^x \rangle$, and (b) y-slope average, $\langle s_n^x \rangle$.

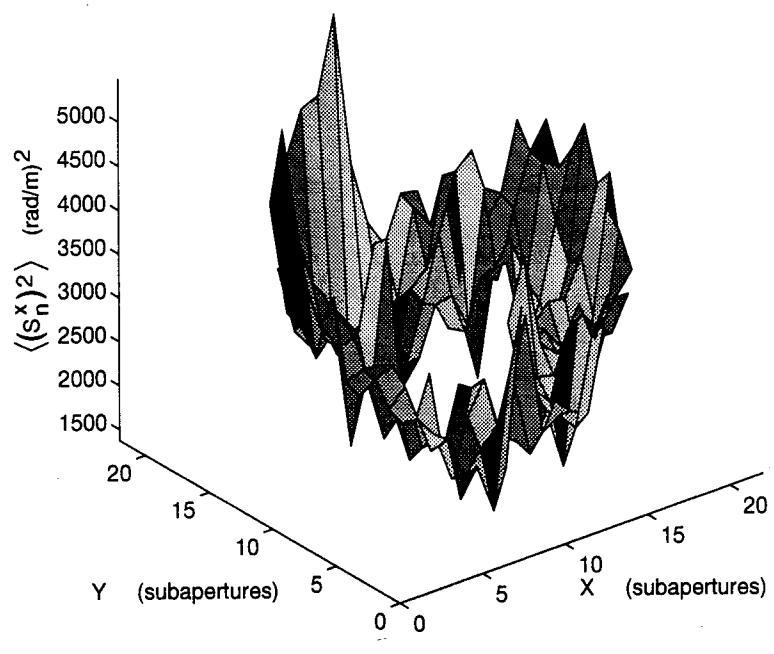

(a)

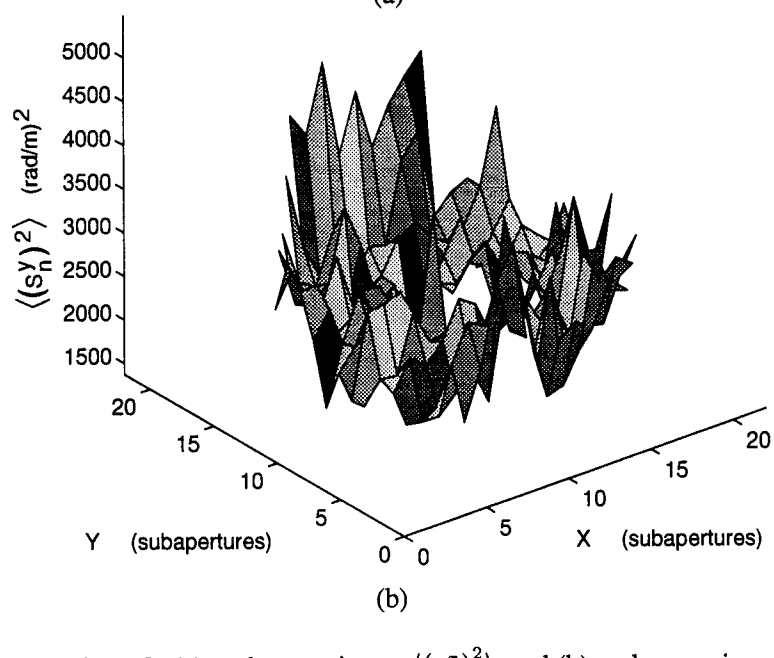

(b)

Figure 4.3 Science3: (a) x-slope variance, $\langle(s_n^x)^2\rangle$, and (b) y-slope variance, $\langle(s_n^y)^2\rangle$

for several structure functions are shown to give a feeling for how the confidence intervals behave. The many outliers and relatively large confidence intervals arise primarily from the limited ensemble length.

Figures 4.4 and 4.5 show the self slope structure functions without average removal. Structure functions from many locations in the pupil have been plotted. The circles show the estimated structure function values. The dotted lines show the various structure functions. Solid vertical lines show the 95% confidence intervals. The structure functions do cluster together slightly. Nevertheless, there are still many outliers, and the confidence intervals are very large compared to the estimated structure function values.

Figures 4.7 and 4.6 show the self slope structure functions with average removal. As shown in Chapter III removing the average slope can compensate for deterministic aberrations which may be present. Such aberrations will affect the estimated structure functions. With average slope removal the structure function clustering is more apparent. The confidence intervals have also been markedly reduced; although, they are still large.

Overall, the structure functions tend to cluster together. But with confidence intervals nearly the size of the structure function values. How closely the structure functions cluster together is an indication of the homogeneity of the turbulence. Combining these observations with the uniformity of the global slope variances tends to support, but does not confirm, the homogeneity of the atmospheric turbulence encountered.

4.2.3 Testing for isotropy. We cannot directly compare the self slope structure functions for various separation directions since the structure functions are not identical. Providing the turbulence is homogeneous, we can spatially average the slope structure functions. Spatial averaging will effectively increase the size of our ensemble and provide a better estimate of the slope structure function. We can then least-squares fit the estimated and theoretical structure functions. If the turbulence is isotropic, the r_o values recovered from the least-square fit scale factor should be nearly the same value.

Figures 4.8 and 4.9 show the spatially averaged self slope structure functions without average removal. Figures 4.10 and 4.11 show the spatially averaged self slope structure functions with without average removal.

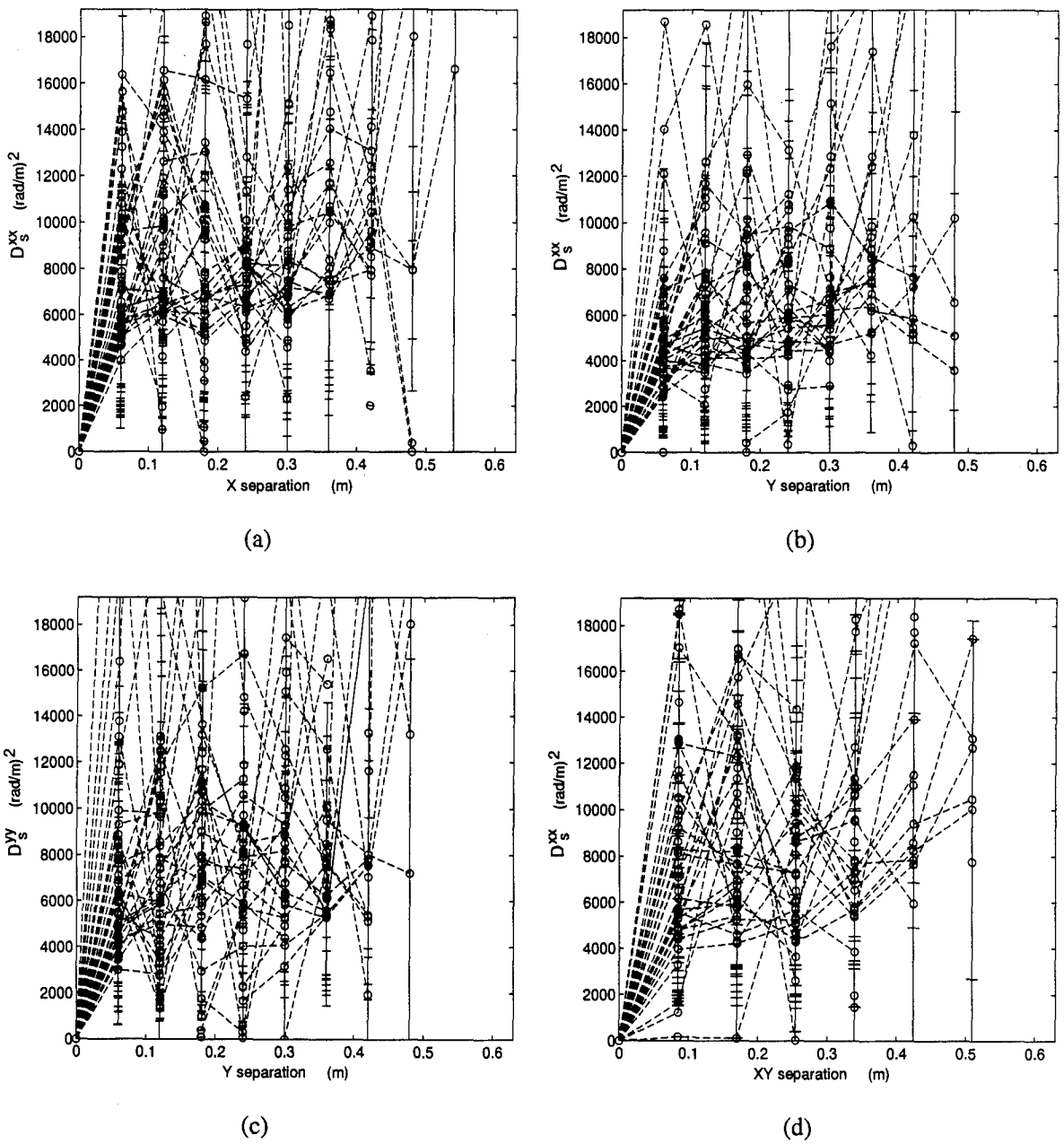

Figure 4.4 Structure function homogeneity: D_s^{xx} for (a) x, (b) y, (c) $+45°$, and (d) $-45°$ separations. Average slopes were not removed.

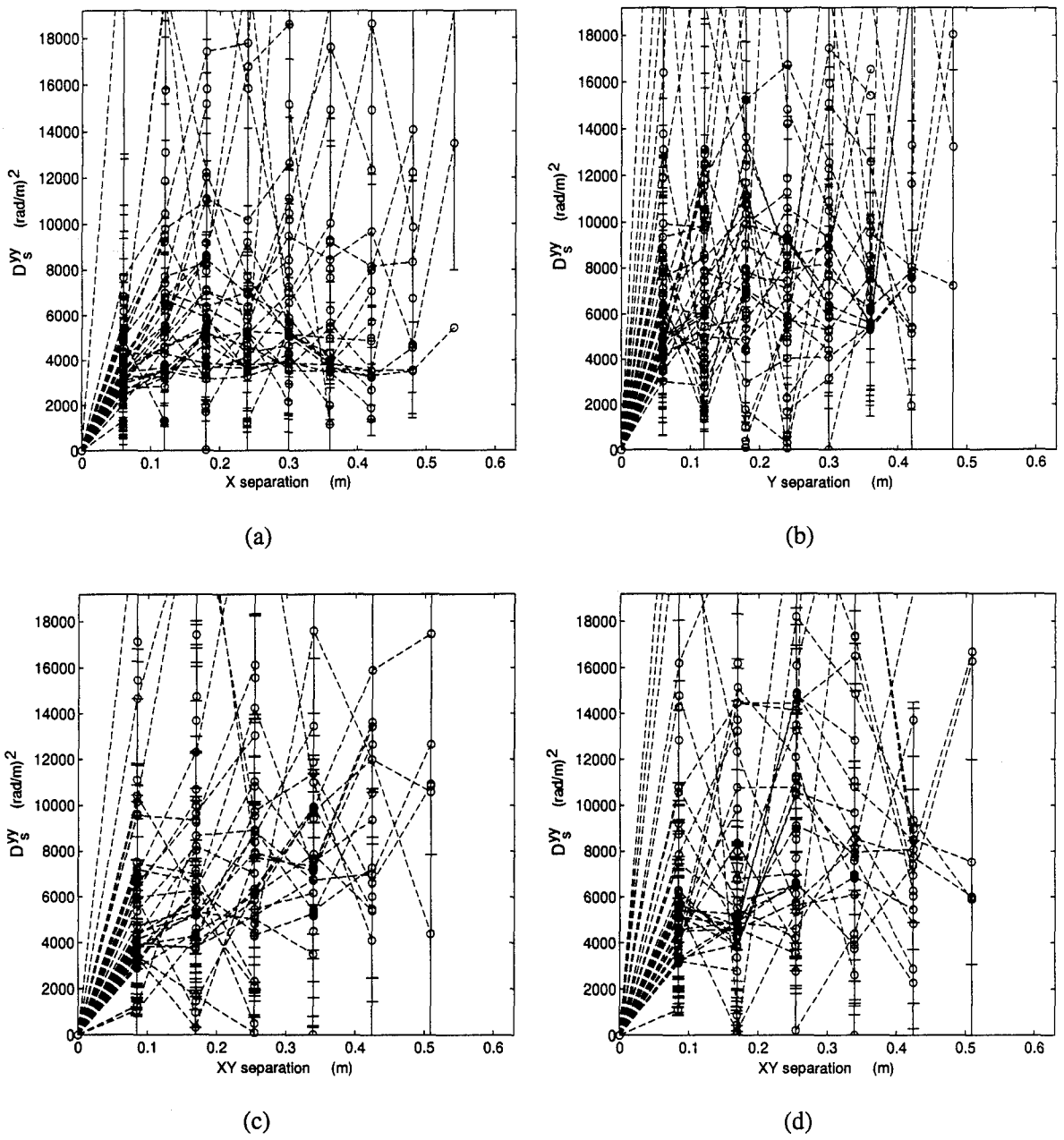

Figure 4.5 Structure function homogeneity: D_s^{yy} for (a) x, (b) y, (c) $+45°$, and (d) $-45°$ separations. Average slopes were not removed.

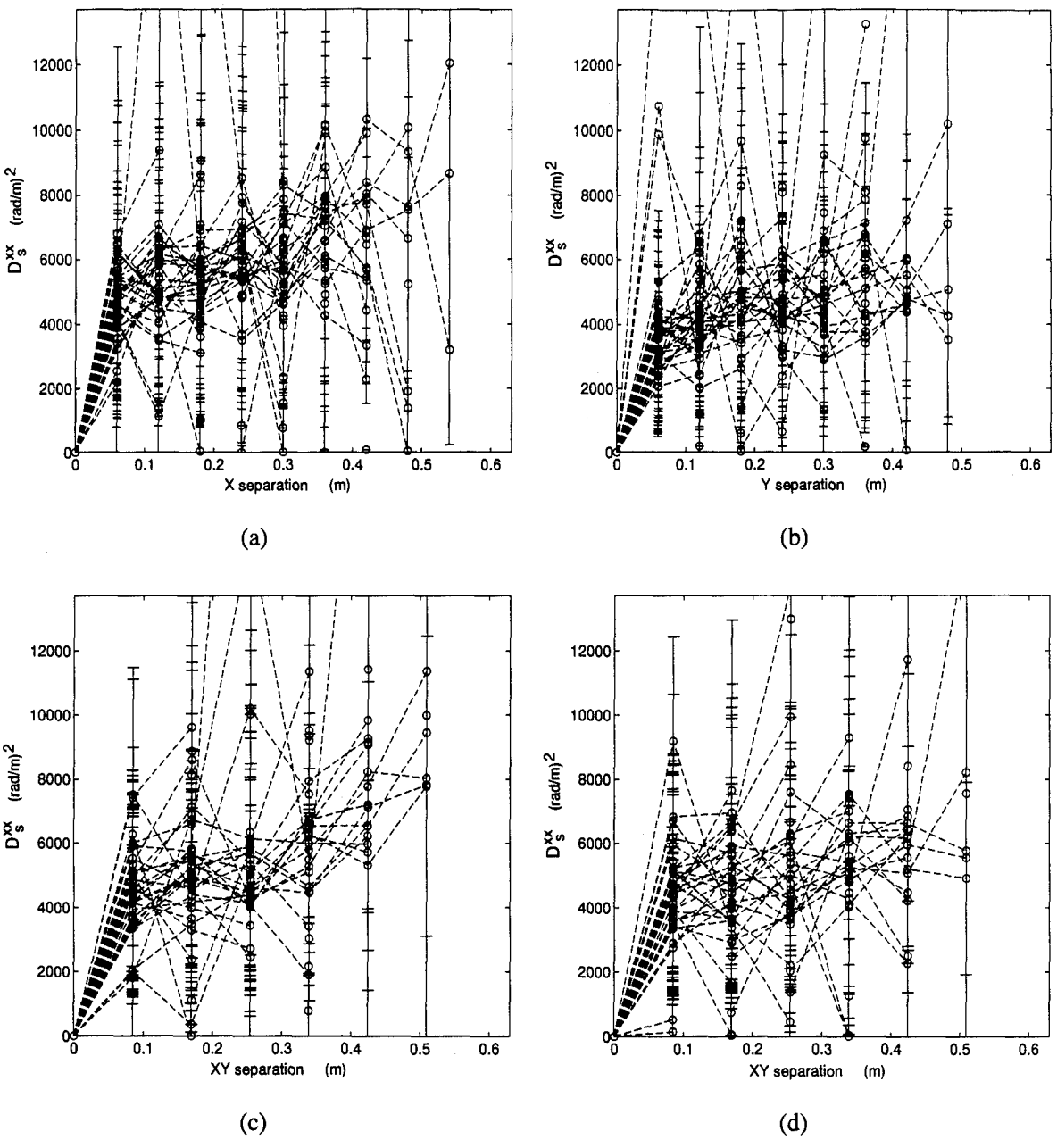

Figure 4.6 Structure function homogeneity: D_s^{xx}-slopes shifted in for (a) x, (b) y, (c) $+45°$, and (d) $-45°$ separations. Average slopes removed.

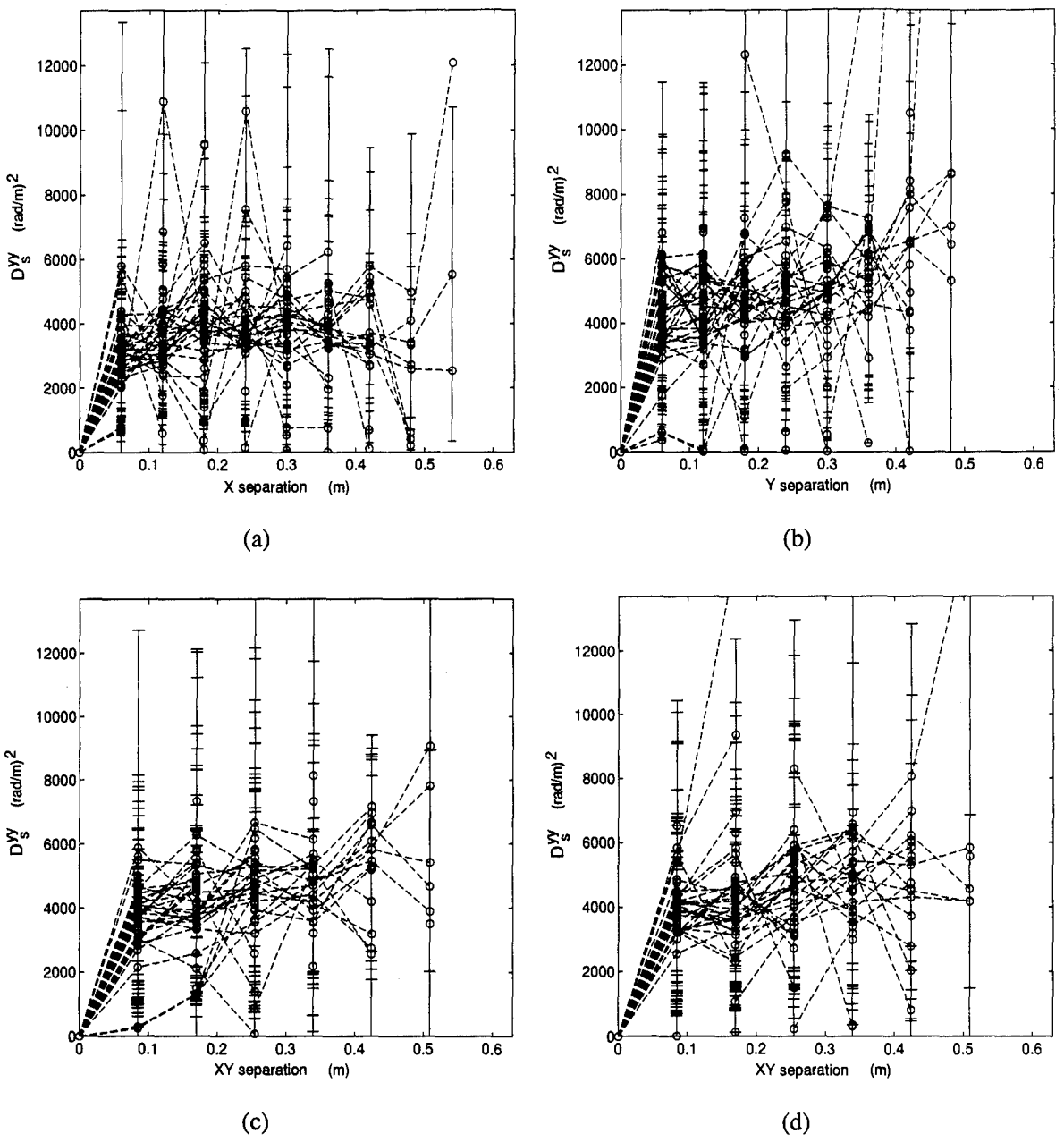

Figure 4.7 Structure function homogeneity: D_s^{yy} for (a) x, (b) y, (c) $+45°$, and (d) $-45°$ separations. Average slopes removed.

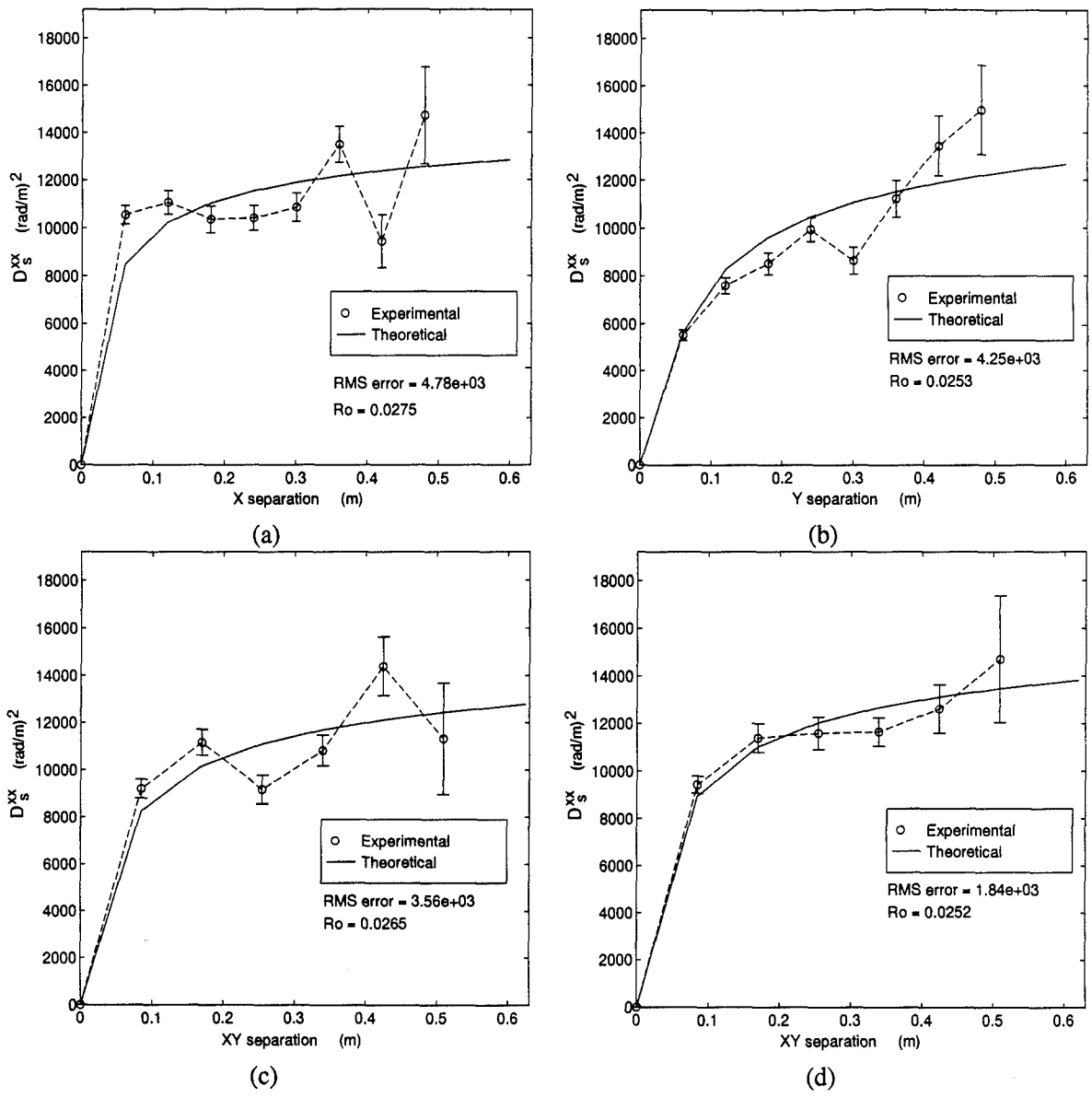

Figure 4.8 Structure function isotropy: spatially averaged D_s^{xx} for (a) x, (b) y, (c) $+45°$, and (d) $-45°$ separations. Average slopes not removed.

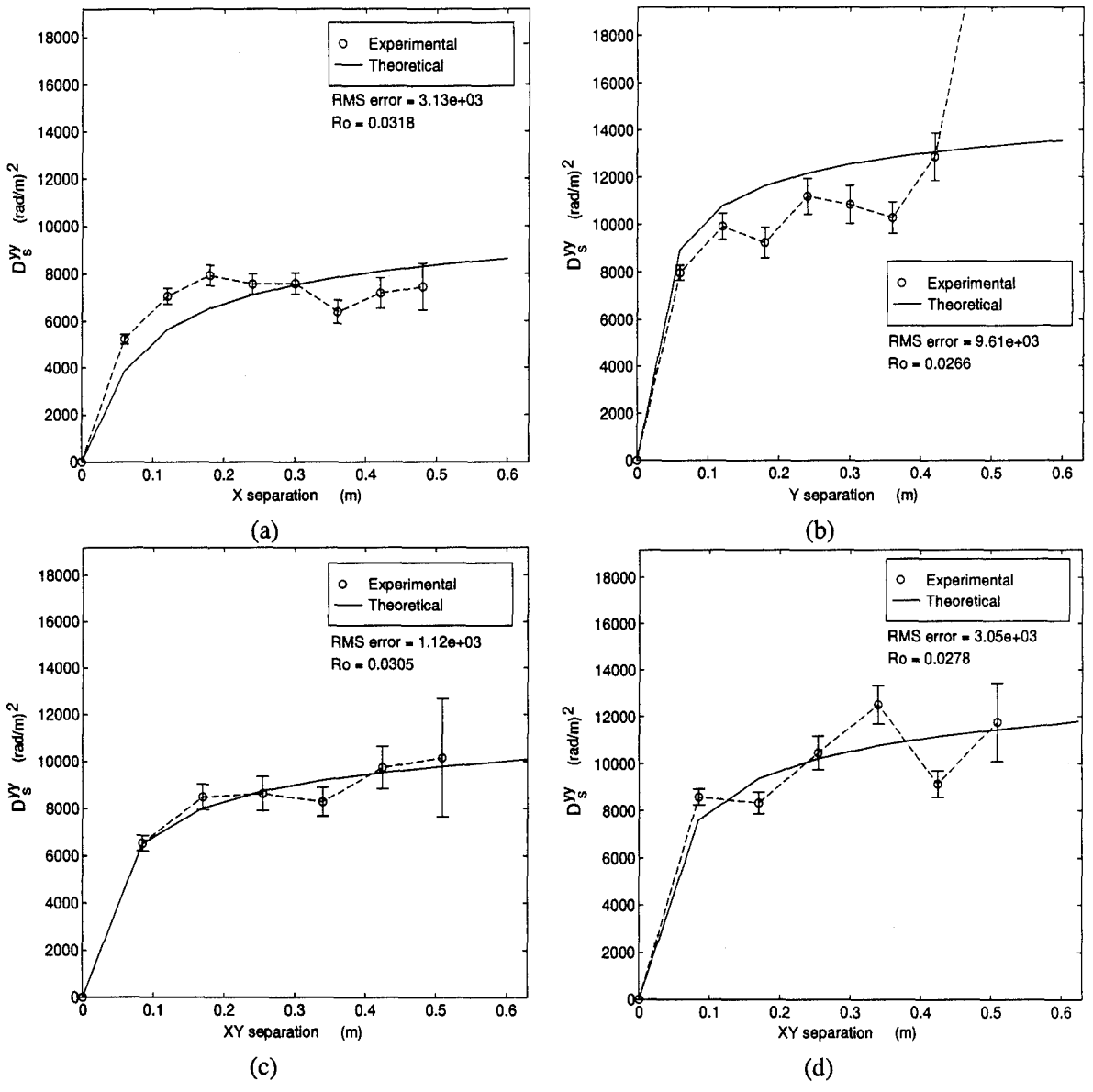

Figure 4.9 Structure function isotropy: spatially averaged D_s^{yy} for (a) x, (b) y, (c) $+45°$, and (d) $-45°$ separations. Average slopes not removed.

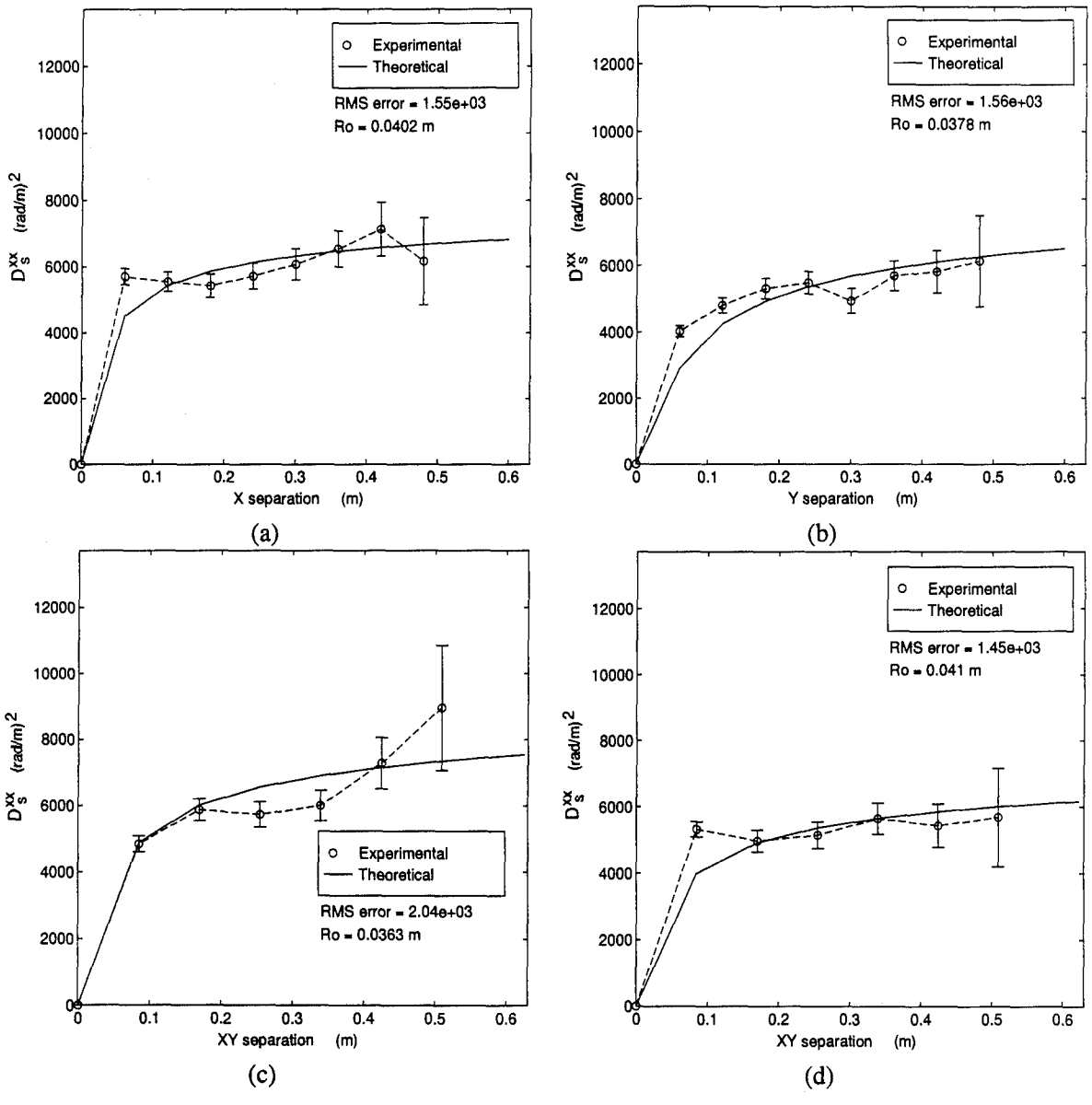

Figure 4.10 Structure function isotropy: spatially averaged D_s^{xx} for (a) x, (b) y, (c) $+45°$, and (d) $-45°$ separations. Average slopes removed.

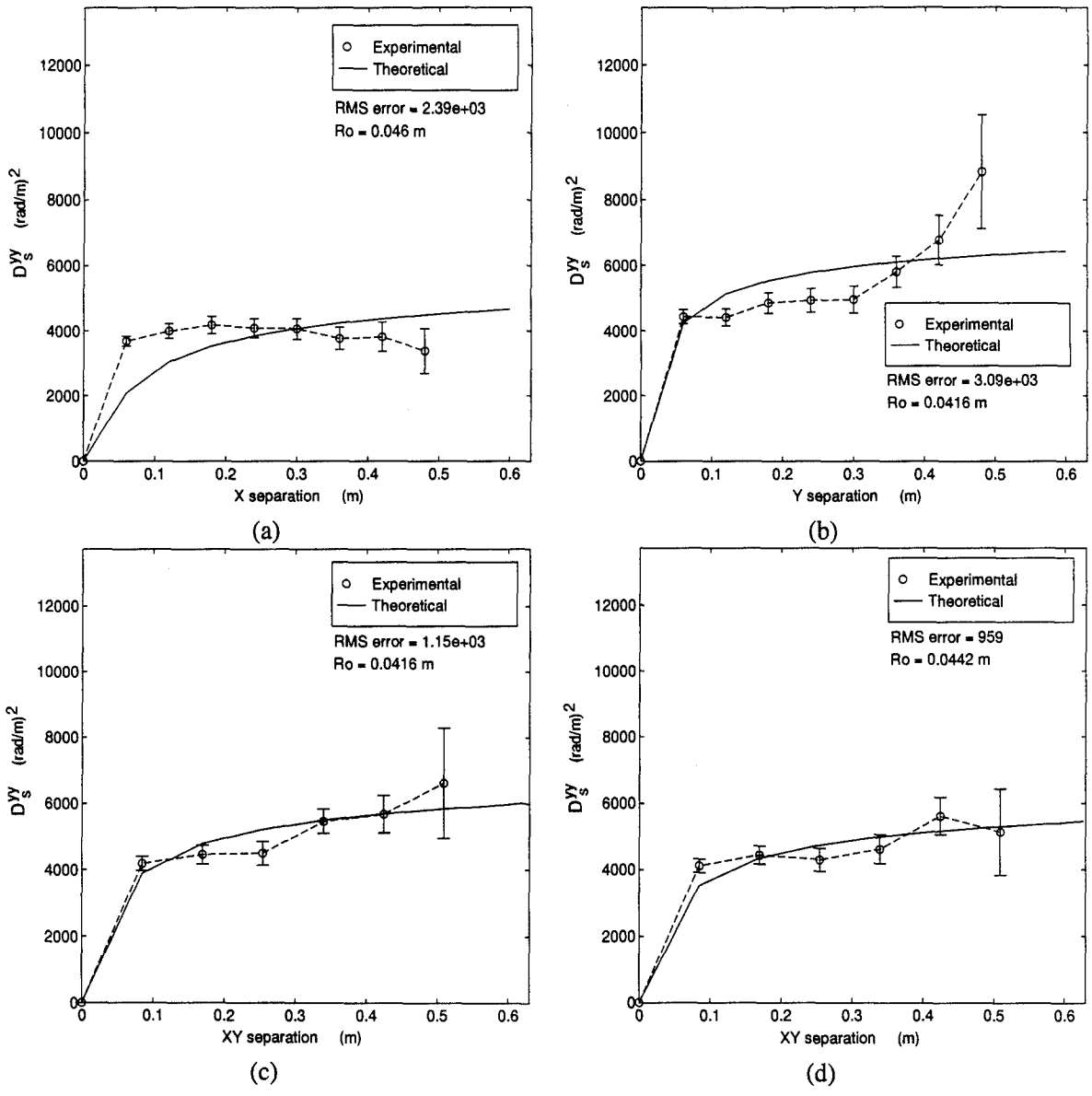

Figure 4.11 Structure function isotropy: spatially averaged D_s^{yy} for (a) x, (b) y, (c) $+45°$, and (d) $-45°$ separations. Average slopes removed.

Slopes	Direction	Data Sets				
		Yokota3-1	Science3	Yokota3-2	Osan2	Science2
x	x	0.045	0.040	0.041	0.037	0.037
	y	0.044	0.038	0.039	0.038	0.042
	$+45°$	0.044	0.036	0.040	0.039	0.040
	$-45°$	0.045	0.042	0.040	0.040	0.040
y	x	0.045	0.046	0.034	0.040	0.045
	y	0.044	0.042	0.040	0.044	0.039
	$+45°$	0.045	0.042	0.040	0.044	0.038
	$-45°$	0.047	0.044	0.041	0.042	0.042

Table 4.2 Recovered r_o values (in meters) for average slope removed structure functions.

As expected, the confidence intervals for the estimated structure functions are markedly reduced. This is due to the increase in the effective ensemble size from the spatial averaging. Overall, the structure functions have the functional forms predicted by theory. The RMS errors for the average slope removed structure functions are in general lower than the non-average removed structure functions. However, there are some exceptions. Average removal had much greater success with data sets such as *Osan2* which had much larger average slopes than the *Science3* data set.

Recovered r_o values for all the data sets are shown in Table 4.2. The measurements for the data sets were collected at various geographical locations and path lengths. The recovered r_o values are remarkably constant over the various path lengths. There seems to be a slight, possibly illusory, decrease in the average r_o values as the path lengths increase. However, such a trend is highly dependent on the actual strength of the turbulence encountered along a given path. Another unknown is the effect of boundary layer turbulence on the optical beam. Such an effect should be fairly constant since the aircraft velocity was kept constant during data collection. Any effects of boundary layer turbulence should reduce the r_o value.

4.3 Summary

Five ABLE ACE H-WFS data sets were analyzed using the slope structure function estimator and compared to theory. Tests for homogeneity and isotropy of the turbulence encountered suggest, but do not prove, that the turbulence was homogeneous and isotropic. Knowing if the turbulence has these properties is critical since these are fundamental assumptions made by theoretical models of

atmospheric turbulence. The behavior of the estimated slope structure functions follows that of the theoretical slope structure functions derived using the Kolmogorov model for atmospheric turbulence.

V. Conclusions and Recommendations

In this chapter the major results and conclusions from this thesis are highlighted. Recommendations for extending the concepts and methods used in this thesis in future work are also presented.

5.1 Results and conclusions

The theoretical results presented in Chapter II provide expressions for the tilt-removed slope structure functions for the in terms of the phase structure function. This derivation assumes only homogeneity, isotropy, and zero mean characteristics of the wavefront phase. Thus, the large body of theoretical work for the phase structure function is available for use. There are many different formulations for the phase structure function which can be used ranging from the simple Kolmogorv model to the von Karman model to the general power law model developed by Stribling [21].

The self slope structure function has been evaluated for the Kolmogorov turbulence model using numerical quadrature. The symmetry inherent in the H-WFS geometry allowed the integrations to be reduced to single dimensional integrals from the original four-fold integrations and normalized. This normalization dramatically reduced the computations necessary to evaluate the integrals.

In Chapter III a method for estimating the slope structure function, without assuming homogeneity and isotropy, was presented. This estimator allows us to check any assumptions about the homogeneity and isotropy of our data. Using simulated slope measurements known to have Kolmogorov turbulence statistics shows that the estimator can recover the slope structure function. Deterministic aberrations were shown to have a large effect on the estimator's performance. Average slope removal was shown to be effective in removing aberrations similar to those found in several of the ABLE ACE data sets. The r_o values were also recovered to within two significant figures.

Many thousands of ABEL ACE WFS image frames were processed to find the several hundred frames which make up the ensembles analyzed in Chapter IV. Due to the limited ensemble length the results shown in the tests for homogeneity are not conclusive. Combining the structure function results and the slope variance calculations suggests that the turbulence encountered probably is homogeneous.

The spatially averaged structure functions tended to follow the behavior expected based on the theoretical slope structure functions. Of course, spatial averaging is only valid if the turbulence truly is homogeneous. The significance of the results from the ABLE ACE data sets is difficult to determine

since the effects of the boundary layer turbulence on the slope measurements cannot be separated from the atmospheric turbulence effects. Recovered r_o values for all path lengths were approximately 0.04 meters.

One of the advantages of using the H-WFS slope measurements directly are that the computationally intense step of phase reconstruction is bypassed. Also, any noise enhancement and assumptions about the turbulence characteristics are also avoided. One of the limitations of this method is that it can only sense the perturbations of orders higher than the overall tilt. Unfortunately, the overall tilt of the wave front phase contains 90% of the energy in the perturbations [7]. This lack of sensitivity can be an advantage if the overall tilt cannot be trusted. This technique should be useful for real-time turbulence sensing.

5.2 Suggestions for further work

Some extensions and further work which would be useful are:

- Evaluate the theoretical slope structure functions for the von Karman and generalized power laws. These evaluations would provide information on how the slope structure function behavior changes with different turbulence statistics.
- Evaluate the behavior of the structure function estimator with noisy slope measurements. Knowing how sensitive this estimator is to noise would be useful in assessing the reliability of results.
- Apply these methods to other data sets or more of the ABLE ACE data. The ABEL ACE data was collected under challenging conditions and contained several unknown sources of noise or distortion. The measurements recently collected by researchers at AFIT over a long, horizontal path between mountain tops in Hawaii would be another good data set.
- Determining the effects of boundary layer turbulence on the optical beam would be beneficial. Such an analysis would help determine how much of the wave front phase distortions are due to boundary layer versus atmospheric turbulence.

Characterizing atmospheric turbulence using H-WFS slope measurements directly is feasible. The calculations involved are much less computationally intense than the traditional phase reconstruction methods. The self slope structure function is insensitive to overall tilt and cannot be sensed by this

method. Recovering r_o values in real-time is a possibility. Such r_o values could be used to adaptively optimize the performance of optical systems. Overall, another tool is available in our tool box for characterizing atmospheric turbulence.

Appendix A. ABLE ACE data analysis

The *Science3* data set was displayed in Chapter IV in full. This appendix displays the analysis for the remaining ABLE ACE data sets. The global average and variances for the x and y slopes are displayed first. Next plots showing the homogeneity of the average removed x and y slopes are displayed. Last, plots showing the isotropy and fit to theory are displayed.

A.1 Osan2 analysis

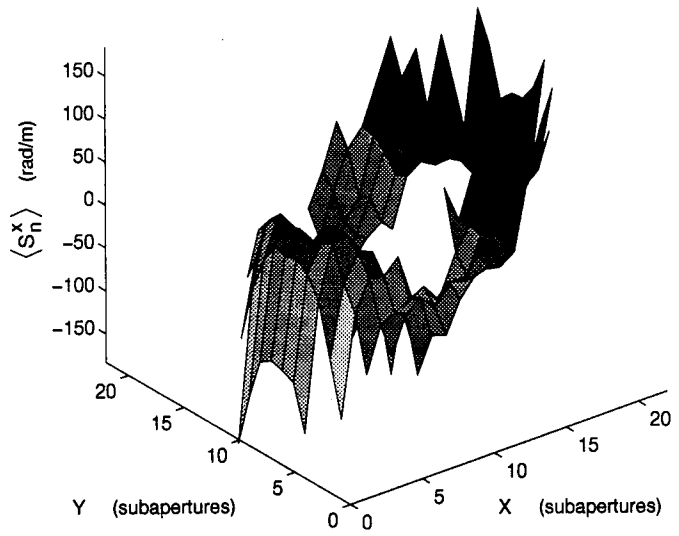

(a)

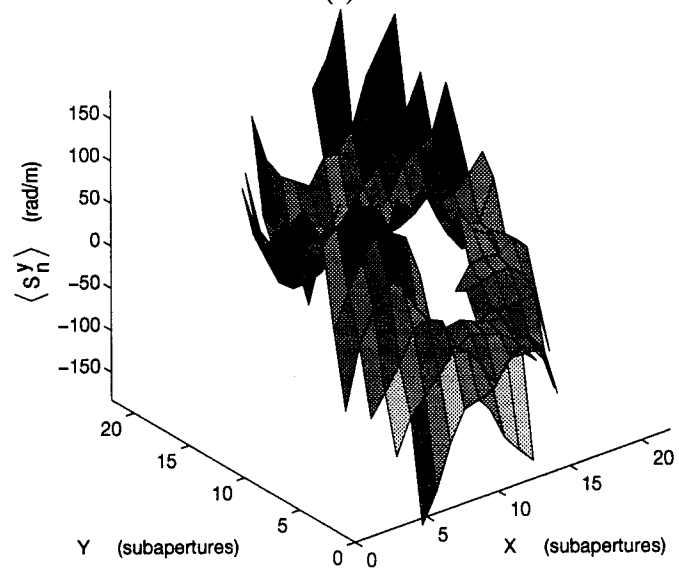

(b)

Figure A.1 Osan2: (a) x-slope average, $\langle s_n^x \rangle$, and (b) y-slope average, $\langle s_n^y \rangle$.

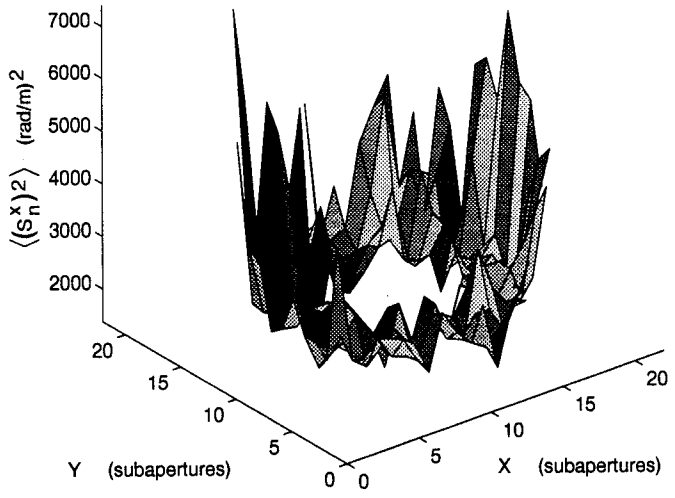

(a)

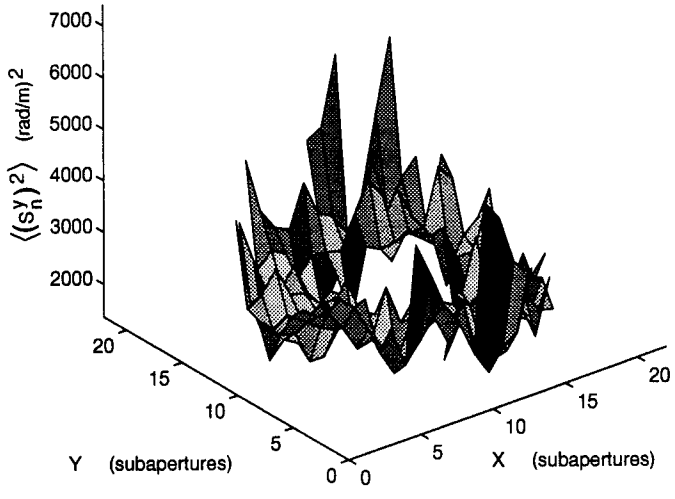

(b)

Figure A.2 Osan2: (a) x-slope variance, $\langle (s_n^x)^2 \rangle$, and (b) y-slope variance, $\langle (s_n^y)^2 \rangle$

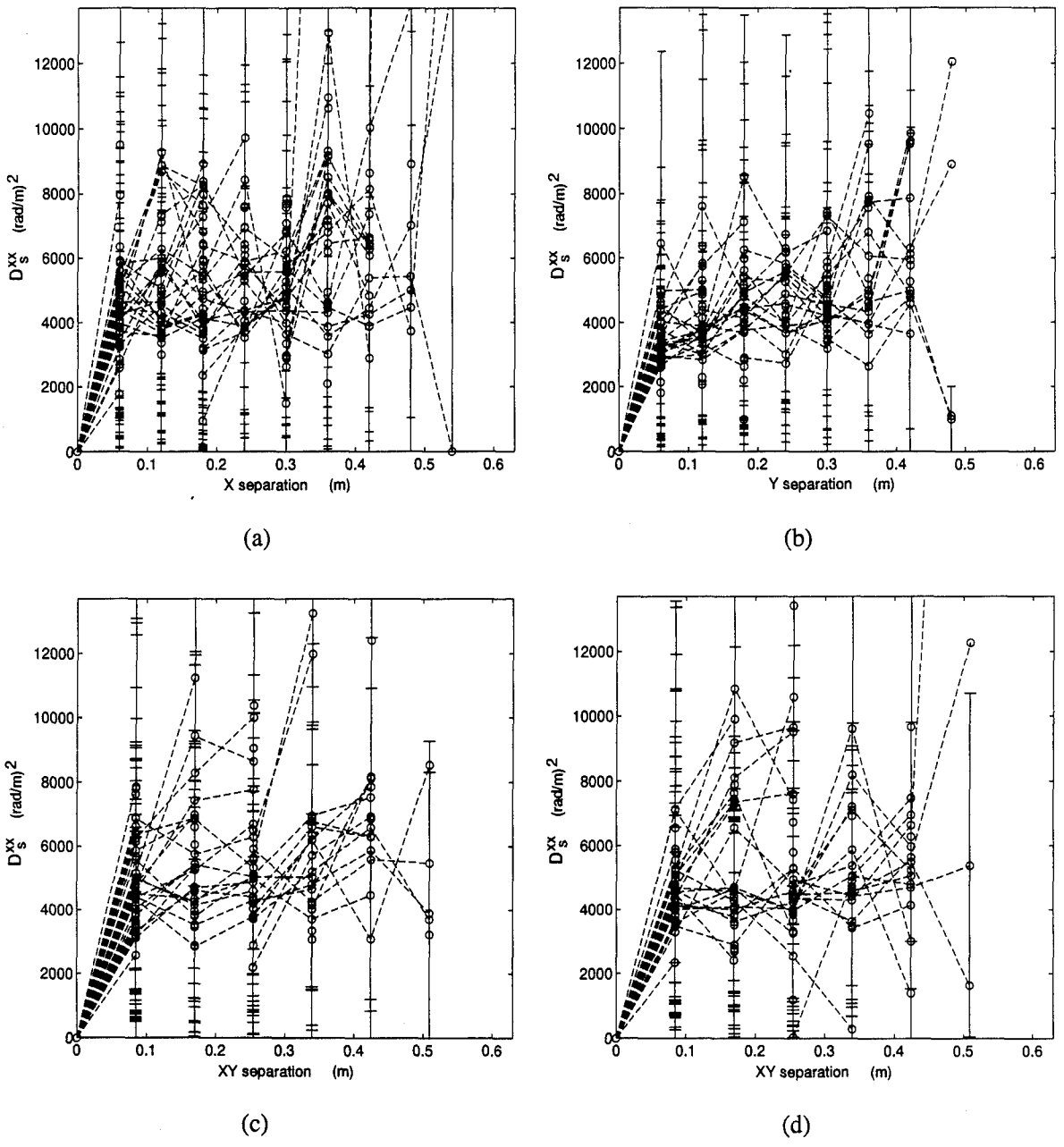

Figure A.3 Structure function homogeneity: D_s^{xx}-slopes shifted in for (a) x, (b) y, (c) $+45°$, and (d) $-45°$ separations. Average slopes removed.

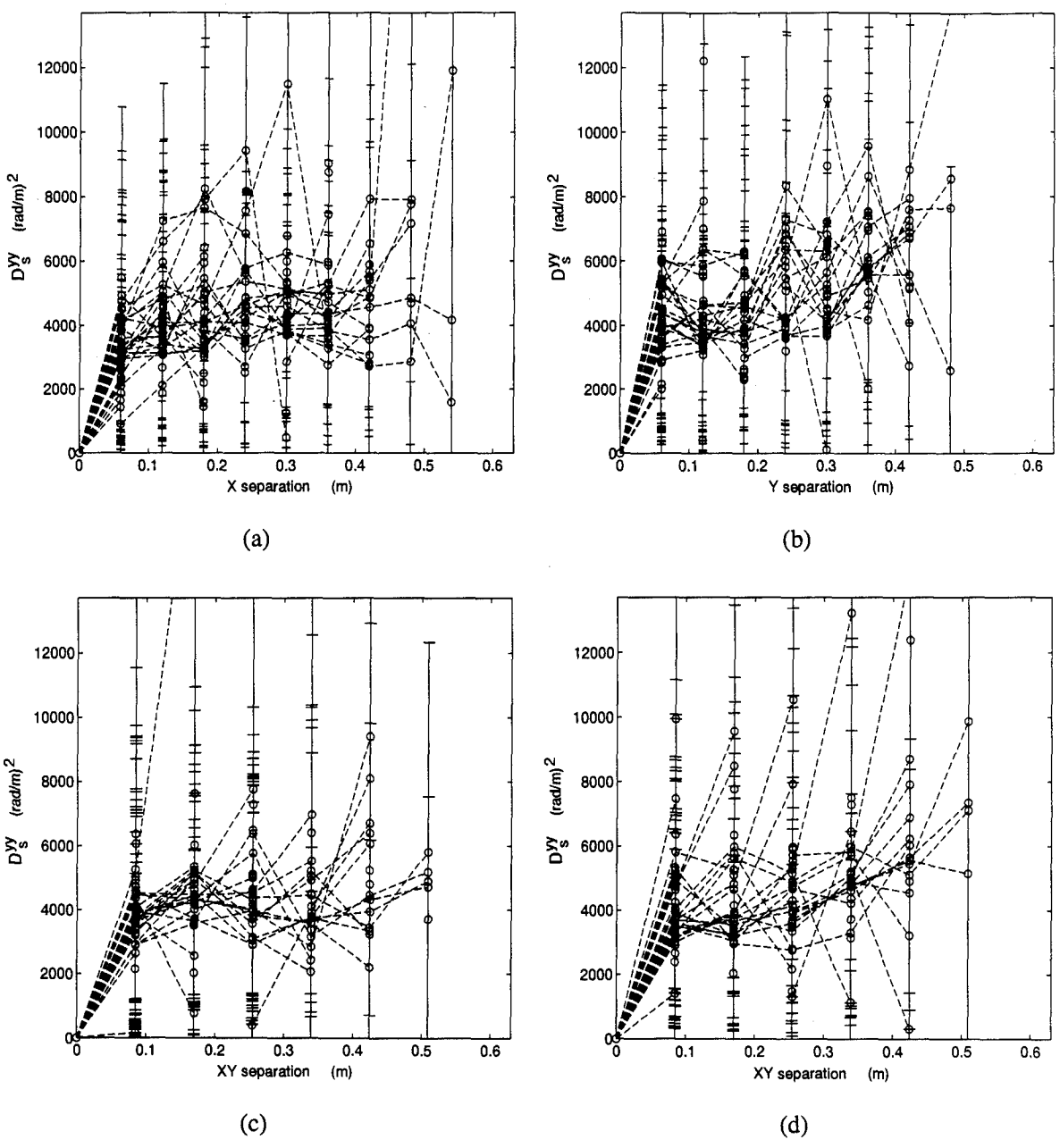

Figure A.4 Structure function homogeneity: D_s^{yy} for (a) x, (b) y, (c) $+45°$, and (d) $-45°$ separations. Average slopes removed.

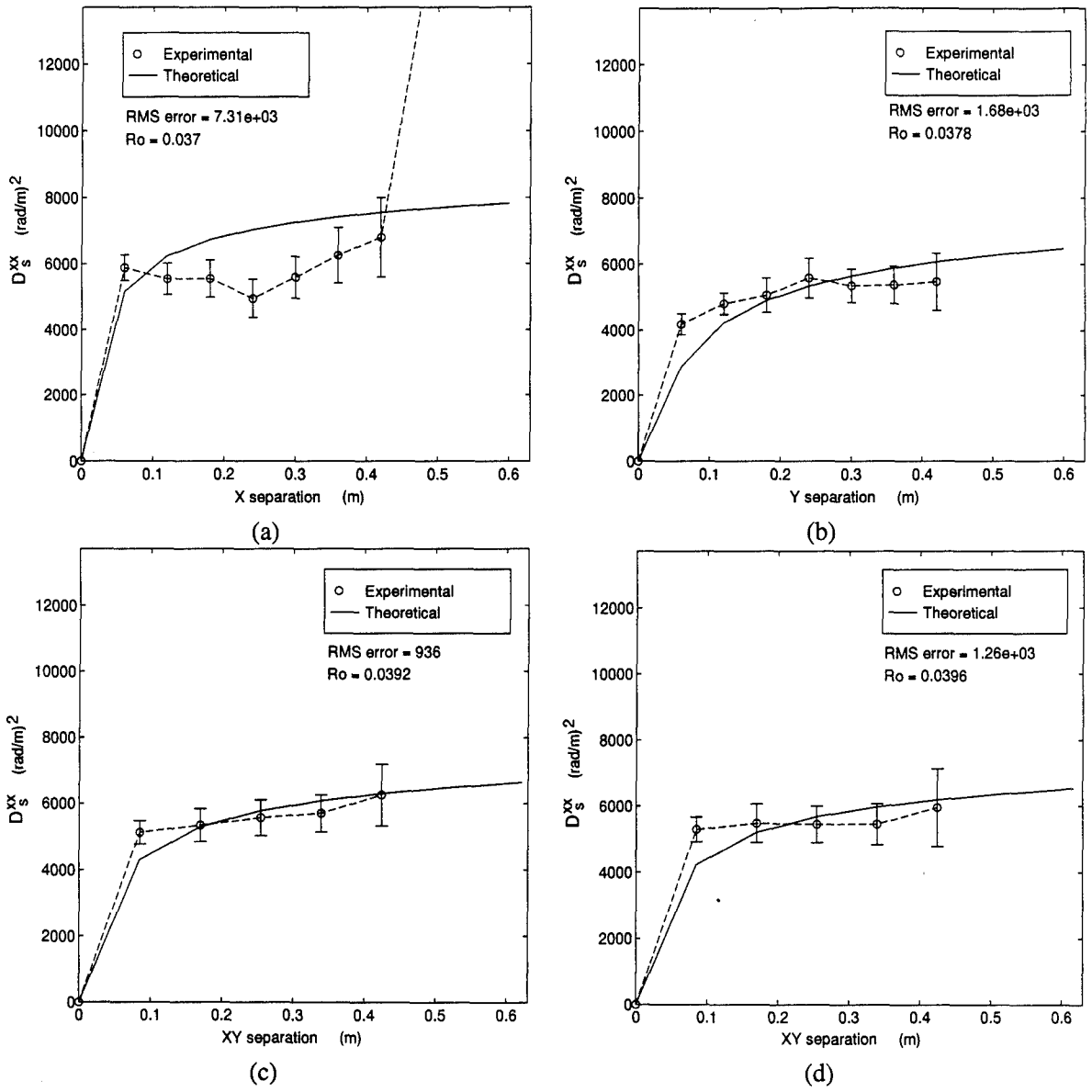

Figure A.5 Structure function isotropy: spatially averaged D_s^{xx} for (a) x, (b) y, (c) $+45°$, and (d) $-45°$ separations. Average slopes removed.

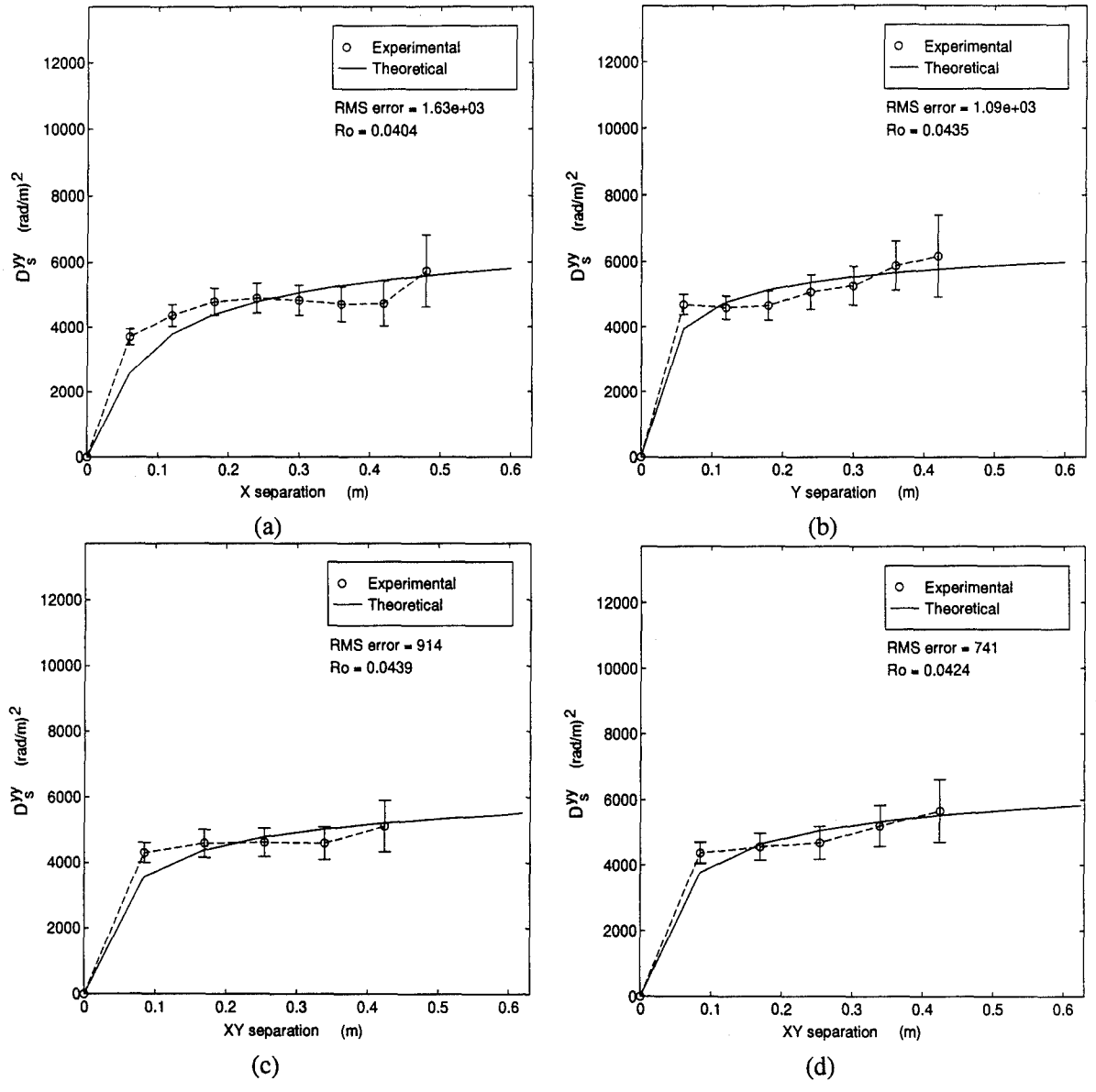

Figure A.6 Structure functionn isotropy: spatially averaged D_s^{yy} for (a) x, (b) y, (c) $+45°$, and (d) $-45°$ separations. Average slopes removed.

A.2 Science2 analysis

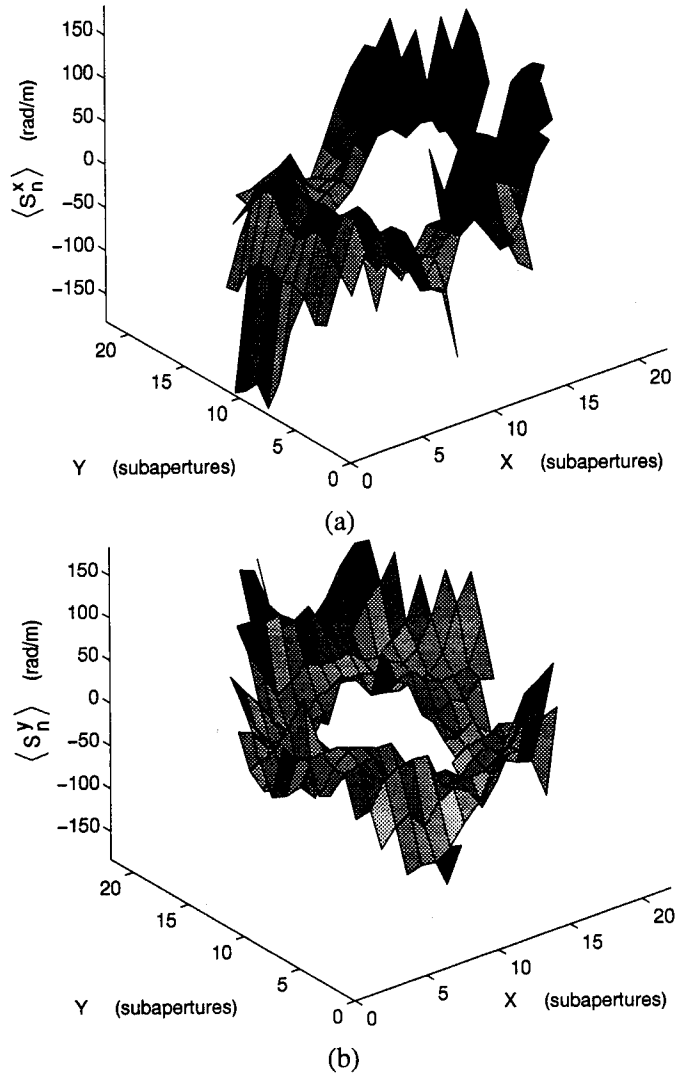

Figure A.7 Science2: (a) x-slope average, $\langle s_n^x \rangle$, and (b) y-slope average, $\langle s_n^y \rangle$.

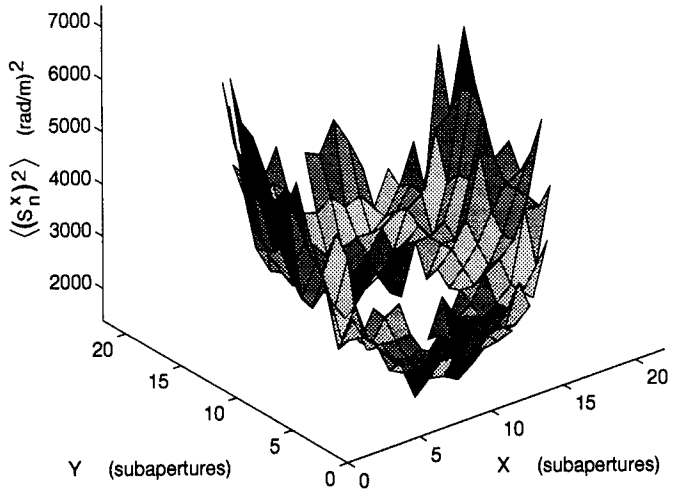

(a)

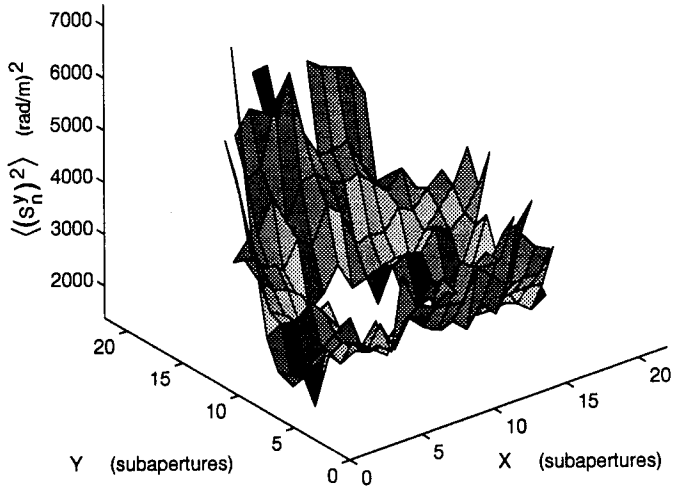

(b)

Figure A.8 Science2: (a) x-slope variance, $\langle (s_n^x)^2 \rangle$, and (b) y-slope variance, $\langle (s_n^y)^2 \rangle$

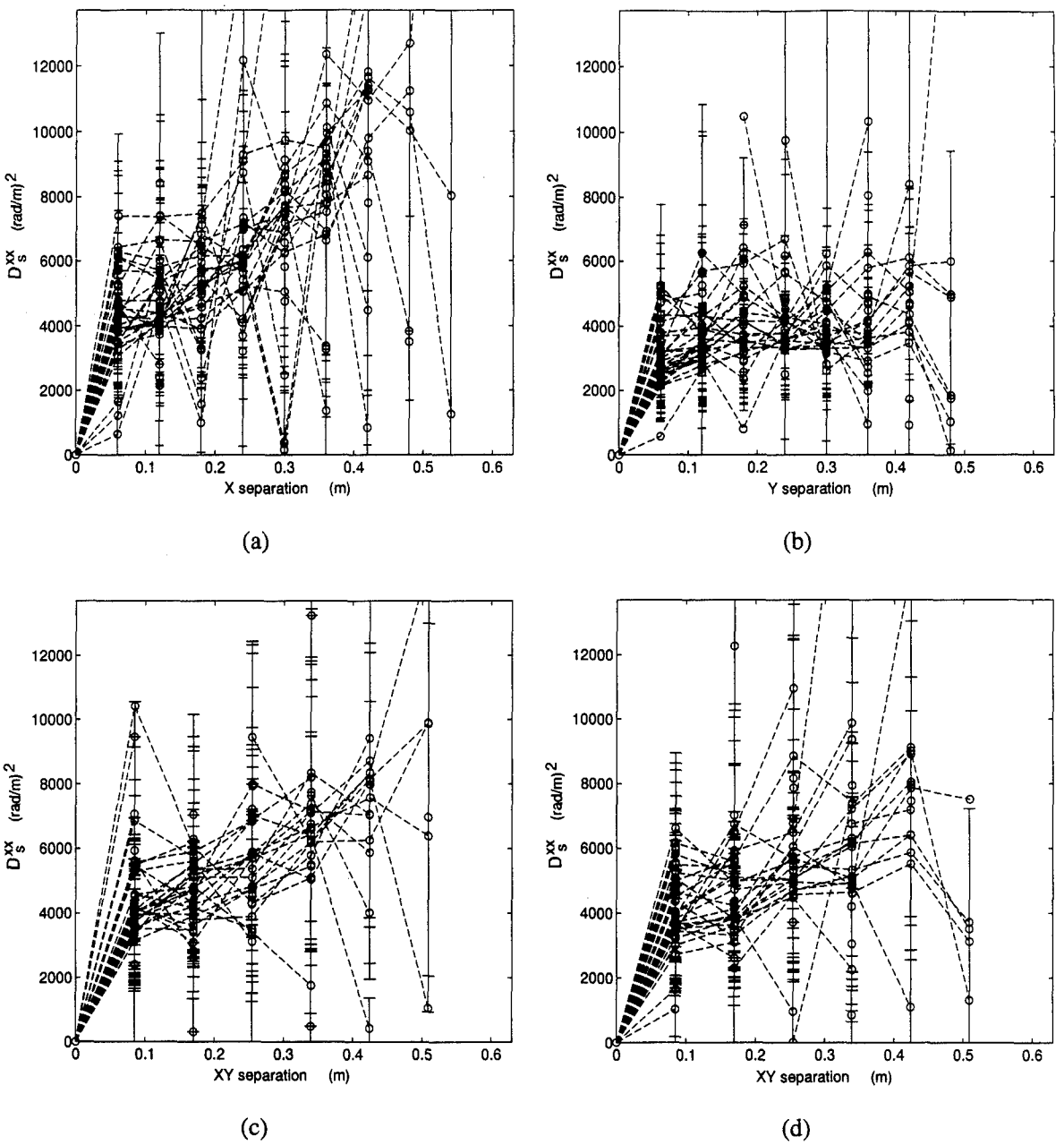

Figure A.9 Structure function homogeneity: D_s^{xx}-slopes shifted in for (a) x, (b) y, (c) $+45°$, and (d) $-45°$ separations. Average slopes removed.

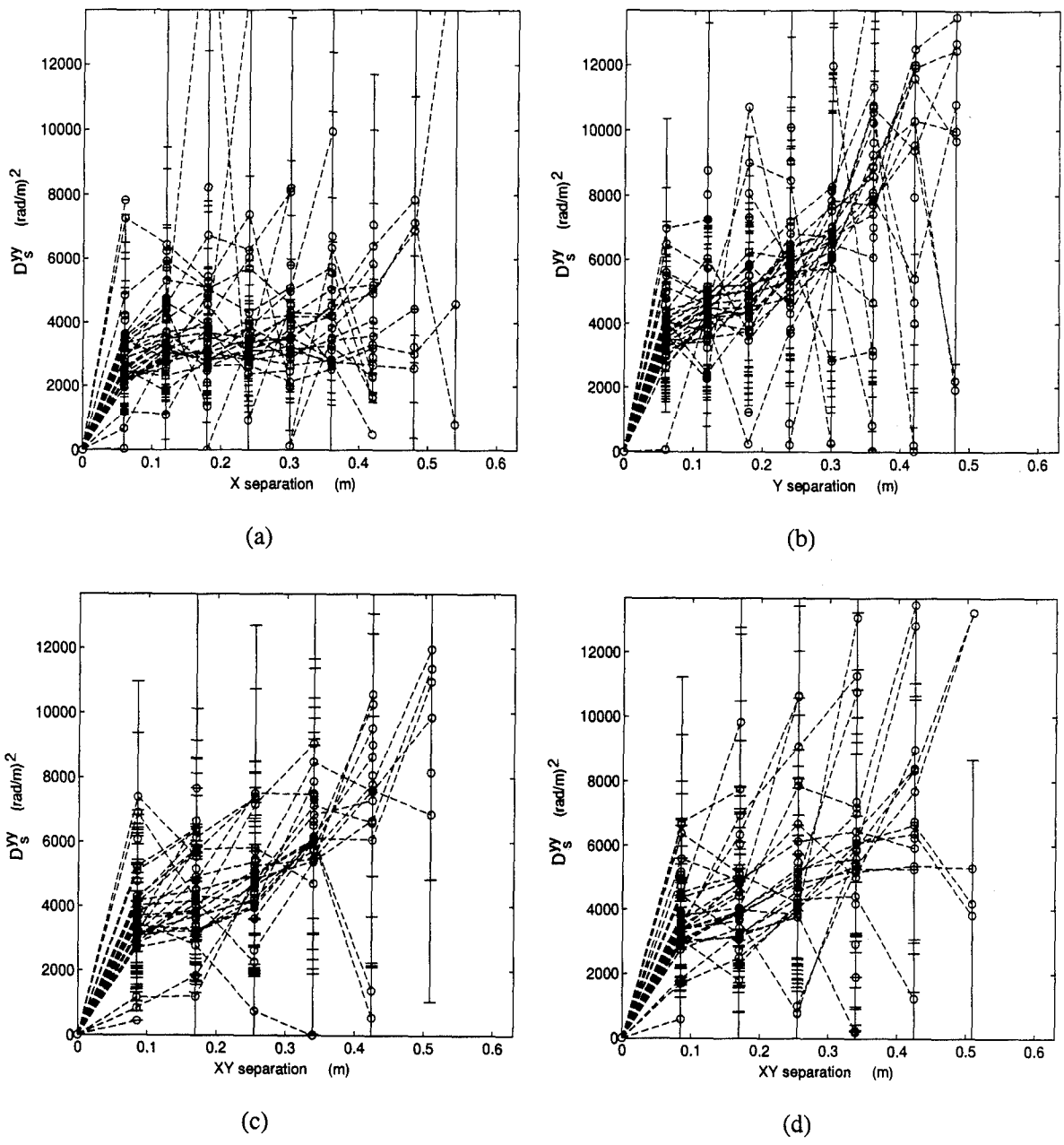

Figure A.10 Structure function homogeneity: D_s^{yy} for (a) x, (b) y, (c) $+45°$, and (d) $-45°$ separations. Average slopes removed.

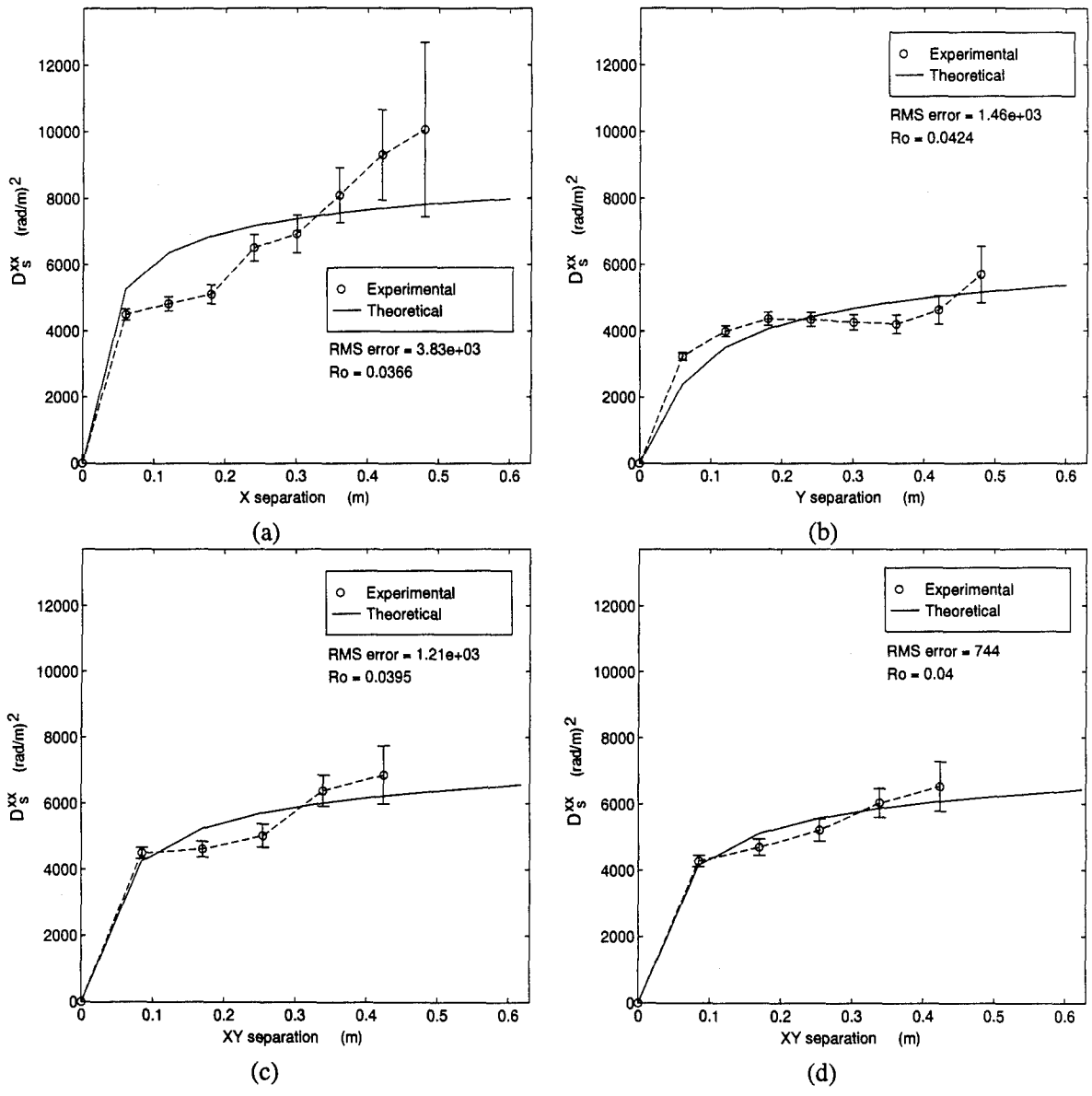

Figure A.11 Structure function isotropy: spatially averaged D_s^{xx} for (a) x, (b) y, (c) $+45°$, and (d) $-45°$ separations. Average slopes removed.

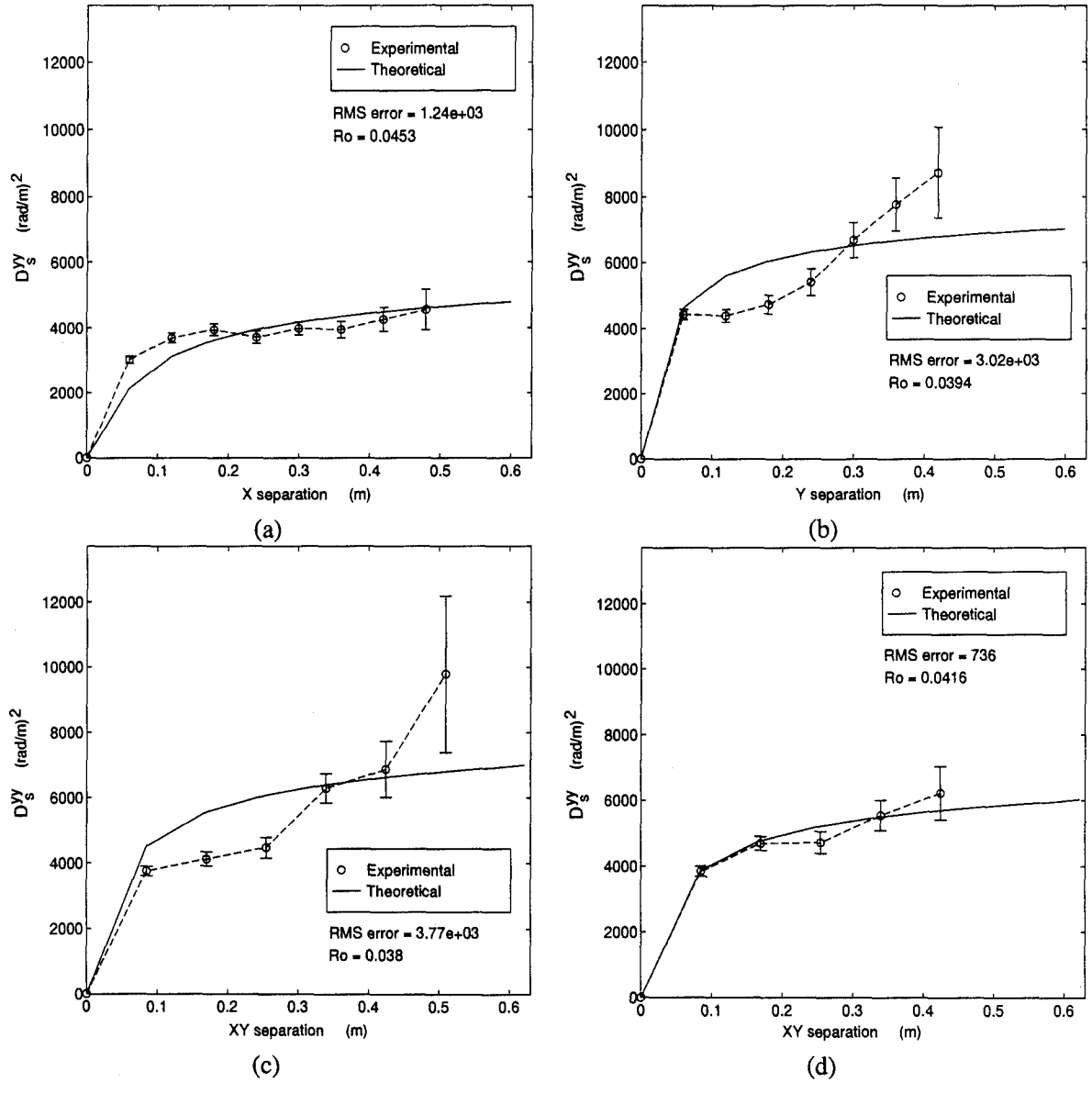

Figure A.12 Structure functionn isotropy: spatially averaged D_s^{yy} for (a) x, (b) y, (c) $+45°$, and (d) $-45°$ separations. Average slopes removed.

A.3 Yokota3-1 data analysis

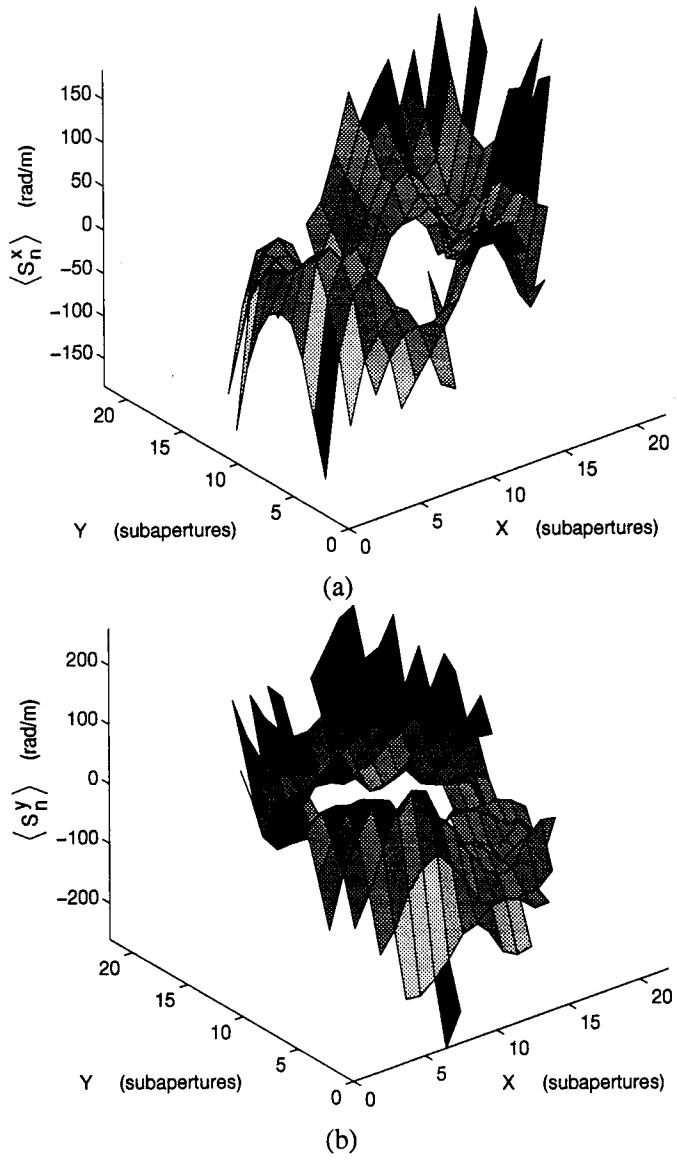

Figure A.13 Yokota3: (a) x-slope average, $\langle s_n^x \rangle$, and (b) y-slope average, $\langle s_n^y \rangle$.

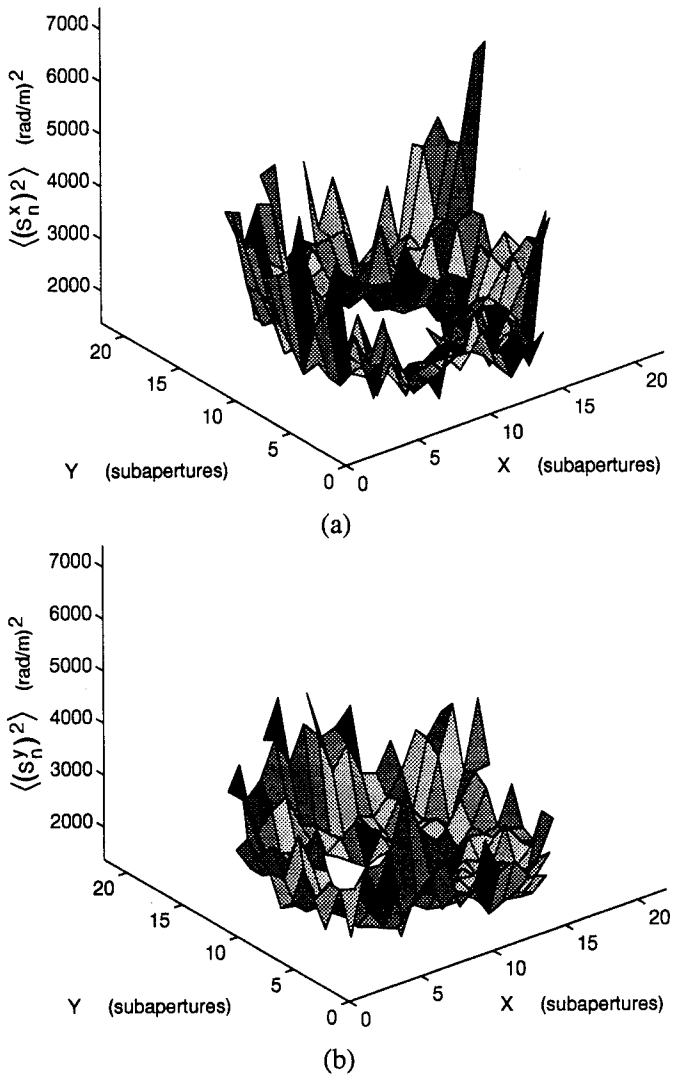

Figure A.14 Yokota3: (a) x-slope variance, $\langle (s_n^x)^2 \rangle$, and (b) y-slope variance, $\langle (s_n^y)^2 \rangle$

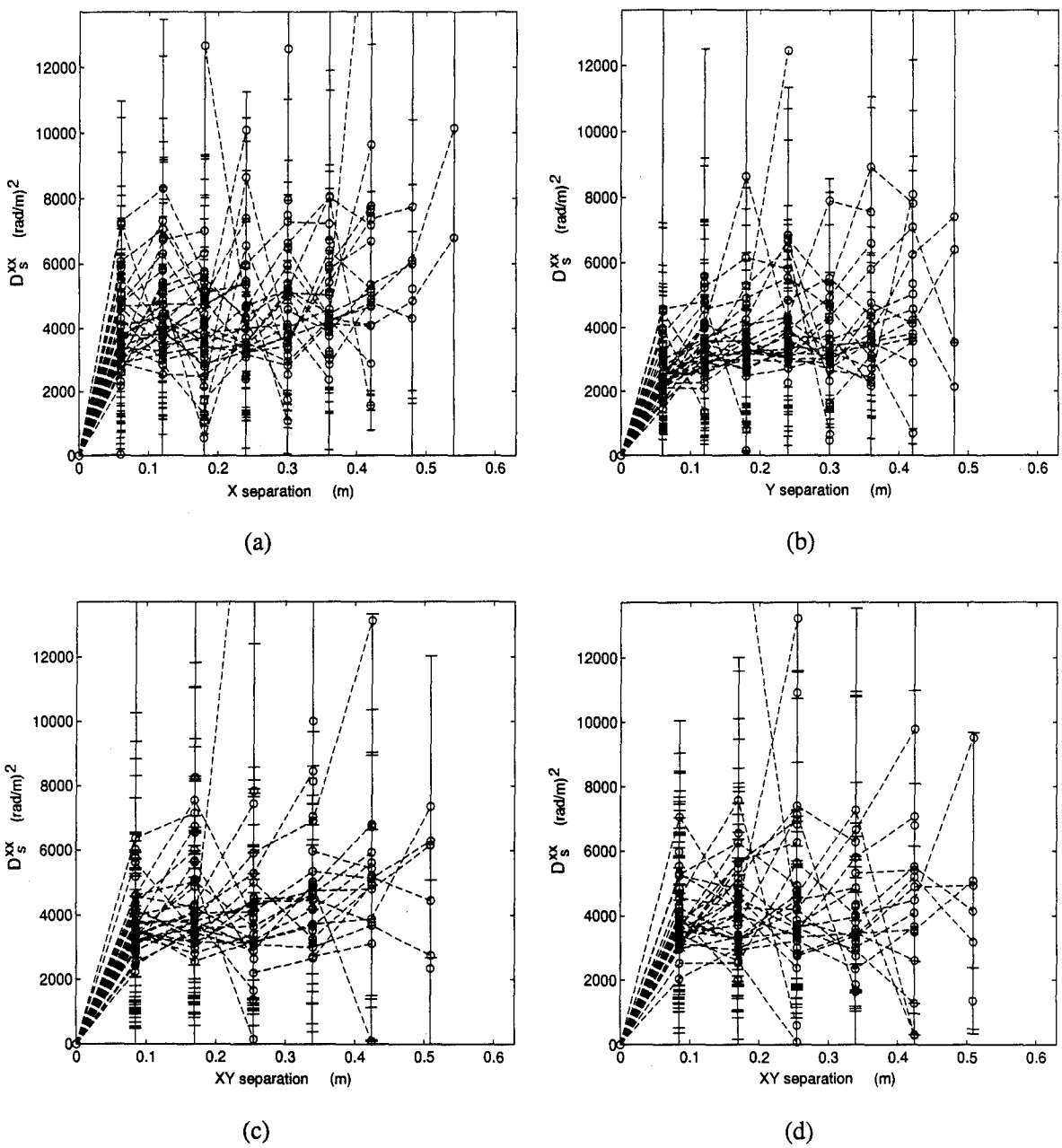

Figure A.15 Structure function homogeneity: D_s^{xx}-slopes shifted in for (a) x, (b) y, (c) $+45°$, and (d) $-45°$ separations. Average slopes removed.

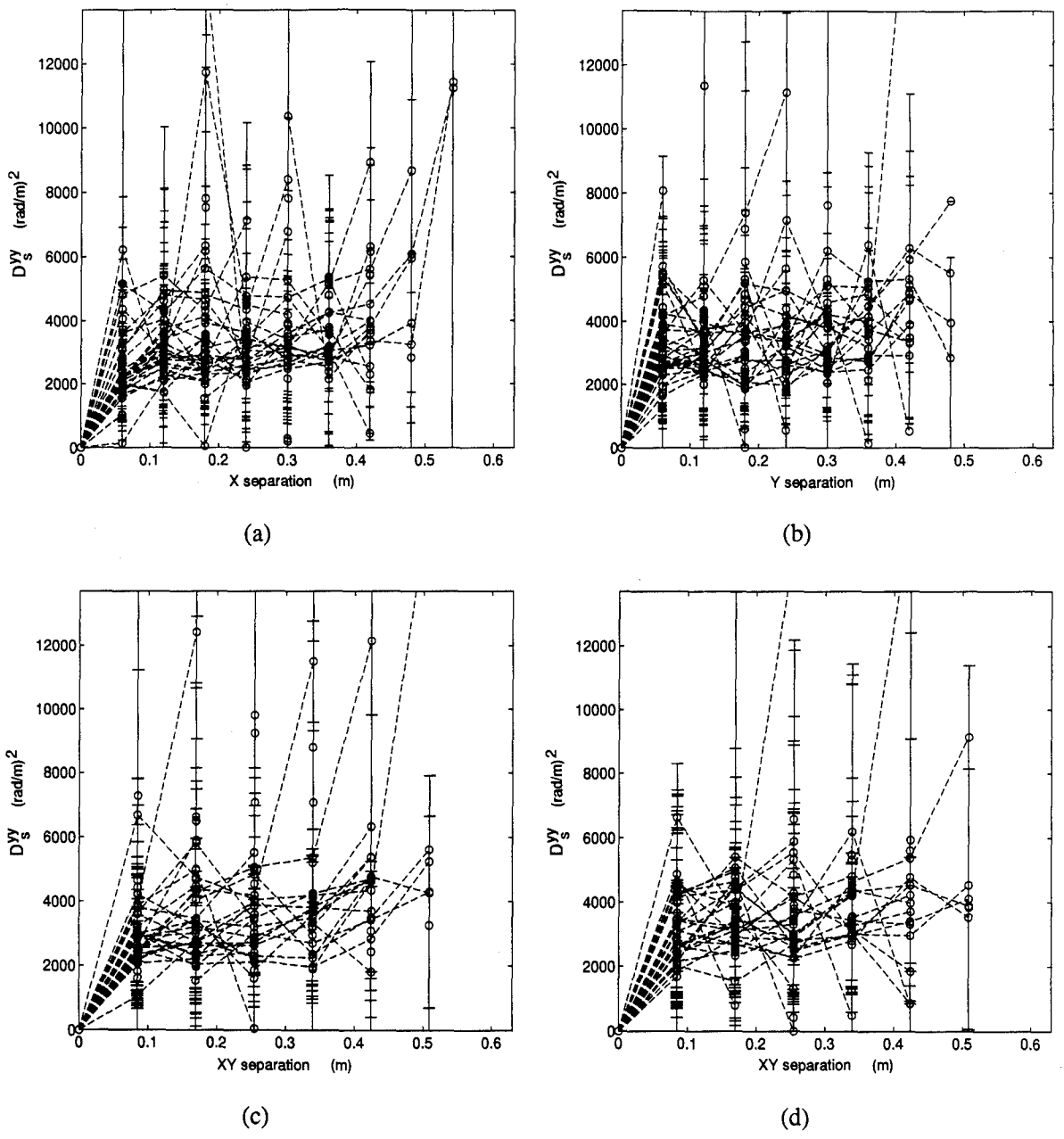

Figure A.16 Structure function homogeneity: D_s^{yy} for (a) x, (b) y, (c) $+45°$, and (d) $-45°$ separations. Average slopes removed.

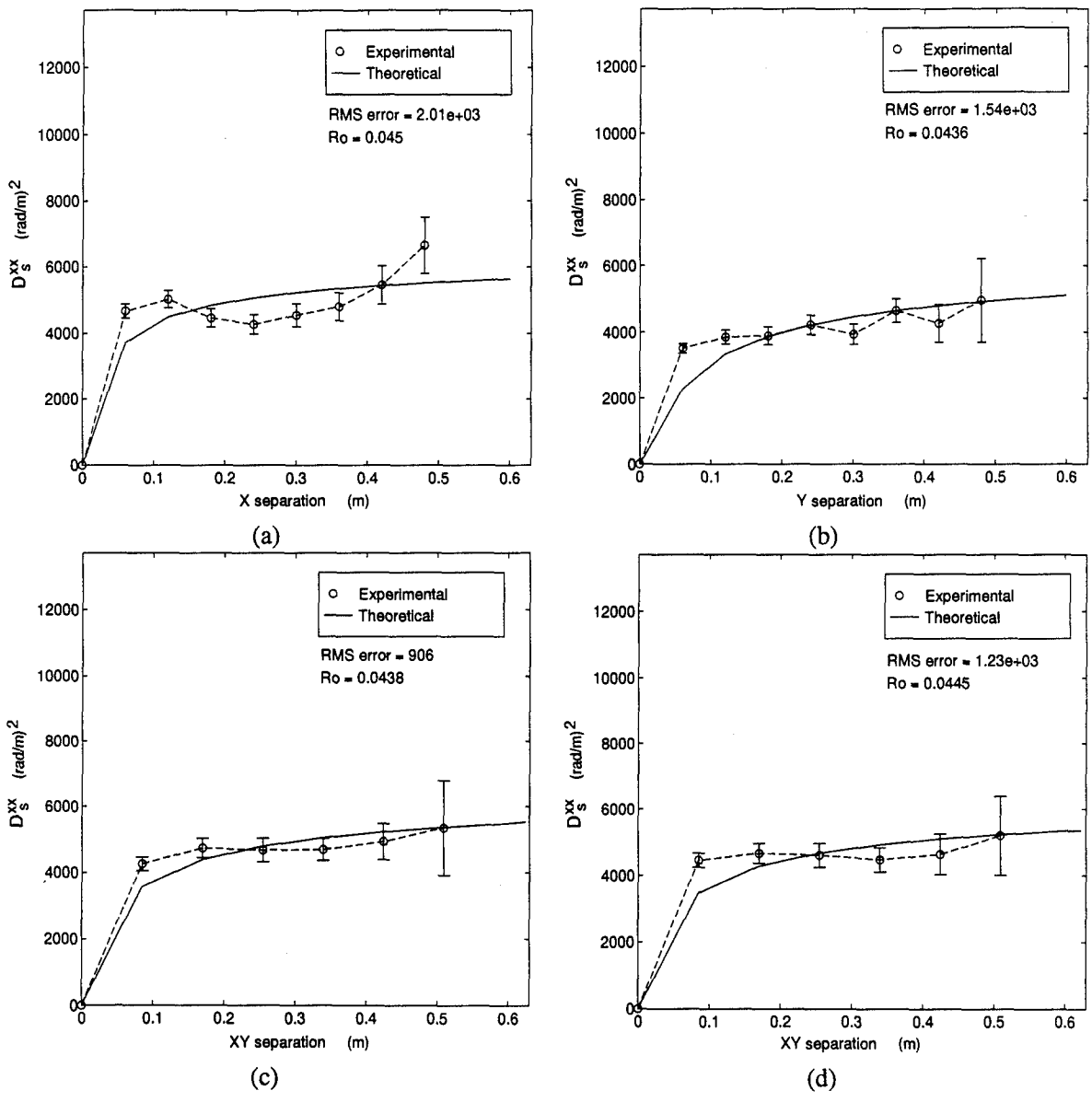

Figure A.17 Structure function isotropy: spatially averaged D_s^{xx} for (a) x, (b) y, (c) $+45°$, and (d) $-45°$ separations. Average slopes removed.

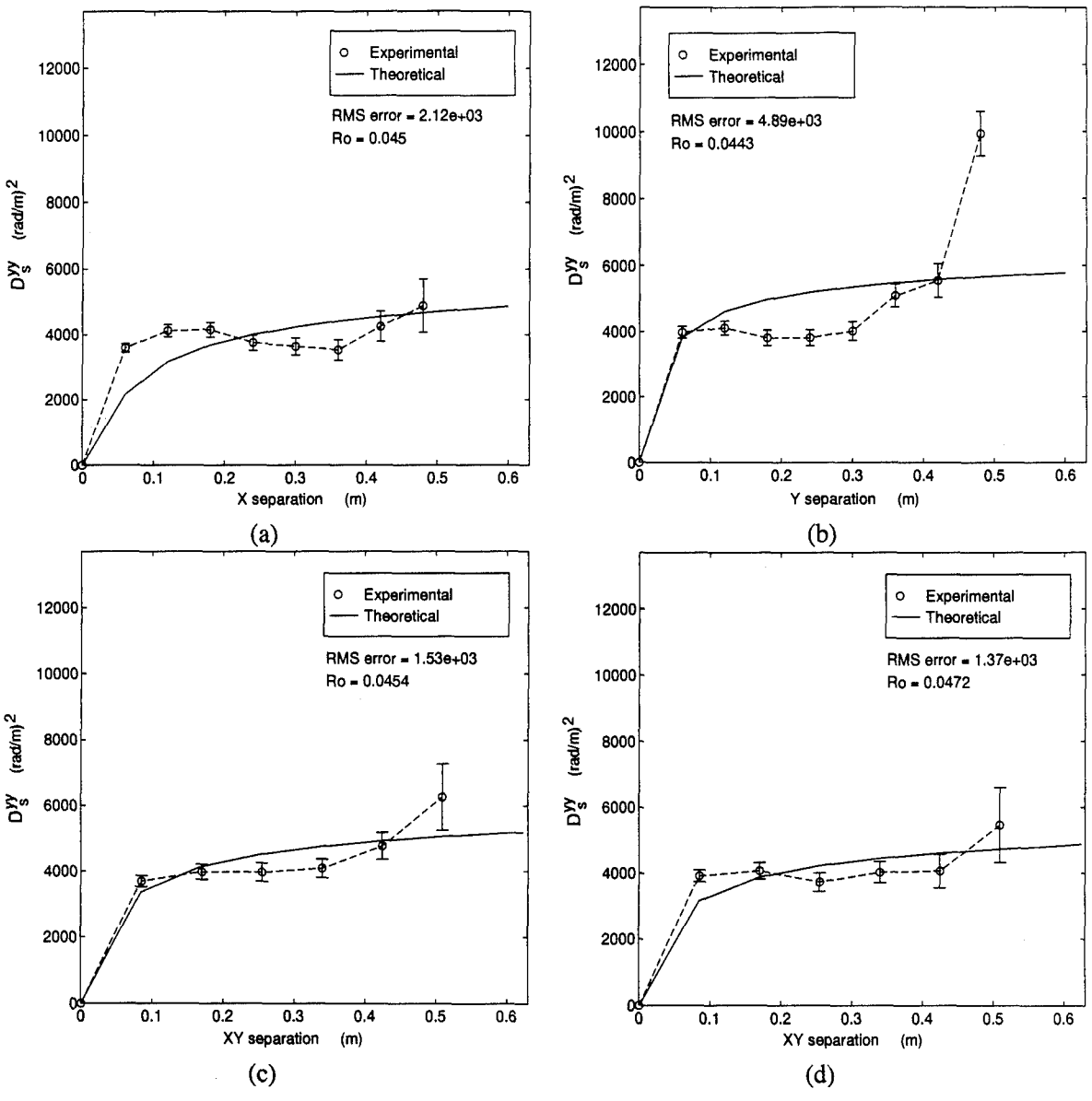

Figure A.18 Structure functionn isotropy: spatially averaged D_s^{yy} for (a) x, (b) y, (c) $+45°$, and (d) $-45°$ separations. Average slopes removed.

A.4 Yokota3-2 data analysis

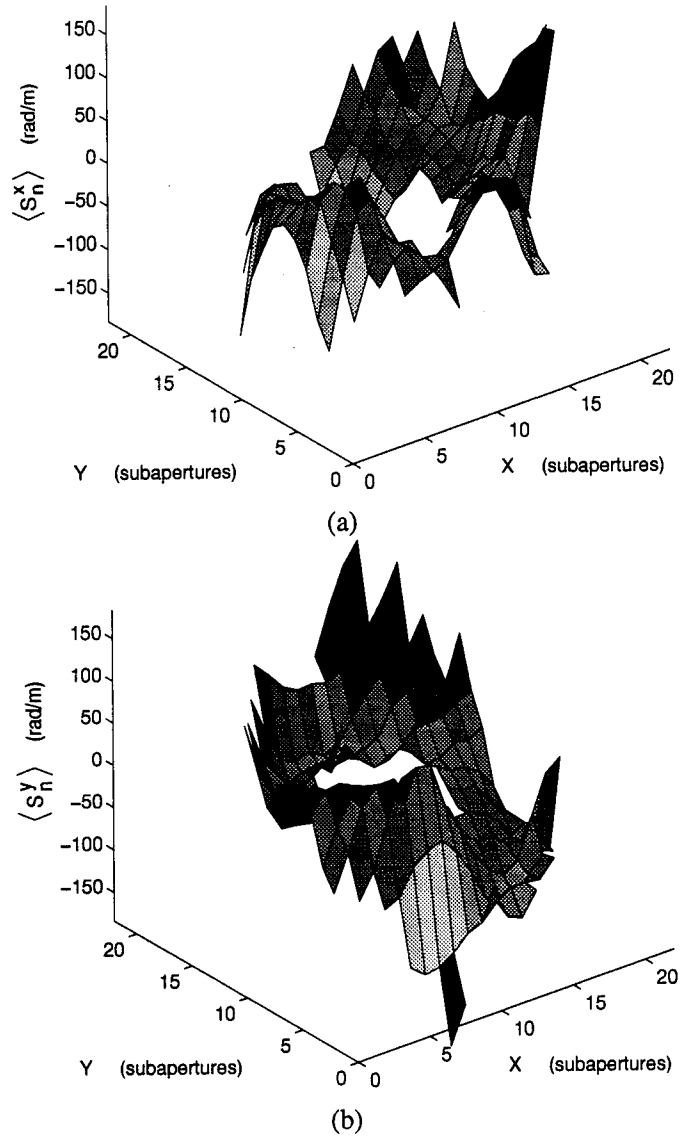

Figure A.19 Yokota3-2: (a) x-slope average, $\langle s_n^x \rangle$, and (b) y-slope average, $\langle s_n^y \rangle$.

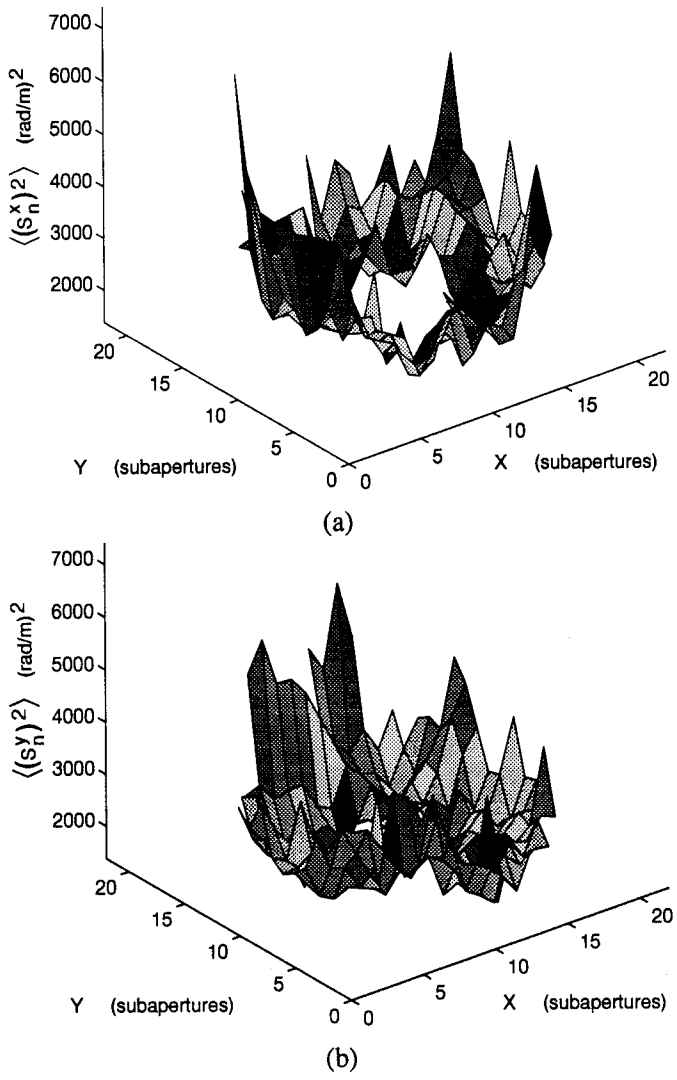

Figure A.20 Yokota3-2: (a) x-slope variance, $\langle(s_n^x)^2\rangle$, and (b) y-slope variance, $\langle(s_n^y)^2\rangle$

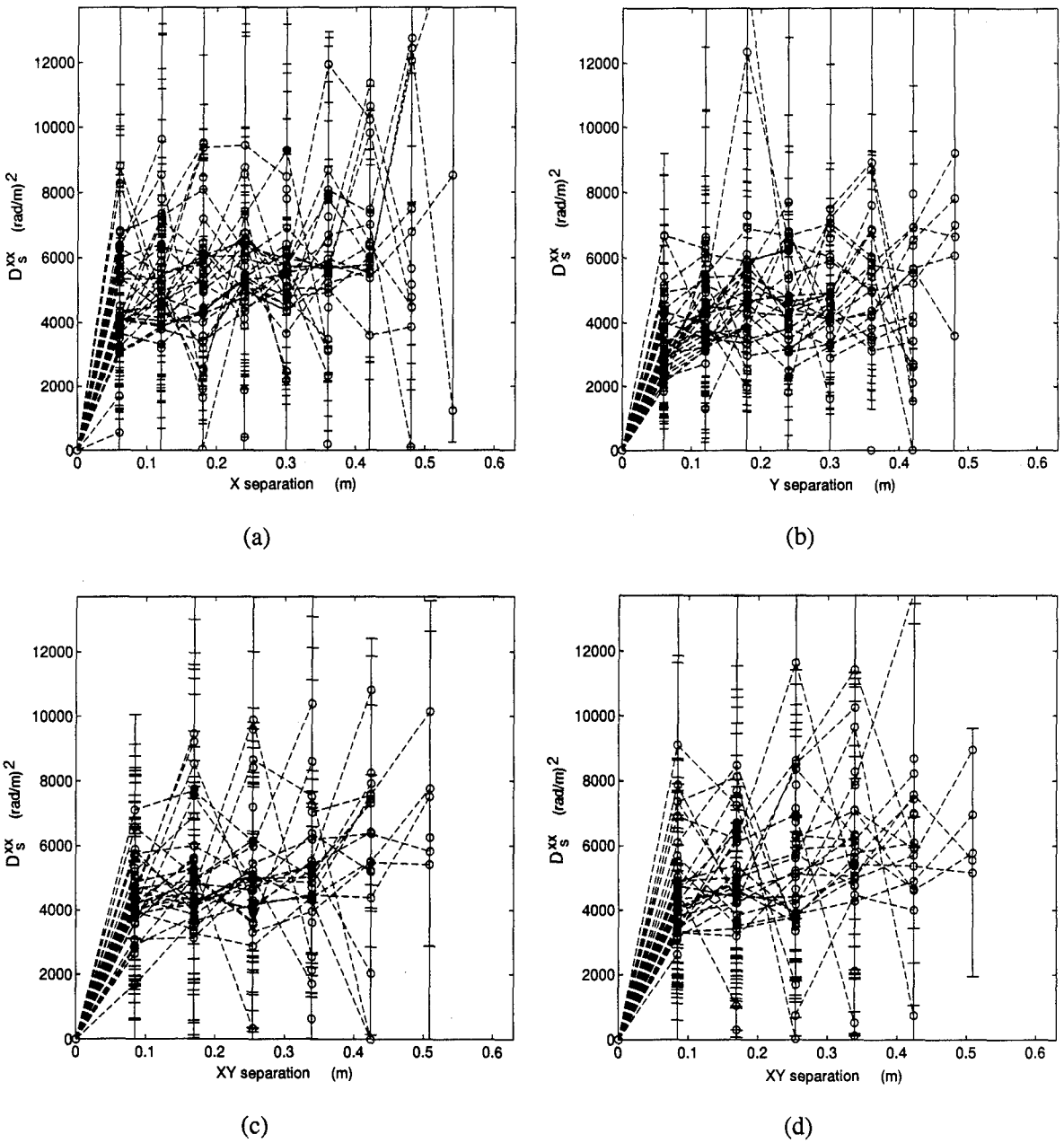

Figure A.21 Structure function homogeneity: D_s^{xx}-slopes shifted in for (a) x, (b) y, (c) $+45°$, and (d) $-45°$ separations. Average slopes removed.

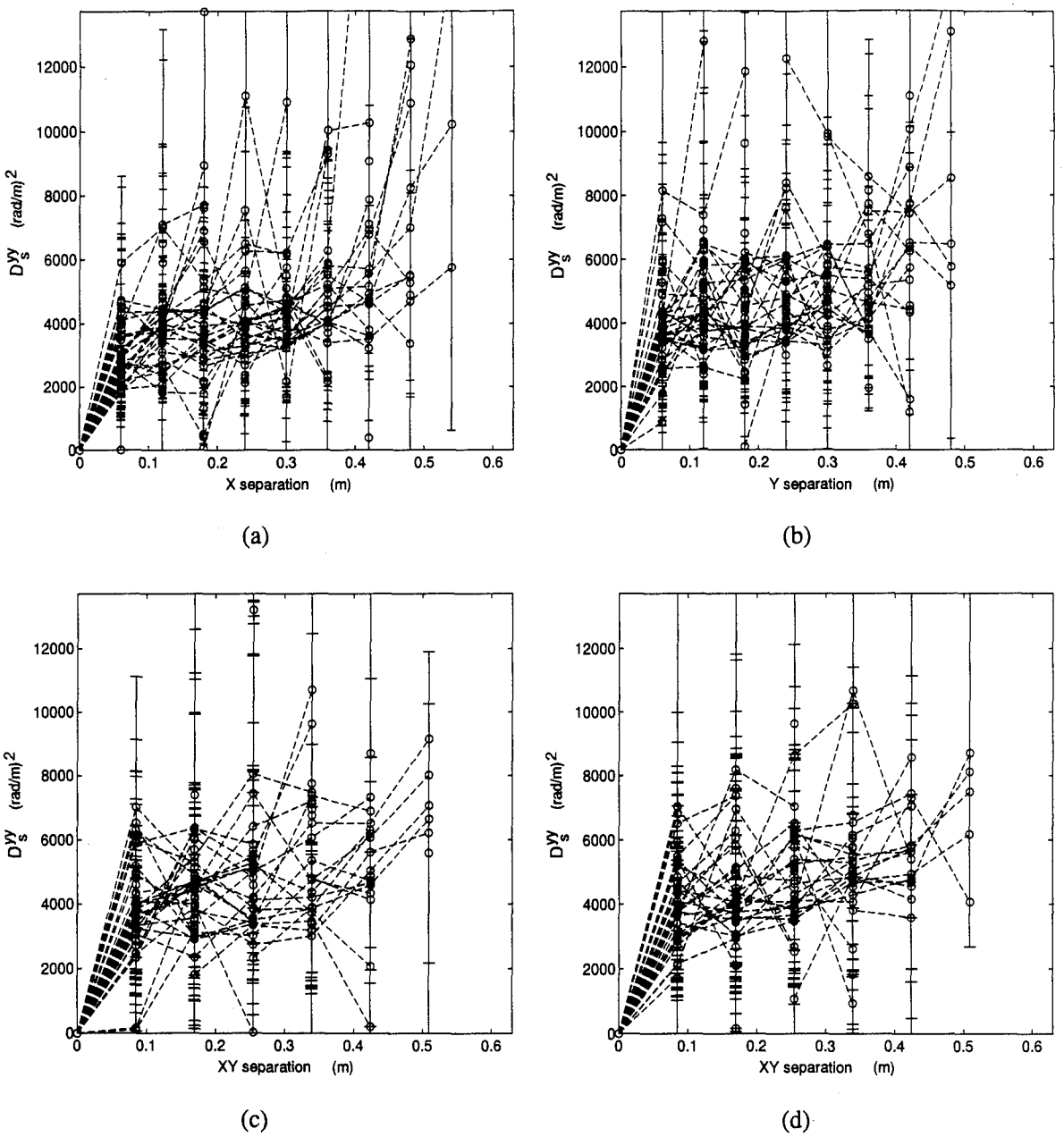

Figure A.22 Structure function homogeneity: D_s^{yy} for (a) x, (b) y, (c) $+45°$, and (d) $-45°$ separations. Average slopes removed.

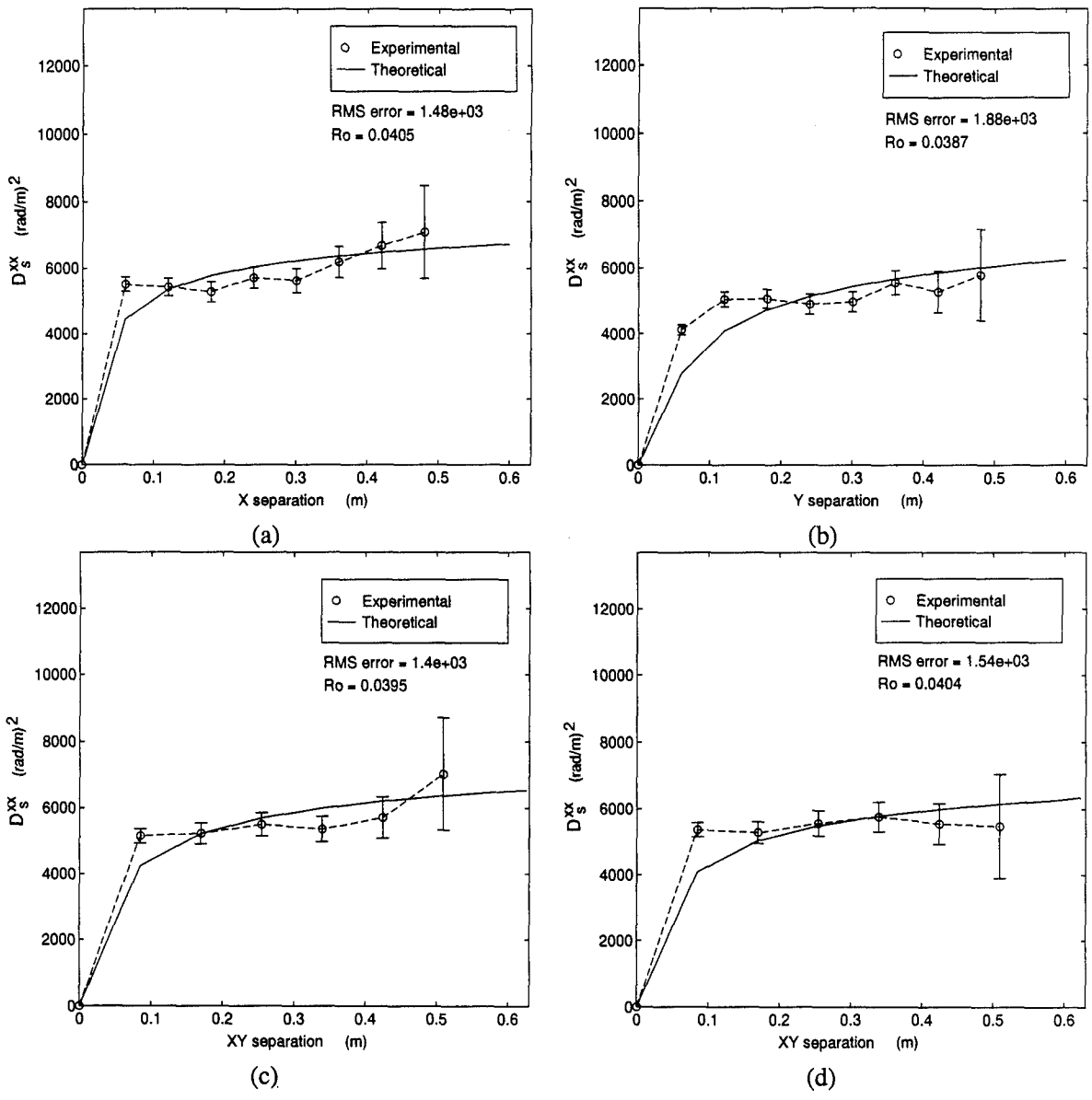

Figure A.23 Structure function isotropy: spatially averaged D_s^{xx} for (a) x, (b) y, (c) $+45°$, and (d) $-45°$ separations. Average slopes removed.

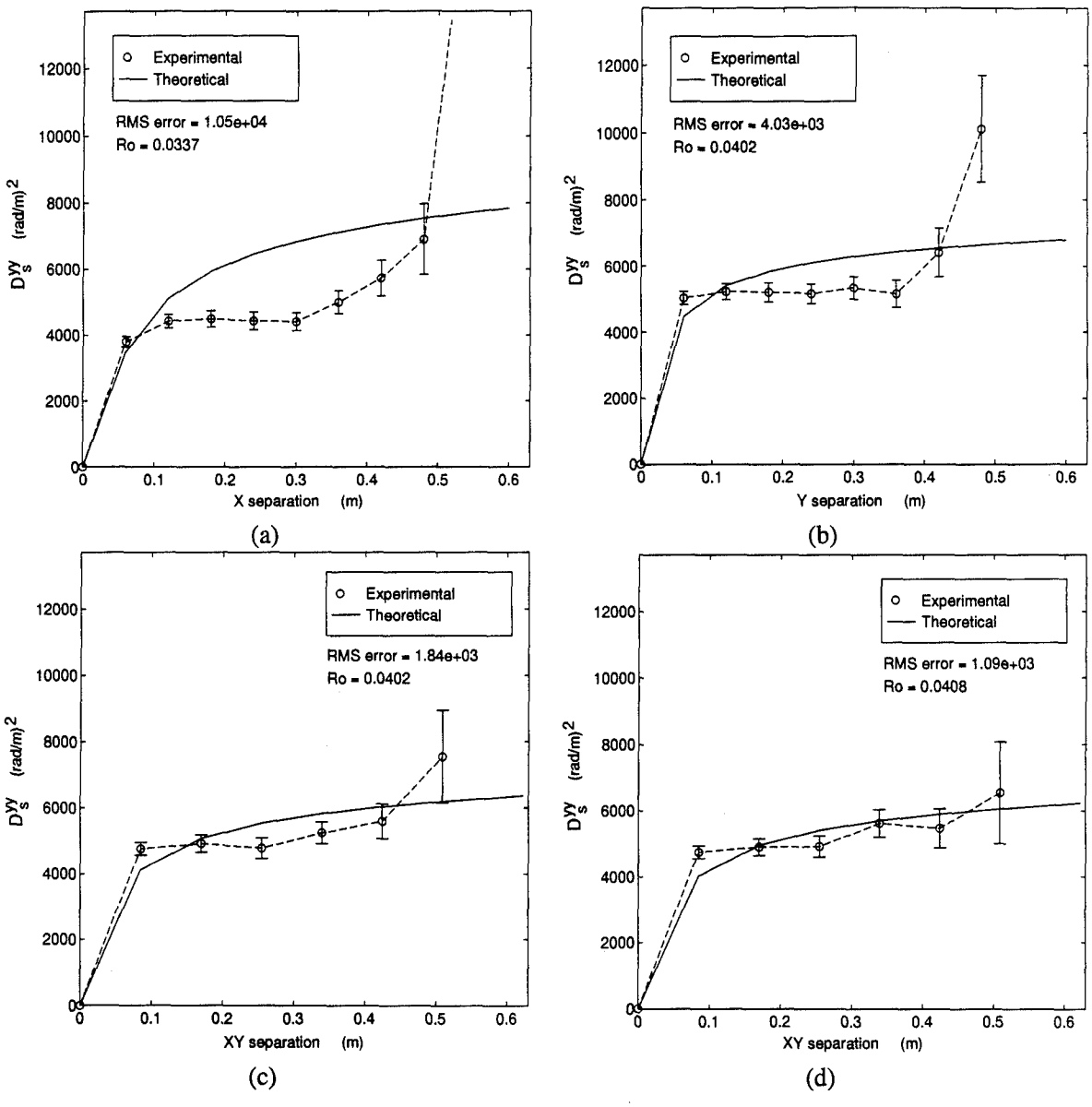

Figure A.24 Structure functionn isotropy: spatially averaged D_s^{yy} for (a) x, (b) y, (c) $+45°$, and (d) $-45°$ separations. Average slopes removed.

Appendix B. Computer code user guide

This appendix is intended to be a short high level overview of the computer code developed for analyzing the H-WFS slope measurements. A brief description of each program or module is provided. As always, the actual code takes precedence over any comment or description.

B.1 IDL code

The H-WFS images are processed in the Interactive Data Language (IDL) environment. The main programs used are described, along with the inputs and outputs.

B.1.1 ACEMAKE.PRO. Compiles the various IDL programs required to process the H-WFS images. Executed by typing `@acemake` at the IDL command prompt.

B.1.2 SLOPES.PRO. The main command interpreter for processing the H-WFS images. Executed by typing `slopes, s=source, d=destination, th=threshold`. The parameter `source` is a string containing the full path to the directory containing the H-WFS images. This directory must contain only ABLE ACE image files or the program will abort. The parameter `destination` is a string containing the full path to the directory where the H-WFS slopes will be stored. The parameter `threshold` is a number setting the threshold at which to display the H-WFS images.

Comments in the `slopes.pro` file contain descriptions of the various commands and their actions for processing the H-WFS images. One file is created for each H-WFS image; its file name will the be same as the image file. Each H-WFS slope file contains four 21x21 matrices in unformatted FORTRAN-77 format. The x slope, y slope, peak intensity, and mask matrices are saved in that order. The x slope, y slope, and intensity matrices are real and the mask matrix is integer.

B.2 MATLAB code

All statistical and structure function calculations were done using the MATLAB environment. Essentially, the MATLAB code is a family of functions and scripts which are called from the MATLAB command line with the proper parameters. A brief description of the inputs, outputs, and action of each function are provided. Detailed comments giving the exact input and output parameters and any restrictions are found in comments in the MATLAB M-files. These comments can be viewed by typing

`help function` at the MATLAB command line, where `function` is the name of the function in question.

B.2.1 DS_GEN.M. Computes the normalized theoretical D_s^{xx} structure function for x, y and $\pm 45°$ separations. The structure functions are returned in vectors. Uses the `dsxx.m` function.

B.2.2 DSXX.M. Computes the a value of the theoretical D_s^{xx} structure function. The input parameters are the x and y subaperture separations, r_o, and the subaperture size. Returns a single value. Uses the `ds_arg.m` function.

B.2.3 DS_ARG.M. Evaluates the normalized integrals for the D_s^{xx} structure function.

B.2.4 ACEFILES.M. Reads the H-WFS slope filenames from a directory. The full pathname must be provided. Only H-WFS slope files must be in the given directory or the function will abort. The file names are returned in the rows of a matrix.

B.2.5 ACEREAD.M. Reads an H-WFS slope file and returns the x slope, y slope, amplitude, and mask matrices. The full path must be specified.

B.2.6 ACEVIEW.M. Displays a matrix using the 'hot' colormap. Useful for debugging.

B.2.7 DSX.M. Computes structure functions for the x separations. Inputs are a mask matrix and two slope matrices. Outputs a structure function and mask matrix.

B.2.8 DSY.M. Computes structure functions for the y separations. Inputs are a mask matrix and two slope matrices. Outputs a structure function and mask matrix.

B.2.9 DSN45.M. Computes structure functions for the $-45°$ separations. Inputs are a mask matrix and two slope matrices. Outputs a structure function and mask matrix.

B.2.10 DSP45.M. Computes structure functions for the $+45°$ separations. Inputs are a mask matrix and two slope matrices. Outputs a structure function and mask matrix.

B.2.11 DSTRUCT.M. A script which computes the structure functions for all slope and separation combinations. Accumulates running sums of the structure function, squared structure function, and mask matrices. These sums are used to compute the structure function, structure function variance, and sum matrices. The results are saved in `.mat` files. Inputs are a string containing the path to the directory containing the H-WFS slope files.

B.2.12 DSTAR.M. Removes the average slopes and computes the structure functions for all slope and separation combinations. Accumulates running sums of the structure function, squared structure function, and mask matrices. These sums are used to compute the structure function, structure function variance, and sum matrices. The results are saved in `.mat` files. Inputs are a string containing the path to the directory containing the H-WFS slope files.

B.2.13 WFS_STAT.M. Computes the slope average, variance, and sum at each point in the aperture. Writes the results to `.mat files`. Inputs are a string containing the path to the directory containing the H-WFS slope files.

B.2.14 DVIEW.M. Displays the submatrices of a structure function matrix in increasing subaperture separation. Inputs are a structure function matrix. Useful for debugging.

B.2.15 DPICK.M. Picks the structure function values corresponding to a particular anchor point and returns those values in a column. Inputs are are a set of vectors listing the x-y coordinates of the structure function and a structure function matrix.

B.2.16 SPCAVG.M. Spatially averages the structure function and computes confidence intervals. Inputs are a set of vectors listing the x-y locations to be averaged; and the structure function, variance, and sum matrices. Outputs are two vectors; one containing the spatially averaged structure function, the other containing the corresponding confidence intervals.

B.2.17 MSFIT.M. Computes the mean-square fit scale parameter and the RMS error. The scale parameter scales the normalized structure function to provide the best mean-square fit between the estimated structure function and theory. The RMS error is the root-mean-square error between

the estimated and the scaled theoretical structure functions. Inputs are the estimated and theoretical structure functions, in vectors. Outputs are the scale factor and the RMS error.

Bibliography

1. Brookner, E. "Atmosphere propagation and communication channel model for laser wavelengths," *IEEE Transaction on Communications Technology, COM-18*(4):396–416 (August 1970).
2. Butts, R. R. "Personnal communication." USAF Phillips Laboratory, Kirtland AFB, NM, July 1995.
3. Butts, R. R. and L. D. Weaver. "ABLEX high-altitude laser propagation experiment." *Laser Beam Propagation and Control*, Proc. SPIE 2120, edited by H Weichel and L. F. DeSandre. 30–42. 1994.
4. Cloutier, M. A. *Using Error Detection and Correction Coding for a Turbulent Atmospheric Optical Comminacations Link.* MS thesis, AFIT/GEO/ENG/90D-3, Graduate School of Engineering, Air Force Institute of Technology (AETC), Wright-Patterson AFB OH, 1990.
5. Feldmann, R. J. *Airborne Laser Communications Scintillation Measurements.* MS thesis, AFIT/GEO/ENG/87J-2, Graduate School of Engineering, Air Force Institute of Technology (AETC), Wright-Patterson AFB OH, 1987.
6. Fried, D. L. "Aperture averaging of scintillation," *Journal of the Optical Society of America*, 169–174 (February 1967).
7. Fried, D. L. "Optical heterodyne detection of an atmospherically distorted signal wavefront," *IEEE Proceedings*, 57–67 (January 1967).
8. Goodman, J. W. *Introduction to Fourier Optics.* New York: McGraw-Hill, 1968.
9. Heidbreder, G. R. "Image degredation with random wavefront tilt compensation," *IEEE Trans. on Antennas and Propagation*, 90–98 (January 1967).
10. Hoversten, E. V., et al. "Communication theory for the turbulent atmosphere," *IEEE Proceedings*, *58*(10):180–204 (1970).
11. Kolmogorov, A. *Turbulence, Classical Papers on Statistical Theory* edited by S.K. Friedlander and L. Topper, New York: Wiley-Interscience, 1961.
12. Magee, E. P. and B. M. Welsh. "Characterization of laboratory generated turbulence by optical phase measurements," *Optical Engineering*, 3810–3817 (November 1994).
13. Markson, R. M., et al. *Atmospheric Turbulence Measurements in Support of Adaptive Optics Technology.* Technical Report RADC-TR-89-289, Rome Air Development Center, 1989.
14. Noll, R. J. "Zernike polynomials and atmospheric turbulence," *JOSA*, *66*:207–211 (1976).
15. Papoulis, A. *Probability, Random Variables, and Stochastic Processes* (3rd Edition). New York: McGraw-Hill, Inc., 1991.
16. Roggemann, M. C. "Optical performance of fully and partially compensated adaptive optics systems using least-squares and minimum variance phase reconstructors," *Computers and Electrical Engineering*, 451–466 (June 1992).
17. Roggemann, M. C. and D. W. Tyler. "Unconventional astronomical imaging," *Optics and Photonics News*, 17–21 (March 1992).

18. Seeger, R. N. *Characterization of an Air-to-Air Optical Heterodyne Communication System.* MS thesis, AFIT/GE/ENG/90D-55, Graduate School of Engineering, Air Force Institute of Technology (AETC), Wright-Patterson AFB OH, 1990.

19. Spreen, D. E. and C. B. Hogge. "Characterizing high-altitude horizontal path optical propagation." *Laser Beam Propagation and Control*, Proc SPIE 2120, edited by H Weichel and L. F. DeSandre. 2–9. 1994.

20. Strang, G. *Linear Algebra and its Applications* (3rd Edition). Fort Worth, TX: Harcourt Brace Jovanovich, Inc., 1988.

21. Stribling, B. E. *Laser Beam Propagation in Non-Kolmogorov Atmospheric Turbulence.* MS thesis, AFIT/GEO/ENG/94D-04, Graduate School of Engineering, Air Force Institute of Technology (AETC), Wright-Patterson AFB OH, 1994.

22. Tatarski, V. I. *Wave Propagation in a Turbulent Medium.* New York: McGraw-Hill Book Company, 1961.

23. von Karman, T. "Progress in the statistical theory of turbulence." *Turbulence, Classic Papers on Statistical Theory* edited by S.K. Friedlander and L. Topper, 162–174, New York: Wiley-Interscience, 1961.

24. Wallner, Edward P. "Optimal wave front correction using slope measurements," *Journal of the Optical Society of America*, 1771–1776 (December 1983).

25. Washburn, D. *ABLE ACE: ABL Extended Atmospheric Characterization Experiment.* Technical Report, Kirtland AFB, NM 87117-5776: USAF Phillips Laboratory, 1994.

Vita

Eric Eugene Silbaugh [redacted]e graduated from the Alliance Christian Academy, Elk River, MN high school in June 1985. Eric graduated from the University of Minnesota, Minneapolis, MN in December 1989 with a Bachelors of Electrical Engineering. Eric was commissioned a Second Lieutenant in the USAF through the ROTC program upon graduation. Second Lieutenant Silbaugh entered active duty in October, 1990.

After attending Basic Communications Officer Course at Kessler AFB, MS Lieutenant Silbaugh was assigned to the 485th Engineering Installation Group, Griffiss AFB, NY. While at the 485th EIG Lieutenant Silbaugh worked as a wideband systems engineer and also as the Systems Telecommunications Engineering Manager for Columbus AFB, MS. Captain Silbaugh was then selected to attend the Air Force Institute of Technology (AFIT) in May, 1994.

Captain Silbaugh graduated from AFIT in December, 1995 with a Masters of Science in Electrical Engineering degree, specializing in communications and radar systems and optical information processing. Captain Silbaugh has been assigned to the Air Force C4 Agency at Scott AFB, IL.

[redacted]

REPORT DOCUMENTATION PAGE

Form Approved
OMB No. 0704-0188

1. AGENCY USE ONLY (Leave blank)	2. REPORT DATE	3. REPORT TYPE AND DATES COVERED
	December 1995	Master's Thesis

4. TITLE AND SUBTITLE
CHARACTERIZATION OF ATMOSPHERIC TURBULENCE OVER LONG HORIZONTAL PATHS USING OPTICAL SLOPE MEASUREMENTS

5. FUNDING NUMBERS

6. AUTHOR(S)
Eric Eugene Silbaugh, Capt, USAF

7. PERFORMING ORGANIZATION NAME(S) AND ADDRESS(ES)
Air Force Institute of Technology, WPAFB OH 45433-7765

8. PERFORMING ORGANIZATION REPORT NUMBER
AFIT/GE/ENG/95D-25

9. SPONSORING / MONITORING AGENCY NAME(S) AND ADDRESS(ES)
Dr. Russell Butts
PL/LIAE
3550 Aberdeen SW
Kirtland AFB, NM 87117-5776

10. SPONSORING / MONITORING AGENCY REPORT NUMBER

11. SUPPLEMENTARY NOTES

12a. DISTRIBUTION / AVAILABILITY STATEMENT
Approved for Public Release; Distribution Unlimited

12b. DISTRIBUTION CODE

13. ABSTRACT *(Maximum 200 words)*

Atmospheric turbulence has long been recognized as one of the fundamental factors affecting optical systems operating through the atmosphere. Turbulence over vertical paths has been well characterized, both theoretically and experimentally. Much less is known about turbulence over long, horizontal paths. Perturbations of the wave front phase can be measured using a Hartmann wave front sensor (H-WFS). Theoretical expressions for the tilt-removed structure function of the H-WFS slope measurements were derived and evaluated using quadrature. These slope structure functions are functions of the phase structure function. The Kolmogorov turbulence model was assumed. Simulated H-WFS slope measurements were generated using an adaptive optics simulation code. The effects of deterministic aberrations on the structure function estimator were illustrated using the simulated slope measurements. Average slope removal was shown to be effective in removing the effects of aberrations. Five H-WFS measurement data sets from the ABLE ACE database were analyzed for homogeneity, isotropy, and fit to theory. The ABLE ACE experiment recorded H-WFS measurements over horizontal paths 20-200 km in length. Results indicate that the turbulence encountered appears to be homogeneous and isotropic and seems to fit the Kolmogorov turbulence model.

14. SUBJECT TERMS
atmospheric turbulence, wave front sensing, Hartmann-type wave front sensor, structure function, optical communication

15. NUMBER OF PAGES
110

16. PRICE CODE

17. SECURITY CLASSIFICATION OF REPORT	18. SECURITY CLASSIFICATION OF THIS PAGE	19. SECURITY CLASSIFICATION OF ABSTRACT	20. LIMITATION OF ABSTRACT
UNCLASSIFIED	UNCLASSIFIED	UNCLASSIFIED	UL